# ENERGY EFFICIENT NAVIGATIONAL METHODS FOR AUTONOMOUS UNDERWATER GLIDERS IN SURFACE DENIED REGIONS

by

© Brian Claus
Master of Engineering, Bachelor of Engineering

A thesis submitted to the
School of Graduate Studies
in partial fulfillment of the
requirements for the degree of
Doctor of Philosophy.

Faculty of Engineering and Applied Science
Memorial University of Newfoundland

April 2, 2015

St. John's Newfoundland

# Abstract

Autonomous underwater gliders routinely perform long duration profiling missions while characterizing the chemical, physical and biological properties of the water column. These measurements have opened up new ways of observing the ocean's processes and their interactions with the atmosphere across time and length scales which were not previously possible. Extending these observations to ice-covered regions is of importance due to their role in ocean circulation patterns, increased economic interest in these areas and a general sparsity of observations.

This thesis develops an energy optimal depth controller, a terrain aided navigation method and a magnetic measurement method for an autonomous underwater glider. A review of existing methods suitable for navigation in underwater environments as well as the state of the art in magnetic measurement and calibration techniques is also presented.

The energy optimal depth controller is developed and implemented based on an integral state feedback controller. A second order linear time invariant system is identified from field data and used to compute the state feedback controller gains through an augmented linear quadratic regulator. The resulting gains and state feedback controller methodology are verified through field trials and found to control the depth of the vehicle while losing less than one percent of the vehicle's propulsive load to control inputs or lift induced drag.

The terrain aided navigation method is developed based on a jittered bootstrap algorithm which is a type of particle filter that makes use of the vehicle's dead-reckoned navigation solution, onboard altimeter and a local digital parameter model (DPM). An evaluation is performed through post-processing offline location estimates from field trials which took place in Holyrood Arm, Newfoundland, overlapping a previously collected DPM. During the post-processing of these trials, the number of particles, jittering variance and DPM grid cell size were varied. Online open loop field trials were performed through integrating a new single board computer. In these trials the localization error remained bounded and improved on the dead reckoning error, validating the filter despite the large dead-reckoned errors, single beam altitude measurements, and short test duration.

Terrain aided navigation methods perform poorly in regions of flat terrain or in deep water where the seafloor is beyond the range of the altimeter. Magnetic measurements of the Earth's main field have been proposed previously to augment terrain aided navigation algorithms in these regions. To this end a low power magnetic instrumentation suite for an underwater glider has been developed. Two calibration methodologies were also developed and compared against regional digital models of the magnetic field. The calibration methods include one for which the actuators in the vehicle were kept in fixed locations and a second for which the calibration coefficients were parameterized for the actuator locations. Both methods were found to agree with the low frequency content in the a-priori regional magnetic anomaly grids.

# Acknowledgements

The production of this thesis benefited from the support of many superb individuals. First, I would like to thank my supervisor, Dr. Ralf Bachmayer, who convinced me to stay on for another graduate degree and allowed me such flexibility in my research program. Also, the members of my supervisory committee, Dr. Brad deYoung and Dr. Colin Farquharson, for their guidance and feedback.

A special thanks goes to Craig Legge at the Holyrood Marine base for all his assistance during the field trials that occurred there; to Allison Eaton and Robert Scott at the Bonne Bay Marine Station for their willingness to deploy instruments in December in Newfoundland; to the members of the Ocean Tracking Network for making their lab available at the Bedford Institute of Oceanography to prepare the gliders prior to boarding the CCGS Hudson; and to the crew of the CCGS Hudson for their assistance and professionalism in the deployment of the gliders in the Labrador Sea.

This project was supported through funding provided by the Natural Sciences and Engineering Research Council (NSERC) through the NSERC Canadian Field Robotics Network (NCFRN) and the Alexander Graham Bell Canada Graduate Scholarships Doctoral Program, the Research Development Corporation Ocean Industries Student Research Award, the Marine Institute through use of their Holyrood Marine Base and digital parameter models and Memorial University of Newfoundland.

Portions of this work have appeared in Oceans 2014 in St. John's [1], AUV 2012 in Southampton [2] and UUST 2011 in Portsmouth, NH [3]. The glider terrain aided navigation method has been accepted to the Journal of Field Robotics [4].

Finally, I would like to thank my wife and two amazing children, whose patience and encouragement enabled the completion of this work.

# Contents

# List of Figures

# List of Tables

# Nomenclature

| | |
|---|---|
| $ADC$ | Analog to digital converter |
| $AUV$ | Autonomous Underwater Vehicle |
| $AZMP$ | Atlantic Zone Monitoring Program |
| $BBB$ | Beagle Bone Black |
| $CTD$ | Conductivity, temperature and pressure sensor |
| $DPM$ | Digital Parameter Model |
| $DVL$ | Doppler Velocity Log |
| $ETOPO1$ | 1 arc minute global relief model |
| $GEBCO08$ | General Bathymetric Chart of the Oceans 2008 |
| $GMRT$ | Global Multi-Resolution Topography |
| $GPS$ | Global Positioning System |
| $ICNAF$ | International Commission for the Northwest Atlantic Fisheries |
| $IGRF$ | International Geomagnetic Reference Field |
| $INS$ | Inertial Navigation System |

| | |
|---|---|
| $LBL$ | Long Base Line |
| $LQR$ | Linear Quadratic Regulator |
| $LRA$ | Long Range Autosub |
| $MBARI$ | Monterey Bay Aquarium Research Institute |
| $MCLB$ | Monte Carlo Lower Bound |
| $MCUB$ | Monte Carlo Upper Bound |
| $MEMS$ | Micro-ElectroMechanical Systems |
| $MFAM$ | Micro-Fabricated Atomic Magnetometer |
| $OWTT$ | One Way Travel Time |
| $RMS$ | Root Mean Square |
| $SBL$ | Short Base Line |
| $SLAM$ | Simultaneous Localization And Mapping |
| $SQUID$ | Superconducting Quantum Interference Devices |
| $SRTM30$ | Shuttle Radar Topography Mission 30 |
| $TAN$ | Terrain Aided Navigation |
| $USBL$ | Ultra Short Base Line |
| $\Delta\mathbf{T}$ | Time between measurements |
| $\Delta\mathbf{x}$ | Position updates |

| | |
|---|---|
| $\Delta\mathbf{x}_{rt,k}$ | Ray traced measurement location offsets at time step k |
| $\Delta z$ | Ray tracing depth increment |
| $\alpha$ | Angle of attack |
| $\delta$ | Magnetic declination |
| $\eta$ | Propulsive efficiency |
| $\phi_{g,k}$ | Glider roll at time step k |
| $\psi$ | Vehicle magnetic heading |
| $\psi_{b,k}$ | Altimeter beam heading at time step k |
| $\psi_{g,k}$ | Glider heading at time step k |
| $\rho$ | Fluid density |
| $\sigma_j^2$ | Jitter variance |
| $\sigma_{DPM}^2$ | Digital parameter model variance |
| $\theta$ | Pitch angle |
| $\theta_v$ | Altimeter beam angle from vertical |
| $\theta_{g,k}$ | Glider pitch at time step k |
| $\xi$ | Glide path angle |
| $A$ | Cross sectional area |
| $\bar{\mathbf{A}}$ | Augmented system matrix |

| | |
|---|---|
| $\mathbf{A}$ | System matrix |
| $\bar{\mathbf{B}}$ | Augmented input matrix |
| $\mathbf{B}$ | Input matrix |
| $\mathbf{C}$ | Output matrix |
| $C_D$ | Coefficient of drag |
| $C_L$ | Coefficient of lift |
| $\mathbf{D}$ | Feed forward matrix |
| $\mathbf{E}$ | Energy |
| $F_B$ | Buoyant force |
| $F_D$ | Drag force |
| $F_g$ | Gravitational force |
| $F_L$ | Lift force |
| $\mathbf{H}_{IGRF}$ | International Geomagnetic Reference Field |
| $H_a$ | Magnetic anomaly |
| $\mathbf{H}_c$ | Calibrated magnetic data |
| $H_e$ | Local field |
| $\mathbf{H}_r$ | Raw magnetic data |
| $\boldsymbol{\mathcal{J}}$ | Quadratic cost function |

| | |
|---|---|
| $\bar{\mathbf{K}}$ | Optimal feedback gain matrix |
| $\mathbf{K}$ | Gain matrix |
| $\mathbf{K}_I$ | Integral gain matrix |
| $\hat{Lat}$ | Latitude estimate |
| $\hat{Lon}$ | Longitude estimate |
| $\mathbf{M}$ | Rotation matrix |
| $N$ | Number of particles |
| $P_0$ | Zero angle of attack power |
| $P_1$ | Constant velocity propulsive power |
| $\bar{\boldsymbol{\mathcal{P}}}$ | Linear Algebraic Riccati matrix |
| $P_p$ | Propulsive power |
| $P_h$ | Base power required by the sensors and vehicle systems |
| $\mathbf{P}_u$ | Input power matrix |
| $\boldsymbol{\mathcal{Q}}$ | Error weighted matrix |
| $R$ | Range of an underwater glider |
| $\boldsymbol{\mathcal{R}}$ | Control weighted matrix |
| $\mathbf{S}$ | Scaling Matrix |
| $SV(z)$ | Sound velocity as a function of depth |

| | |
|---|---|
| $\mathbf{T}$ | Translation Matrix |
| $V$ | Vehicle velocity |
| $V_0$ | Zero angle of attack velocity |
| $V_1$ | Constant propulsive power velocity |
| $a$ | Ray tracing constant |
| $c$ | Speed of sound in water |
| $cs$ | Cumulative sum |
| $\mathbf{h}$ | Resampled particles |
| $i$ | Particle index |
| $k$ | Time step |
| $n$ | Random number on the interval [0,1] |
| $p_b$ | Ballast location |
| $p_m$ | Moving mass location |
| $\mathbf{r}$ | Particle jitter |
| $\mathbf{s}$ | Control input |
| $r_e$ | Radius of the earth |
| $s_w$ | Sum of the particle weights |
| $\bar{\mathbf{u}}$ | Augmented input vector |

| | |
|---|---|
| $\bar{\mathbf{u}}^*$ | Minimum energy control law |
| $\delta\mathbf{u}$ | Input error |
| $\mathbf{u}$ | Input vector |
| $\delta\mathbf{v}$ | State integral error |
| $\mathbf{v}$ | State integral vector |
| $v_A$ | Glide path velocity |
| $v_z$ | Vertical velocity |
| $w$ | Normalized particle weights |
| $\tilde{w}$ | Raw particle weights |
| $\bar{\mathbf{x}}$ | Augmented state matrix |
| $\delta\mathbf{x}$ | State error |
| $\hat{\mathbf{x}}$ | State estimate |
| $x_{ap}$ | Along axis pressure sensor, altimeter separation |
| $\mathbf{x}_k$ | Vehicle location in the local coordinate frame at time step $k$ |
| $\mathbf{y}$ | Output vector |
| $\mathbf{z}$ | Water depth estimate |
| $z_{T,k}$ | Tidal correction at time step k |
| $z_{w,k}$ | Water depth estimate at time step k |

| | |
|---|---|
| $z_{a,k}$ | Measured altitude at time step k |
| $z_b$ | Digital parameter model depth bias |
| $z_{DPM}$ | Digital parameter model water depth |
| $z_{g,k}$ | Glider depth at time step k |
| $\hat{z}_{rt,k}$ | Ray traced water depth at time step k |

# Chapter 1

# Introduction

Over the past decade underwater gliders, a type of autonomous underwater vehicle (AUV), have proven their ability to persistently monitor ocean processes in a wide range of conditions [11]. However, operational gaps still exist in regions where surface access is limited due to ice cover or heavy ship traffic.

## 1.1 Motivation

Sustained underwater observations in regions with ice cover are of particular importance to climate change research and polar exploration efforts, making tools to overcome these observational obstacles a key development in improving global climate change predictions [12]. The sparsity of historical observations in ice covered regions makes it difficult to determine the anthropogenic impact on these environments. Further, recent under ice observational programs have shown that satellite based estimates of the biology and biogeochemistry surrounding sea ice and under shelf ice are in error by an order of magnitude [13, 14].

Changing sea ice concentrations bring new economic opportunities as well. Oil and gas exploration efforts are increasing due to an estimated 13 and 30 percent of the world's undiscovered oil and gas reserves respectively being in Arctic waters [15]. Shipping traffic through Arctic sea lanes is also projected to increase with new routes projected to open for open water and polar class vessels during the summer months by the mid 21st century [16, 17].

This combination of increased economic activity and poorly understood environmental conditions requires the establishment of an observational record through persistent in-situ observations. This record allows the equitable allocation of resource rights through identifying environmentally sensitive areas. It also establishes the predevelopment conditions to determine the degree of reparation necessary in case of an accident. Autonomous underwater gliders and other long range autonomous underwater vehicles are potential platforms to gather these measurements. However, these platforms rely on GPS information gathered at the surface to update their navigation solutions. In ice covered regions the ability to surface is not possible requiring new navigational tools to enable persistent observations by these platforms.

As the vertical locations of the observations are sufficiently provided by the scientific pressure sensor, the task of estimating the vehicle's depth is separated from the horizontal localization estimates. While operating in profiling modes the vertical control of the vehicle is well suited to performing steady state glides. Conversely, maneuvering the vehicle in horizontal flight modes through use of the hybrid propulsion system can result in significant energy being lost to lift induced drag. This parasitic drag is the result of the non zero angle of attack needed to generate a lift force capable of compensating for the net buoyant force of the vehicle. For long duration maneuvers utilizing horizontal flight modes a control methodology which minimizes this wasted energy is needed.

To achieve long range navigation with an underwater glider without surface access the navigation sensors must represent an average power of less than a few Watts and have a bounded position error which meets the needs of the mission. For typical profiling glider missions which provide feedback into oceanographic models, the horizontal localization requirements are often on the order of 10s of meters. Ideally, the navigation system should be scalable with respect to accuracy and power in order to be able to choose between more accurate position locations at the expense of a higher energy consumption. Inertial navigation systems and dead reckoning algorithms are subject to drift which over month or year long deployments can develop errors exceeding kilometers. A method producing a bounded location estimate is therefore needed. To obtain bounded position estimates it is necessary to use location techniques which rely on predictable measurable features such as an acoustic transponder or a model of the terrain. To be suited to mission durations on the order of months these measurements must consume little energy and the position calculation simple enough to be computed by the existing onboard processors or an additional low power processor.

For the purpose of discussion, the Labrador Shelf is taken as the design environment and straight line sections out across the shelf and back as the design mission to align with prior sampling strategies of the Atlantic Zone Monitoring Program (AZMP), the International Commission for the Northwest Atlantic Fisheries (ICNAF) and the Fisheries Research Board of Canada [18, 19]. These programs and research bodies established standard oceanographic sections to be performed several times per year as conditions and ships were available as shown in Fig. 1.1.

The northernmost section in the AZMP is the Seal Island section. This section was determined to be the northern boundary of where it was possible to collect observations over several seasons while still constraining the southward flow of Arctic water before it splits into the Gulf of St. Lawrence and the Newfoundland Shelf. Other sections have been established and occupied when possible, usually in mid-

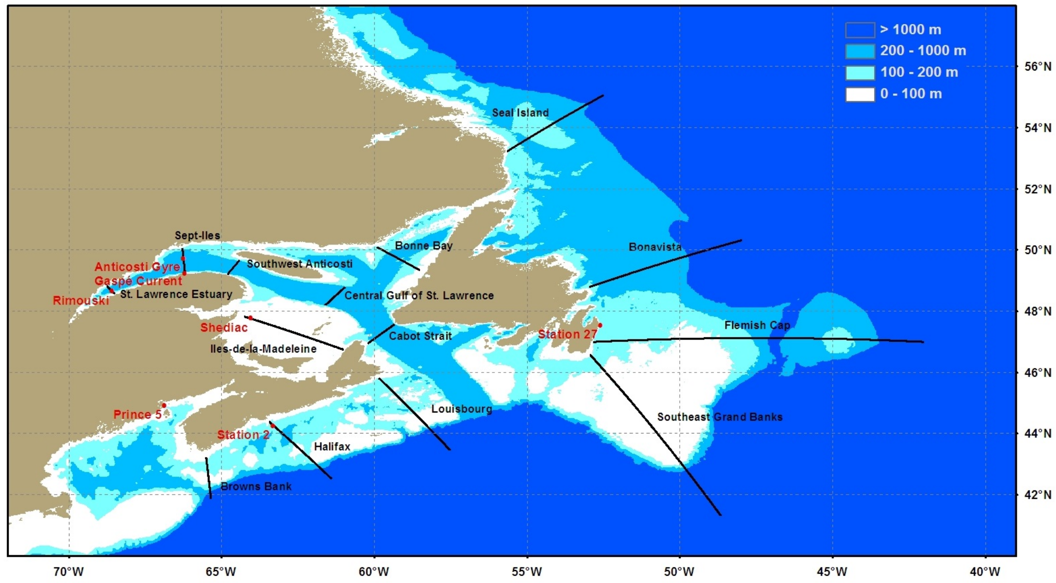

Figure 1.1: Sections in the Atlantic Zone Monitoring Program [5]

summer [19].

The Labrador Shelf is composed of several distinct regions consisting of an inner shelf characterized by the initial 200 meter isobath, a marginal trough with local depths reaching 800 meters and an outer shelf composed of shallower banks broken up by deeper saddle regions as shown in Fig. 1.2 [6]. The main shelf break is typically found at the 600 meter isobath. The Labrador current flows southward, roughly following the shelf break with a typical surface speed of 0.3 m/s [20].

The Labrador Shelf experiences seasonal sea ice during the winter months beginning in December and continuing to grow until the seasonal maximum in March, past which the ice retreats with breakup in May through June depending on the latitude as shown in Fig. 1.3 [7]. The inter-annual variability of the sea ice extent can be significant with variations from the median value often exceeding 5 percent with the ice maximum generally in late February or early March as illustrated in Fig. 1.4 [7].

The average number of weeks of sea ice presence over the last 40 years for the

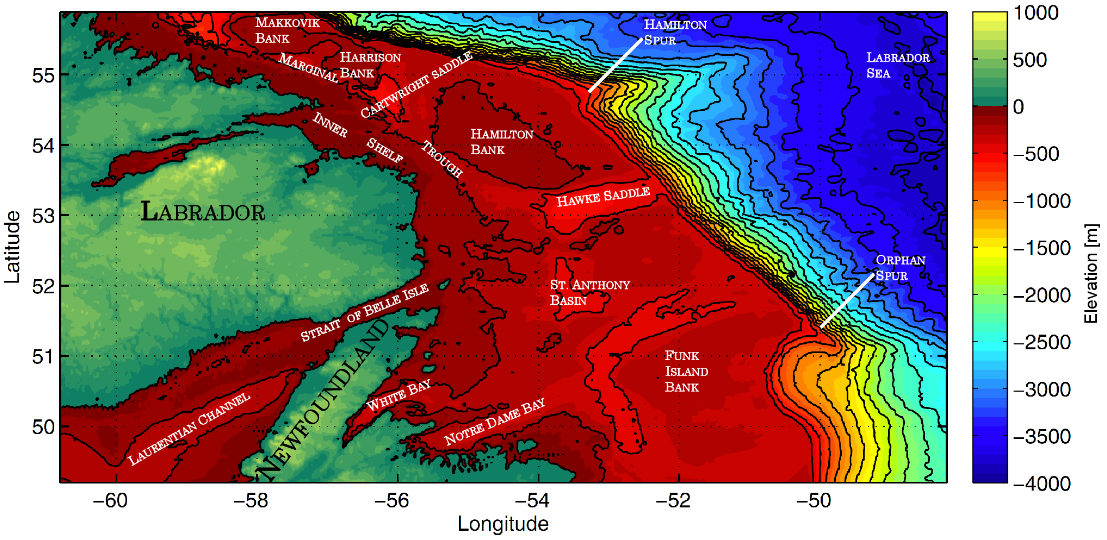

Figure 1.2: Bathymetry of the Labrador Shelf from the Global Multi Resolution Topography model with 200 meter contour lines [6]

inner shelf has been around 20 weeks, for the marginal trough regions about 16 weeks and for the outer shelf about 10 weeks as shown in Fig. 1.5 [8, 9].

Sea ice concentrations decrease from the coastal areas to the shelf break with the outer boundary roughly corresponding to the shelf break. A vehicle operating under ice on the Labrador Shelf could therefore reasonably expect sea ice for up to 6 months over a portion of its traverse of the shelf.

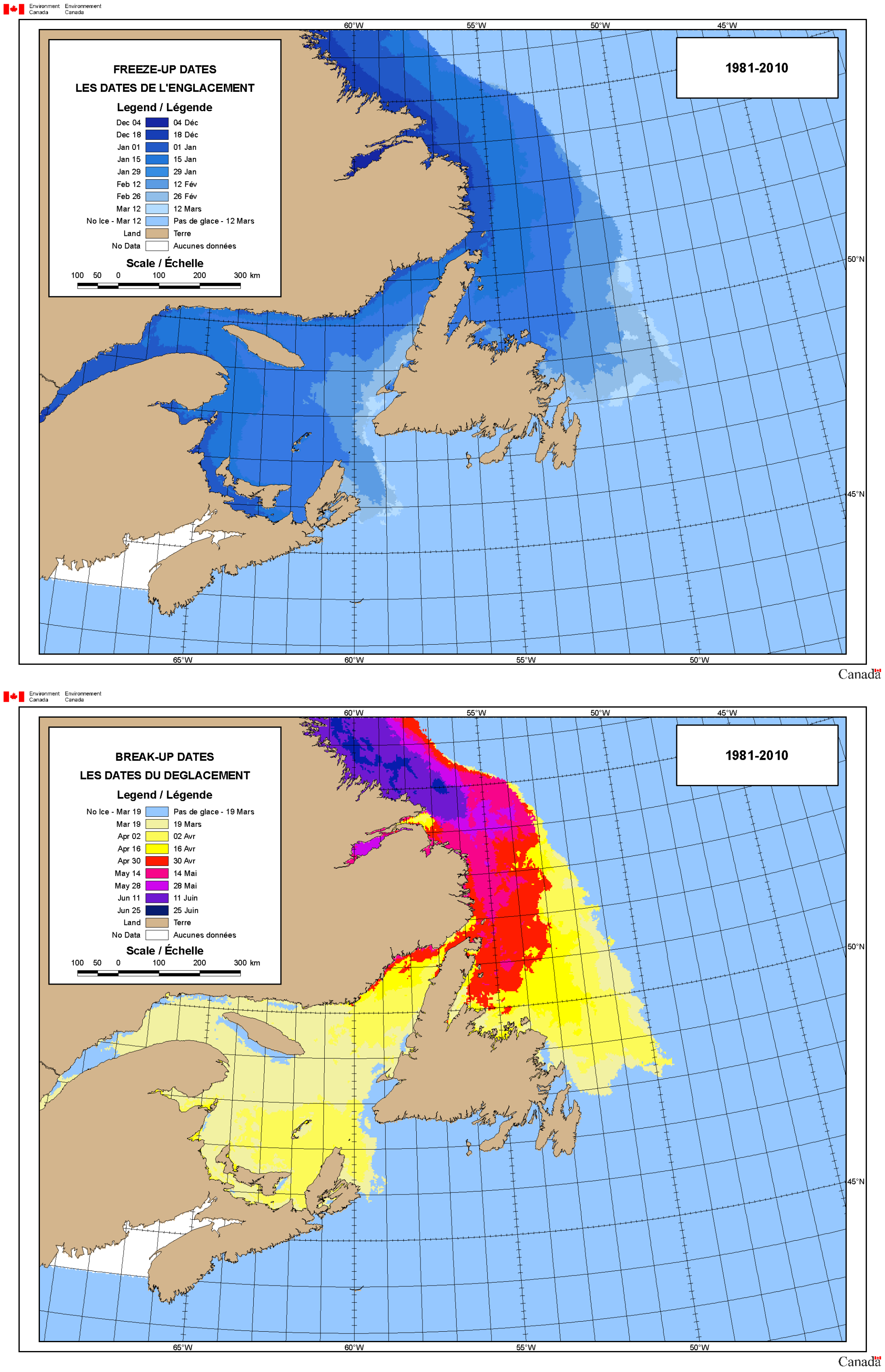

Figure 1.3: Freeze up and break up dates by location for the East Coast of Canada, Source: Canadian Ice Service [7]

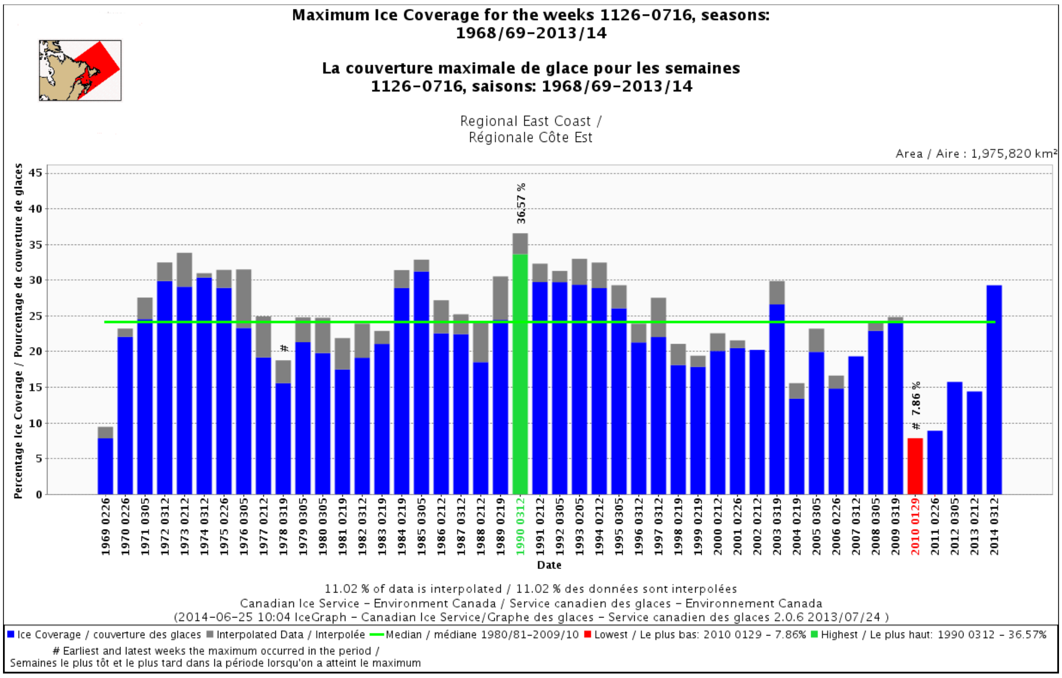

Figure 1.4: Percent coverage and week of the ice maximum between the years 1969 and 2014, Source: Canadian Ice Service [7]

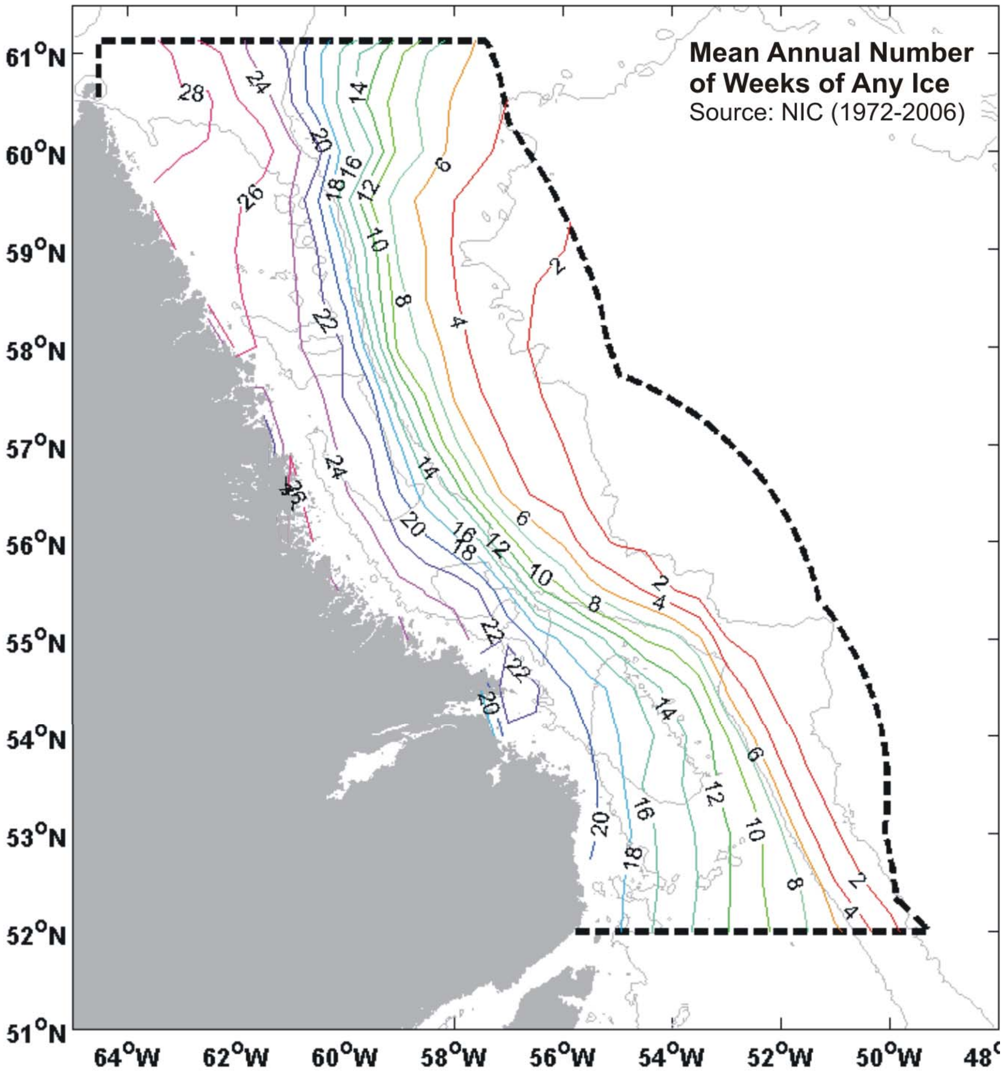

Figure 1.5: Labrador Shelf showing the average number of weeks of ice presence as contour lines [8, 9]

## 1.2 Available Navigational Methods

Existing methods for underwater navigation may be grouped into geophysical, acoustic, inertial, multi-vehicle and model based techniques [21, 22, 23]. Of the available methods, only acoustic systems and geophysical methods provide bounded location estimates.

### 1.2.1 Acoustic

Acoustic localization methods in general rely on range and bearing information between a sound source and a receiver to compute a location estimate. For the distances required to traverse from the near shore to open water under the sea ice during the winter maximum, acoustic methods would require either a very low frequency sound source, a net of multiple sound sources or a surface vessel shadowing the AUV. In regions with periodic ice cover, a shadowing vehicle is often not practical and in shipping lanes can present a navigational hazard. Infrastructure costs for acoustic nets of standard long baseline (LBL) systems are prohibitively expensive once the vehicle's range extends past the nominal range of tens of kilometers. Low frequency sound sources are perhaps the only alternative left for acoustic localization of long range vehicles with ranges on the order of hundreds of kilometers [24, 25, 26, 27]. However, these systems are expensive to maintain and deploy making them more suited to limited duration observational programs.

### 1.2.2 Geophysical

Geophysical aided methods have no infrastructure requirements, making them attractive for long distance surface denied transects from a cost perspective. These methods make use of measurements of the bathymetric, magnetic or gravimetric features, which, when compared with a digital parameter model, provide some localizing information. Successful field trials of terrain aided methods have been performed with multibeam sonar or acoustic doppler current profilers which give a measure of the bathymetry when combined with the vehicle depth given by the pressure sensor [28, 29, 30].

The majority of these demonstrations use an existing fused navigation solution from a high accuracy inertial navigation system (INS) aided by a Doppler velocity log (DVL) as an input to the terrain aided navigation (TAN) algorithm [31]. This high accuracy navigation update is then combined with the measurement update from a multi-beam sonar or DVL which give a measure of the bathymetry when combined with the vehicle depth given by the pressure sensor [32, 33]. However, it has recently been shown that lower grade inertial sensors aided by a DVL may be used by directly including the inertial and DVL measurements in the filter used for the terrain aided navigation [34]. This tight coupling has the effect of increasing the number of states in the terrain algorithm but also increases the reliability and accuracy.

These methods in general have the limitations of requiring a detailed digital parameter model (DPM) of the region and considerable design effort to tailor the algorithms to a specific platform. Further, they require measurements of the geophysical parameters to compare to the DPMs which in the bathymetric case is not always possible if the seafloor is out of range of the SONAR (multi-beam, DVL or single-beam). These methods also suffer degradation in areas where the DPM does not have sufficient variation to provide meaningful corrections.

To overcome the limitations of sensor proximity and terrain uniformity in bathymetric aiding techniques, gravimetric and geomagnetic information have been proposed as augmentations or as a replacement to the bathymetric DPM [35, 36]. The proposed methods rely on the same concepts as the bathymetric techniques with the exception that they may be sensed ubiquitously underwater. Several simulations have been presented to date using pre-recorded data as a map for navigational underwater aiding [37], [38]. To the best of the author's knowledge there has been no practical demonstration of magnetic or gravimetric relative navigational aiding with an AUV or underwater glider.

## 1.3 Suitability of Available Navigation Methods

To achieve long range navigation for an underwater glider without surface access the navigation instrumentation must be low power and must have a bounded position error which meets the needs of the mission. For typical profiling glider missions which provide data for assimilation and evaluation of numerical ocean models and other ocean science applications, the horizontal localization requirements are often on order of 10s of meters. For the proposed mission scenario of a glider traversing an endurance line under the sea ice to out past the maximum sea ice extent, the vehicle must travel around 175 to 250 kilometers each way. For an underwater glider traveling at nominal speeds of around 20 kilometers per day this would take around two weeks. For a glider equipped with enough energy to repeatedly take measurements along the endurance line from freeze up to break up, multiple transects would have to be performed. The longest distance traveled by the vehicle without surface access in this scenario would be from outside the sea ice extent in towards the coast and back out again during the sea ice maximum, or around 350 to 500 kilometers. In addition, the vehicle would need to be deployed prior to freeze-up and be recovered after breakup. This time-frame, between a coastal deployment and recovery, is around 150 to 180 days. A suitable navigational aid must therefore provide bounded error location estimates on the order of 10s of meters over a horizontal distance of 500 kilometers while having an endurance of 5 to 6 months.

The 200 meter Slocum electric glider's base power consumption is around 1 Watt, requiring around 4.5 kWhrs for the vehicle equipped with a standard science payload on a 6 month deployment. This amount of energy requires a lithium primary pack for the Slocum glider which has about 7.2 kWhrs. After derating the pack for a temperature of four degrees and a self discharge of around 3 percent the energy is 6.5 kWhrs [39]. The leftover energy for a navigation solution is around 2 kWhrs which is 0.5 W over 6 months. If more energy is needed an additional battery pack could be added, however, for design purposes the navigational aids must consume less than 0.5 W on average.

### 1.3.1 Acoustic

Given that a low frequency sound source for synchronous, one way travel time navigation and the associated receiver on the glider are available it is a useful exercise to examine a system configuration which meets the needs of the proposed mission. It is assumed that the range of these sources will be around 100 kilometers on and outside the shelf break depending on frequency varying sound propagation conditions. In the shallower water of the inner shelf and bank regions this range would likely decrease to around 50 kilometers. To cover the 200 kilometers to the shelf break it would be necessary to have at least two sources arranged as in Fig. 1.6.

These source locations are positioned such that the majority of the vehicle's transit across the shelf is in deeper water where the sound should propagate well. The source in the marginal trench is located to be within the assumed 50 kilometer range on the inner shelf while still covering most of the shelf. In this manner two sources are available to localize the vehicle which should be considered the bare minimum for an

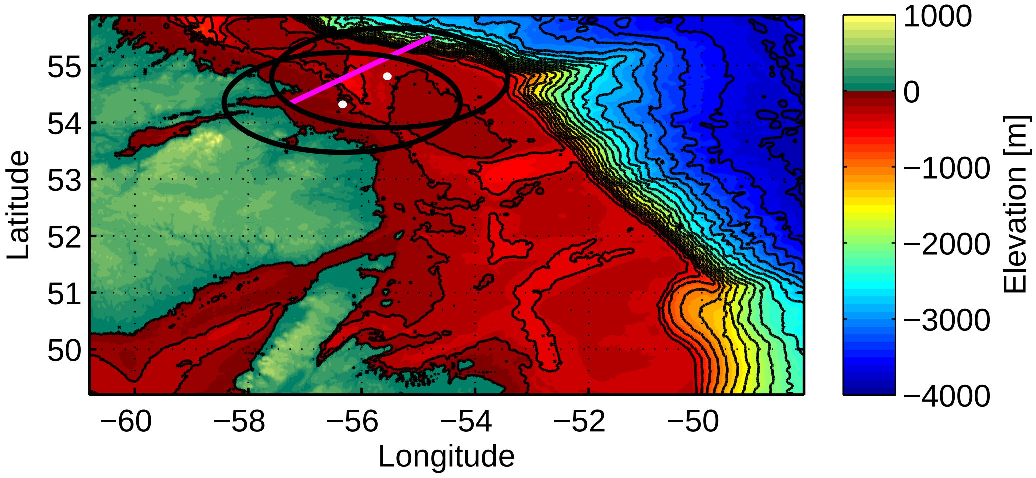

Figure 1.6: Possible location of two low frequency sound sources (white) to ensonify the Cartwright Saddle. The potential range for aiding information is shown as black circles surrounding the sound sources. A proposed track-line utilizing the sound sources is shown in pink. The bathymetry of the Labrador Shelf is shown with 200 meter contour lines [6].

operational system.

By locating the sources on the edge of the marginal trench and the Hamilton Bank the installations would be protected from ice scouring. However, the Labrador Shelf experiences significant bottom trawling activity resulting in possible mooring loss. This activity combined with equipment failure and the harsh ocean environment creates a challenging environment in which to deploy underwater installations.

By setting the transmission schedule to be modest the average power requirements on the receiving side remain low. For example the Woods Hole Oceanographic Institute's micromodem 2 has a detect mode consumption of 0.08 W, 0.3 W while receiving and 2.3 W while decoding the packets [41]. Assuming a transmission schedule of every 5 minutes and that the decoding happens at the same time as the receiving for 5 seconds, the device would consume an average power of 0.117 W.

A commonly cited statistic for the accuracy of a 12 kHz long baseline system at 10 kilometers range is a precision of around 10 meters [21]. If this ratio is extrapolated out to 100 kilometers for a hypothetical lower frequency system, the accuracy of the acoustic solution would be around 100 m. Realistically, these systems are fairly nascent with the first demonstrations using the older narrow band 260 Hz 780 Hz RAFOS sound sources obtaining a navigation error on the order of 13 kilometers over a 150 kilometer under ice segment [27]. Proposed improvements to this system include using chip scale atomic clocks and broadband acoustic sources to mitigate some the errors present in the preliminary trials [26].

Thus the acoustic localization method meets the power requirements for the proposed deployment but requires further work to meet the localization error requirements and has limited flexibility past the initial sound source location. Additionally, the sound sources would have a limited life span which could be accelerated due to premature loss.

### 1.3.2 Geophysical

Geophysical techniques are a suitable alternative to acoustic methods for bounded error position fixes. Limitations of this method are the sensor power required, processing for the position estimation algorithm and divergence in regions of low parameter variance. Also, existing digital parameter models must be used for the type of mission described in the research problem of a single trajectory out and back as SLAM techniques would have no opportunity for loop closing or significant measurement overlap.

For the Labrador Shelf there are several publicly available bathymetric DPMs. One is the GEBCO08 which has a resolution of 30 arc seconds [42]. An extension of the GEBCO08 is the GMRT which uses the GEBCO08 as a base and incorporates multibeam swath bathymetry where it is available [6]. A further 30 arc second global model released at around the same time is the SRTM30 plus which includes satellite based altimetry [43]. The ETOPO1 1 arc minute global model is also available although it uses the GEBCO data for the Labrador Shelf region [44].

Sections crossing the shelf using geophysical techniques should be located such that there is sufficient variance to allow convergence of the algorithm. The bathymetric variance in the GMRT for the Labrador shelf was evaluated as in Fig. 1.7.

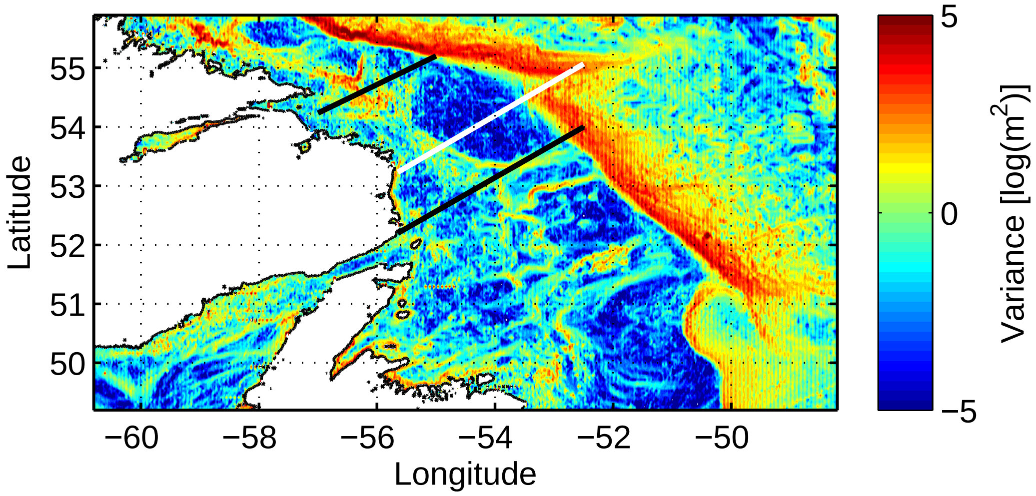

Figure 1.7: Digital parameter model variance shown on a log scale with warmer colors indicating higher variance and cooler colors lower variance. Possible locations for track-lines are shown as black lines. The Seal Island section from the Atlantic Zone Monitoring Program is shown in white.

This evaluation was performed by drawing 100 normally distributed samples around each grid cell with a variance of $\sqrt{200}\ m^2$, computing the water depth from the GMRT using bilinear interpolation and using these values to compute the terrain variance. While a high degree of terrain variance computed in this manner does not equate to adequate performance using the a terrain aided navigation technique, it does show where it is likely to not work well as represented by the regions of low terrain variability. From this computation, the shelf break has a high degree of bathymetric variance as expected. Also, the inner shelf, marginal trough and edges of the saddle regions show a high degree of variability. The example track-lines shown in Fig. 1.7 are located over regions with a high degree of terrain variability while also attempting to align with historical records.

While DPMs with a grid cell size of up to 120 meters have shown to be useful in terrain aiding [4], the available DPMs for the Labrador Shelf have a resolution of 2 kilometers. However, the prior study in which the impact of grid cell sizes were evaluated was in a coastal region. It remains to be seen whether coarser grids may be used in a non-coastal environment. If coarser grids are not able to be used then higher resolution DPMs for the track-line area would need to be collected.

Another limitation of bathymetric methods is the need to be within range of the bottom to receive a viable return. Slocum underwater gliders have ballast pumps with 30, 100, 200, 300 and 1000 meter maximum depth ratings and an altimeter with a maximum range of around 100 meters. Thus the maximum water depth for bathymetric aided navigation with a Slocum glider using its altimeter is 1100 meters.

Magnetic or gravimetric relative navigation techniques may be a suitable augmentation for relative localization when the bottom is out of range of acoustic sensors or when the bathymetric DPM is too coarse or flat. Power requirements for magnetic sensors are reasonably low while gravimetric sensors of the necessary precision presently require too much power and are too large.

There are several sources of publicly available global magnetic DPMs [45, 46]. These compilations are from shipborne, aeromagnetic and satellite measurements, are levelled to a constant altitude of 5 kilometers and have a resolution of 3 arc minutes. Another recent global model, the EMAG2, has a grid cell size of 2 arc minutes and is leveled to 4 kilometers above sea-level [47]. Sources of regional magnetic DPMs include the Magnetic Anomaly Map of North America and further regional models available at local repositories [48].

Aeromagnetic surveys typically provide reasonably high resolution DPMs of the terrestrial magnetic signatures as the sensor source separation is relatively low. Aeromagnetic surveys of marine areas suffer in this regard because the sensor-to-source separations are necessarily constrained by the surface of the water. There have been some successful marine surveys with deep magnetic tows, where the magnetic sensor is towed at a fixed altitude from the seafloor [49, 50]. Additional surveys have utilized AUVs for high resolution surveys of sea mounts and other mid oceanic spreading region features [51].

The use of underwater gliders for magnetic measurements presents several unique challenges which have to be overcome prior to their use as a relative navigational aid. The glider's profiling causes a variable sensor-to-source separation which may require either leveling of the data prior to comparison with a DPM or a DPM which has a depth dimension as well. Additionally, the glider's pitch adjustment mechanism is a moving battery pack which contains ferrous materials and distorts the magnetic measurements. The glider itself also contains other fixed magnetic disturbances. These effects require calibration to remove their disturbance from the magnetic measurements. Due to these challenges with measurement techniques and DPM availability the use of magnetic measurements as a relative navigation aid has been limited to simulation. These simulations have shown promise in constraining the error growth, especially in areas of the terrain that lack sufficient variability or where the water depth exceeds the range of the sonar device [38],[37].

## 1.4 Case Study for Under-Ice Navigation

A potential underwater glider program operating year round on the Labrador Shelf and into the Labrador Sea faces the challenge of navigating under seasonal sea ice. Additionally, to move from limited depth profiles in a coastal environment to full depth profiles past the shelf break requires new strategies to effectively manage the energy usage between the ballast system and the hybrid propeller drive. To evaluate the possibility of such a program a case study is proposed involving three phases.

### 1.4.1 Phase I: Ice Free Operations

The first phase is a glider data collection phase whereby the gliders are deployed throughout the ice free season to collect data along the track-lines. These initial deployments would build the skill of the operators, technicians and other personnel involved in their deployment and allow the evaluation of the geophysical navigation methods through post-processing of location estimates [4]. The suitability of the available DPMs may be evaluated against the collected glider data. During this phase the use of an acoustic localization method is desirable to both provide baseline measurements for the evaluation of the geophysical navigational methods and to evaluate the performance and robustness of the acoustic localization aids. Additionally, the need for hybrid thruster assisted profiles or horizontal segments in order to save energy may be evaluated here.

### 1.4.2 Phase II: Digital Parameter Model Refinement

Depending on the outcomes of Phase I, further refinement of the DPMs may be necessary. A suitable survey size for this work could be considered as a swath 5 kilometers wide across the shelf and 300 kilometers long out to the shelf break. For a ship based bathymetric survey of this area using nominal hull mounted multibeam sonar with a track-width of seven tenths the water depth corresponding to a swath angle of 45 degrees, a nominal water depth of 300 meters, and a survey speed of 10 knots, the survey would take approximately 2 weeks. In this survey the track-line spacing is around 200 meters with some small amount of overlap. An alternative to a ship based survey is the use of a long range autonomous surface vessel like the wave glider by Liquid Robotics [52]. The wave glider can handle moderate payload energy requirements and moves at nominal velocities of one knot. The benefit of this platform is lower cost relative to the ship based survey. Although the same survey of the target region may take 40 weeks for a single platform, by using two platforms the survey may be completed in a single ice free season. Additionally, the wave gliders may act as tending vessels to provide acoustic baseline measurements to the underwater gliders while they are collecting their phase I data.

### 1.4.3 Phase III: Under-Ice Operations

Building upon the operational experience gained in Phase I and using the refined DPMs generated in Phase II, the under ice operations may commence. In this phase the underwater gliders would be deployed prior to freeze up and be recovered after breakup. Depending on the findings of Phase I and II acoustic navigational aids may still be needed for key areas where there is insufficient information from the DPMs. In this way year round observations of the Labrador Shelf using underwater gliders may be achieved.

## 1.5 Contributions

This work presents the following contributions toward realizing the goal of long distance autonomous underwater glider operations in surface denied regions:

1. A review of the state of the art in long range autonomous underwater vehicles, in navigational methods for these vehicles and in magnetic measurement and calibration techniques.
2. A state feedback depth controller with proportional and integral terms where the gains are computed using an energy optimal method.
3. A method for terrain aided navigation of an underwater glider including offline evaluations and open loop online tests.
4. A system for performing magnetic measurements using an underwater glider including a calibration method for correcting these magnetic measurements.

The key contribution of this thesis is the method for terrain aided navigation of an underwater glider which lays the groundwork for the observational case study outlined in Section 1.4. Additionally, the magnetic instrumentation and calibration methods included in this thesis show promise towards augmenting the terrain information with magnetic anomalies.

# Chapter 2

# Literature Review

An overview of the state of the art in long range autonomous underwater vehicles (AUVs) is presented followed by an in depth review of their navigational methods. Additional consideration is also given to magnetic measurement and calibration methods using underwater vehicles.

## 2.1 Autonomous Underwater Vehicles

### 2.1.1 Underwater Gliders

The concept of underwater gliders was initially motivated by the scientific drive to better understand the subsurface layers of the world's oceans. This desire was shown through initial development of ocean floats by Stommel and Swallow [53], [54]. These floats, through many iterations, developed into the Autonomous Lagrangian Circulation Explorer (ALACE) floats as a part of the world ocean circulation project [55]. Slightly before this, Douglas Webb, who had been heavily involved in the float development, conceived the original concept for an underwater glider as a type of controllable profiling float. Discussions of this concept with Henry Stommel led to their vision of the glider's role in oceanographic research as a portrayal of a future world control center for gliders [56].

Several years later the first revision of what later became the Slocum glider was developed as a variation of a profiler with controllable fins which allowed for gliding motions and therefore, a horizontal motion component in addition to the vertical motion component [57]. Webb's original plan was to develop a glider with a thermal engine, capable of harnessing the sharp temperature gradient found in much of the oceans to cause buoyancy differences large enough to sustain gliding motion [58]; however, due to the complicated nature of the thermal engine, electric versions of the Slocum gliders were developed to expedite product development [59, 60, 61]. Concurrent to this development, other notable gliders were developed including the Spray glider at the Scripps Institute for Oceanography and the Seaglider at the University of Washington [62, 63]. The Spray glider was originally developed as an autonomous profiling float and the Seaglider as a virtual mooring capable of long term monitoring of critical locations. These three gliders were the first commercially available underwater gliders and reviews of their capabilities can be found in [64, 65, 66, 67, 68].

Additional glider platforms have emerged to fill slightly different roles. The wave glider, which is a surface platform that utilizes wave energy as its primary propulsive force [69, 70]; the Sea Explorer underwater glider which has a larger ballast drive and rechargeable lithium batteries [71]; and the Exocetus glider is another new glider platform which is larger and potentially faster than the original three underwater gliders [72].

### 2.1.2 Long Range Vehicles

Alongside underwater gliders, larger long range vehicles are being developed to fill the gap between traditional survey grade AUVs and underwater gliders. One notable example of this is the Long Range Autosub (LRA) 6000 AUV which extends the Autosub family of vehicles with a new version that has a range of 6000 km [73, 74, 75]. The Tethys AUV developed by MBARI is another recently developed long range platform which has seen significant field trials [76]. The Tethys platform effectively merges some of the most successful components of underwater gliders with that of AUVs, using internal mass shifting and ballast systems typically found on underwater gliders and the larger battery capacity, propeller drive and higher power sensors typically found on AUVs.

### 2.1.3 Under-Ice Operations

There have been a small number of AUVs which have specialized in under-ice missions. The most notable of these from a Canadian perspective is the Theseus AUV from International Submarine Engineering [77]. The Theseus vehicle was developed under contract from the Defense Research Establishment Atlantic of the Canadian Department of National Defense to lay fibre-optic cables in ice covered waters [78]. Initially developed to have a range of around 400 km, it has evolved to being capable of a range of over 1360 km with a depth rating of 2000 m [79]. The Theseus vehicle remains one of the few AUVs specifically designed and successfully used in under-ice deployments. The success of the Theseus vehicle has prompted under-ice missions with the MUN-Explorer vehicle in 2009 [80]. These missions came as a precursor to two additional Explorer class vehicles being contracted by the Canadian government for use in an under-ice survey of the Canadian Arctic ridge to establish Canada's claim to the Commission on the Limits of the Continental Shelf through the United Nations Convention on the Law of the Sea [81, 82].

The Autosub Under-Ice program is another notable under-ice AUV exploration program. The Autosub under-ice program was a 5-year program funded by the National Environment Research Council in the United Kingdom to bring together scientists and engineers to study ice-shelf and ocean interactions and the impact they have on the climate. This program collected a significant amount of data on the under-ice properties in Arctic waters [83], [84]. The use of the Autosub platform for under-ice missions also prompted significant investigation into under-ice AUV risk of loss assessment after the loss of one of the Autosub vehicles under the Ross Ice Shelf [85].

Underwater gliders have also begun to see operational use in both polar regions. A recent observational program in the Davis Strait has successfully navigated Seagliders under marginal ice cover using low frequency acoustic navigational aids [27]. Slocum gliders have also been successfully deployed in Marguerite Bay, Antarctica in marginal ice, although without the use of additional navigational aids [86].

## 2.2 Navigational Methods

The majority of navigation techniques require a system to maintain a sense of orientation and location within a given frame of reference. Existing methods for underwater navigation may be grouped into geophysical, acoustic, inertial and model based techniques. Several recent survey papers by Kinsey et al. 2006, Sutters et al. 2008 and Paull et al. 2014 [21, 22, 23] summarize much of the state of the art in underwater navigation.

### 2.2.1 Acoustic Navigation Systems

Acoustic aids to navigation are widely used in precision surveys using underwater vehicles. One of the more popular and earliest developed techniques for underwater acoustic navigation is the long baseline system (LBL) [87]. Long baseline navigation requires several acoustic transponders with known locations on the sea floor as illustrated in Fig. 2.1.

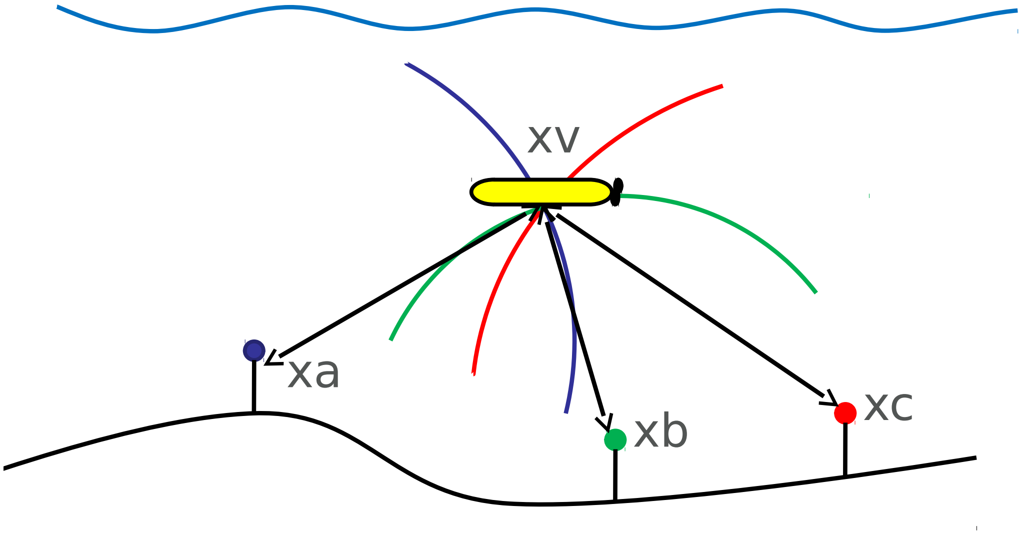

Figure 2.1: Long baseline acoustic navigation with three transponders and an underwater vehicle. Ranges based on the two way travel times are shown by the red, blue and green arcs. The intersection of these three ranges gives the location estimate for the underwater vehicle.

The vehicle estimates its location relative to these transponders and therefore relative to the earth frame using range measurements based on the return time of an acoustic query, knowledge of the transponder locations and the vehicle depth measurement. Standard accuracies achievable with these systems are around 0.1 to 10 meters depending on the range from the beacon, which can reach up to 10 kilometers horizontally, beacon motion, acoustic frequency and speed of sound variations among others [88]. This system provides bounded error positioning but usually with a low update rate, depending on the two-way travel time. Navigation techniques with higher update rates are used to provide positioning information between fixes. These higher update rate methods often are subject to drift, making the combination of these two methods well suited to various sensor fusion techniques. Some recent field trials have demonstrated the utility of LBL systems for aiding an AUV under Arctic sea ice [89] as well as a Seaglider [90]. Recent theoretical developments have been shown to improve the accuracy of these systems through direct inclusion of the range measurements in the estimation algorithm as well as some convergence proofs [91].

A slight variation of the LBL technique is the short baseline (SBL) system. In an SBL setup, the transponders are located at the extremes of the ship or on a bottom mounted external frame [42]. This type of system is generally used when fixed moorings are impractical or to reduce the number of locations which need to be surveyed in. In general the ranges for these systems are lower than an LBL system due to the geometry of the system.

Another variation is the ultra short baseline (USBL) system [92, 93, 94]. In this setup the vehicle measures range and bearing to a single beacon. The position of the AUV may be determined by the USBL system relative to the beacon. If the beacon's position is known or it is able to send its position to the AUV, the AUV is able to localize itself as shown in Fig. 2.2

A USBL setup gives relatively good fixes over a short distance, however, because the position of the vehicle requires the calculation of the bearing to the source its accuracy falls off very quickly with distance. The USBL system is generally used in docking or in maneuvering in tight quarters around fixed installations. It may also be used for orientation estimation if multiple USBL transponders are installed on a vehicle [95].

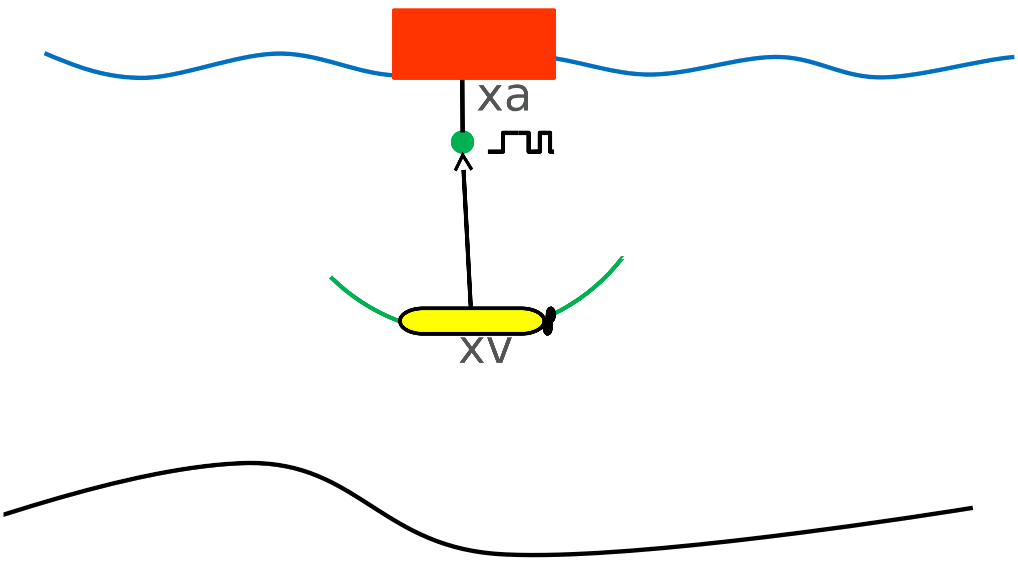

Figure 2.2: Ultra short baseline acoustic navigation with a single set of transponders and an underwater vehicle with acoustic communications. The range and bearing to the underwater vehicle are used by the surface vehicle to track the underwater vehicle. The location estimates are then sent to the underwater vehicle.

Other approaches to underwater localization have tried to mirror the success of the Global Positioning System (GPS) to underwater vehicles. The first proposed system was to replicate the GPS signal underwater using buoys equipped with differential GPS and acoustic modems [96]. Any vehicle in range of the signal could then compute its local position. Another approach has been to synchronize the clocks of surface buoys with the AUV and have the buoys receive an acoustic signal from the AUV which is transmitted on a known schedule. The buoys, by communicating with each other, could then determine the position of the AUV. This system was suited only for tracking of the vehicle [97], [98].

Developing out of this tracking system, a promising area of recent research has been in synchronous one way travel time (OWTT), also termed underwater transponder positioning or synthetic long baseline among others [99, 100, 101, 102, 103, 91].

Generally, in these systems, the transmitter and receiver have precision synchronous clocks. The transmitter sends acoustic pulses on a predetermined schedule. The receiver then calculates the travel time based on the schedule. The AUV can calculate its position through range measurements to a single source if either itself or the source is moving such that the intersection of those ranges is solvable, however, multiple sources increase the fidelity of the system. If the source position is available through acoustic modem link then the vehicle position may be calculated in the inertial frame as shown in Fig. 2.3

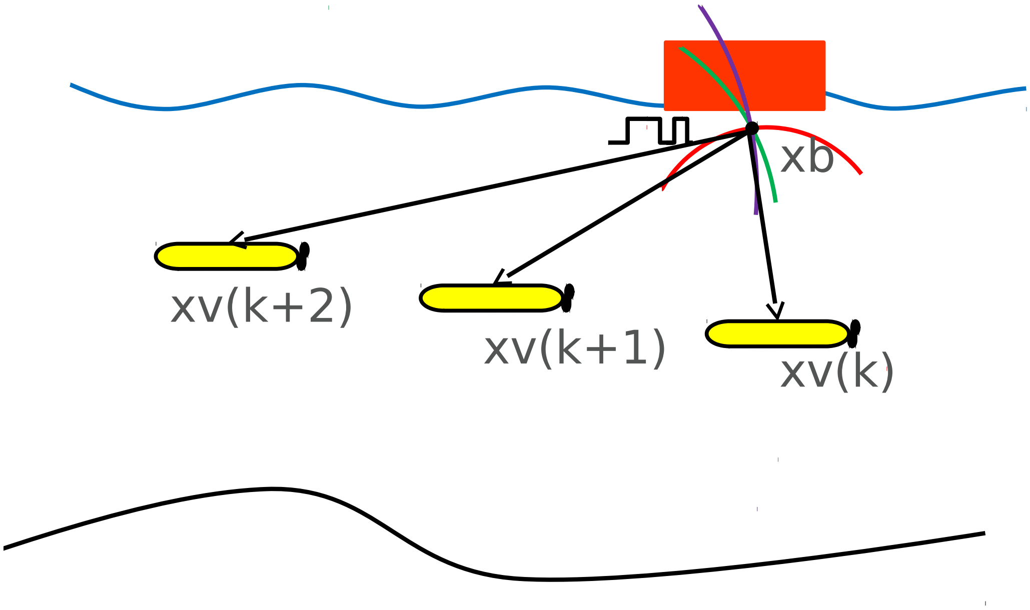

Figure 2.3: Single beacon navigation using synchronous clocks which allows the underwater vehicle to compute a range to the source based on a schedule. If the vehicle or the source are moving relative to each other the location of the source may be estimated. Subsequently, if the source location is transmitted to the underwater vehicle through an acoustic link, the vehicle may determine its location.

The errors inherent to this setup are largely due to clock drift and uncertainties in the water properties which affect the sound speed profile. Demonstrations of this technique have been successful at up to 11 km over the course of a several day deployment [104]. However, progress has also been reported toward long range localization of AUVs over hundreds of kilometers [105, 27].

The cooperation of multiple AUVs has also been demonstrated as a method to increase the accuracy of localization estimates [106, 107]. In these systems one vehicle with a higher accuracy location estimate may communicate with other vehicles with lower accuracy location estimates to decrease their localization error. In this arrangement all of the vehicles in the group need not have precision navigation systems, decreasing the cost of the fleet.

### 2.2.2 Inertial Navigation

Inertial navigation is a general term for a collection of techniques which use measurements of the body accelerations and angular rates of the vehicle to determine the relative change in position and attitude. These methods are based on integrating these measurements which results in drift over time due to time varying biases. The errors present in inertial navigation systems (INS) are typically characterized by percent per distance traveled. When aided by a Doppler Velocity Log (DVL), a commercial grade INS might have a drift of 1 percent per distance traveled whereas a tactical grade system based on laser ring gyros or fiber optic gyros might have a drift of 0.05 percent of distance traveled. These two systems differ greatly in their cost, power requirements and size with the more accurate system requiring more of each. The trend in these systems is to lower power and higher accuracy, with significant progress towards systems which achieve tactical accuracy at low power and size [108].

Statistical estimators are often used in INSs to improve the position and attitude information. These estimators include Kalman filters for linear Gaussian systems, extended Kalman filters in which a non-linear system is linearized and a wide variety of non-linear filters which make no attempt to linearize the system [109]. All of these filters attempt to use a statistical distribution of the measured variables to improve the estimates of the position and attitude.

Many inertial navigation algorithms incorporate data from non-inertial sensors to help mitigate the drift rate or to reset the accumulated navigational error. A DVL, which measures the speed over ground, is a commonly used acoustic sensor for limiting the drift rate [110]. A limitation of this sensor is its range which is typically around 100m for a sensor of an appropriate size to fit on an AUV. When the DVL is out of range of the bottom, or without "bottom lock", the DVL provides no speed over ground information to the filter. There have been some recent results which correlate the water velocity measurements made by the DVL during subsequent pings to back propagate the speed over ground downwards from the surface estimates due to the GPS and upwards once bottom lock is achieved [111, 112]. Other methods include many of the acoustic localization techniques, such as LBL, OWTT and USBL systems, to provide a bounded error position estimate which is incorporated into the position and attitude estimator to reset the accumulated error [21].

### 2.2.3 Model Based Navigation

Model based navigation uses knowledge of the vehicle's state to measure its relative change in location. One form of this is dead-reckoning which has its roots in surface navigation whereby a ship would know its longitude based on the ship speed and the time it had traveled. On a sailing vessel one of the first instruments to measure ship speed was a line attached to a sea anchor which was played over the side. The time at which knots in the rope passed was used to find the speed of the vessel. This speed was combined with the ship's clock, originally an hourglass, to achieve a crude knowledge of the distance traveled. Once propellers began to be used for propulsion of vessels the revolutions per minute of the propeller was used to ascertain the ship speed. This method has been transferred to basic controllers for underwater vehicles.

Underwater gliders navigate by combining the depth rate and vehicle pitch angle to calculate the horizontal velocity. This technique is a simple form of model based navigation as it does not take any other inputs, such as actuator positions or hydrodynamic coefficients, and is subject to drift due to ocean currents as it only provides information relative to the water not the ground. To mitigate the sometimes significant drift, underwater gliders surface periodically to obtain GPS locations.

More sophisticated models for aiding navigation can be grouped into combinations of linear and non-linear controllers with fixed or adaptive models [113]. Fixed parameter models suffer from poor performance if the model parameters are inaccurate while adaptive models provide relatively decent tracking without the need for accurate identification of parameters [114]. However, an accurate fixed parameter model has been shown to outperform adaptive models during highly non-linear events such as thruster saturation [115]. Sliding mode controllers have also been shown to be effective for certain problems where the fixed parameter model coefficients are allowed to vary in accordance with a control law [116, 117]. Model predictive controllers have also shown their utility in estimating vehicle attitude and locations [118]. The majority of models presented in literature simplify the state space to 3 degrees of freedom to simplify the number of model parameters required. Additionally, cross terms are usually neglected due to the difficulty in obtaining accurate estimates of these parameters [119].

Model based techniques require all of their effort up front either in the collection of the parameters or in developing the adaptive model gains to be suitable to extract the parameters. However, once developed the model based navigation method does not require significant power as it is not based inherently on additional navigation sensors, although the actuators and attitude must be instrumented if they are not already. If speed over ground is not available the model based method is subject to uncertainties due to ocean currents. Speed over ground is available from DVL sensors or in some cases a model may be capable of estimating the speed given certain maneuvers [120].

### 2.2.4 Geophysical Navigation

Naturally occurring potential sources of information suited to relative navigational methods include geophysical phenomena and features such as gravimetric, geomagnetic, visual and bathymetric data. Relative navigation techniques rely on feature variability in past measurements which is compared to a map. Statistical estimators are then used to generate an estimate of the current position of the vehicle given prior measurements. This data is often used in conjunction with model based or inertial navigation techniques to bound the error drift which is present when these methods are used alone.

Terrain aided navigation (TAN) methods make use of pre-existing bathymetric maps to help bound the position error of an AUV through comparisons with water depth measurements. Successful applications have included the use of single beam altimeters, multibeam SONARS, acoustic doppler current profilers and other acoustic arrangements that allow for estimates of the water depth [28, 29, 30].

The majority of these demonstrations use the existing fused navigation solution from a high accuracy inertial navigation system (INS) aided by a DVL as an input to the TAN algorithm [31]. This high accuracy navigation update is then combined with the water depth measurement update from a multi-beam sonar or DVL [32, 33].

However, it has recently been shown that lower grade inertial sensors aided by a DVL may be used by directly including the inertial and DVL measurements in the filter used for the terrain aided navigation [34]. This tight coupling has the effect of increasing the number of states in the TAN filter, but also preserves the reliability and accuracy of the high accuracy DVL aided INS TAN methods.

General limitations of TAN techniques are due to the range of the acoustic sensors that is typically on the order of 100 meters, depending on the transducer. Additionally, low terrain variability, which increases the uncertainty of the estimate, and the power requirements of the sensors are limiting factors.

In the absence of a-priori knowledge of the bathymetry, simultaneous localization and mapping (SLAM) techniques may be a viable alternative [121]. A large body of work has been dedicated to this topic in terrestrial robots [122, 123]. However, the unstructured underwater environment poses challenges for this technique. This method of navigation performs well with areas that have recognizable features and requires overlap in the data collection process to reduce the estimation error. Successful implementations of this technique underwater have been demonstrated using acoustics where the vehicle loops back on its trajectory to provide the necessary overlap [124]. Another successful implementation uses visual still frames where the frame rate is high enough to provide enough overlap between pictures [125]. More recently an adaptation of bathymetric SLAM using trajectory maps has been demonstrated [126].

To overcome the limitations of sensor proximity and terrain uniformity in bathymetric aiding techniques, gravimetric and geomagnetic information have been proposed as aids to navigation [35, 36]. The proposed methods rely on the same methods as the bathymetric techniques with the exception that they may be sensed ubiquitously in the underwater environment. They have the additional benefit of varying in three dimensions allowing for a higher degree of uniqueness in each measurement. In the case of gravimetric aiding the sensor accuracy required has limited its use to military applications due to the large power and space requirements for sensors meeting these needs [127], [128], [129]. Magnetic sensors meet the power and space requirements for underwater vehicles but have not found great use in underwater navigational aids beyond as a heading reference due to calibration and measurement challenges [130], [131]. Recent efforts in providing vector based calibration methods for magnetometers have met with some success in bringing the large number of measurement distortions under control [132]. Additionally, gradiometric measurements have mitigated much of the issues involved with the secular drift (time variance) [133], [134]. Several simulations have been presented to date using pre-recorded data as a map for navigational underwater aiding [37], [38]. To the best of the author's knowledge there has been no practical demonstration of magnetic or gravimetric aided navigation aiding for an AUV to date.

## 2.3 Magnetic Measurements and Calibrations

Magnetic measurements of the earth's main field have found use in a variety of subject areas including but not limited to characterization of the earth's crust, searching for unexploded ordinance and as a heading reference. Using magnetic field measurements for relative navigational methods has been proposed previously but has yet to have a practical demonstration. For integration into a long range underwater vehicle for the purpose of magnetic aided navigation, a potential sensor must be lower power, small and accurate. Additionally, any sensor which is integrated into an underwater vehicle requires calibration to remove the effect of the sensing platform from the measurements. Further, for a magnetic measurement to act as a relative navigational aid there must exist prior surveys of the magnetic field of sufficient accuracy and resolution.

### 2.3.1 Magnetic Sensing

Until around the turn of the 20th century, measurements of magnetic fields were performed by measuring the orientation of a magnetized needle fixed to a fine line [135]. During the Second World War rapid progress was made on the development of magnetic fluxgate sensors for the detection of submarines [136]. Magnetic fluxgate sensors have since matured into low power, stable devices with resolutions down to 10 pT which measure the magnetic field in its orthogonal vector components [137]. This resolution is contrasted with the total field magnitude of around 50 uT, for a signal to noise ratio of 500,000 to 1.

Another capable technology for measuring magnetic fields is based on proton precession [138]. A common variant of these proton magnetometers is based on a Cesium vapour cell which has recently been successfully miniaturized by the United States' National Institute of Standards and Technology [139, 140]. This miniature version, termed the micro-fabricated atomic magnetometer (MFAM) is being commercialized by Geometrics and the initial version provides a 1 pT resolution at 2 W [141]. A recent application note by Geometrics has noted that they have successfully begun demonstrations of this system on a Gavia AUV [142].

Other techniques for magnetic sensing include magnetoresistive devices, which are widely used in micro-electromechanical systems (MEMS) as chip level heading references, superconducting quantum interference devices (SQUIDs), nuclear magnetic resonance and hall effect devices [135]. However, to date these methods have not resulted in devices which are suited to integration into underwater vehicles for the purpose of long term, high accuracy magnetic measurements of the earth's main field and its variations.

### 2.3.2 Magnetic Calibrations

Measurements of magnetic fields must be calibrated to remove the effects of the sensing platform and to correct for the non-linearity of the sensor. These effects can be due to electrical currents, hard and soft magnetic effects and temperature variations among others. Recent methods have found success through estimating the parameters through batch estimation in which a series of calibration measurements are performed periodically throughout the measurement regime. Calibration parameters are then extracted using the set of measurements through vector or scalar methods.

Vector calibration methods attempt to preserve the three vector components of the magnetic field measurement in the earth frame [143, 144]. In these methods the platform is maneuvered in a figure eight pattern to provide an unbiased representative sample. The measurements are subsequently rotated to the earth frame and the calibration coefficients are extracted through a least squares fit to the data. The drawback of these methods is the requirement for a precise attitude reference such as a laser ring gyro or similar system which can be cost prohibitive both monetarily and in energy consumption.

Scalar methods, on the other hand, make use of only the magnitude of the magnetic field to compute the calibration coefficients resulting in the vector components of the magnetic field remaining in the sensor frame. Initial developments of batch scalar calibration methods of vector magnetometers in a laboratory setting were performed for the satellite industry [145]. These methods were verified through several years of measurements on the Orsted satellite through comparison of the calibrated vector magnetometer measurements with an onboard total field magnetometer [146]. Around the same time, a method termed the TWOSTEP algorithm was published for which initially the bias [147], followed by the complete set of calibration parameters are estimated [148] which were then refined through a Gauss-Newton iterative solver [149]. These methods saw quick adoption by marine magnetic survey groups with towed marine magnetometer systems calibrated through an initial lab calibration using these methods, followed by further calibration maneuvers in the field to refine the parameters [150, 151]. Developments of new methods for estimating ellipsoids from point measurements [152, 153, 154, 155] led to a further refinement of the TWOSTEP algorithm to a method based on a least squares estimation of ellipsoidal parameters [156]. This least squares method was then extended to a maximum likelihood estimator of the magnetic calibration coefficients [132]. Similar developments use an adjusted least squares method that includes a noise term to allow for unbiased estimates of the calibration parameters in sensors with higher noise floors [157, 158].

An extension to batch estimation has been proposed in which an initial estimate of the calibration parameters is obtained followed by real time adaptation of the parameters through non-linear estimators [159]. Further extensions have shown through off-line analysis compensation methods for a time varying bias due to onboard electrical currents [160], the presence of actuators with moving magnetic parts [161] and for a varying sensor altitude during the calibration run [162].

# Chapter 3

# Underwater Gliders

The Slocum underwater glider uses active ballast changes as its main propulsive force [66]. The ballast system is located in the nose of the vehicle and creates an upward or downward pitching moment, assisting in the change in pitch necessary to form a suitable glide path. A mass shifting mechanism attached to one of the battery packs acts as a vernier pitch adjustment mechanism to control the vehicle pitch to a precise angle. The cyclic positive and negative vertical motion due to the forces from the ballast system generates lift due to the wings and vehicle body which moves the vehicle forward when the vehicle pitch is within a certain range of values. For the Slocum glider, the pitch values which produce the most forward movement are in the region of 35 degrees [163].

Before deployment a glider's mass is adjusted such that the vehicle is neutrally buoyant in sea-water. Additonally, the mass is distributed to the zero trim condition such that the center of mass is directly below the center of buoyancy when the ballast system and the mass shifting are both in the center of their range. At this stage the glider user plans the mission by selecting appropriate way-points for the vehicle to navigate to as well as other vehicle parameters such as desired pitch, surfacing conditions and minimum altitude among others. During the mission the vehicle attempts to reach the way-points by moving forward in its cyclic up-down pattern and by servoing the rudder to control the bearing to the desired heading. If the vehicle reaches a surfacing condition such as hitting a way-point or being too long underwater, it will surface, obtain a new GPS fix, re-establish the range and bearing to the way-point and continue on its way. In this navigational scheme the vehicle tracks its progress to the way-points, using dead-reckoning while underwater.

## 3.1 Dead-reckoning

In general, dead-reckoning systems keep track of the location of a vehicle through integration of the estimated vehicle velocity over time starting from a known initial condition. On an underwater glider this is accomplished discretely by using an initial location and adding the incremental displacements given by the product of the vehicle velocity and the time difference between measurements. The glider's dead-reckoning system uses the pressure and attitude sensors to estimate the horizontal velocity components. To that end the total vehicle velocity $v_A$ is computed by

$$v_A = \frac{v_z}{sin(\xi)} \tag{3.1}$$

where $v_z$ is the vertical velocity as given by the first derivative of the vehicle depth, measured by the pressure sensor, and $\xi$ is the glide path angle as shown in Fig. 3.1.

The glide path angle $\xi$ is composed of the vehicle pitch $\theta$ and angle of attack $\alpha$ as in

$$\xi = \theta + \alpha \tag{3.2}$$

In older versions of the vehicle control software the angle of attack was not in-

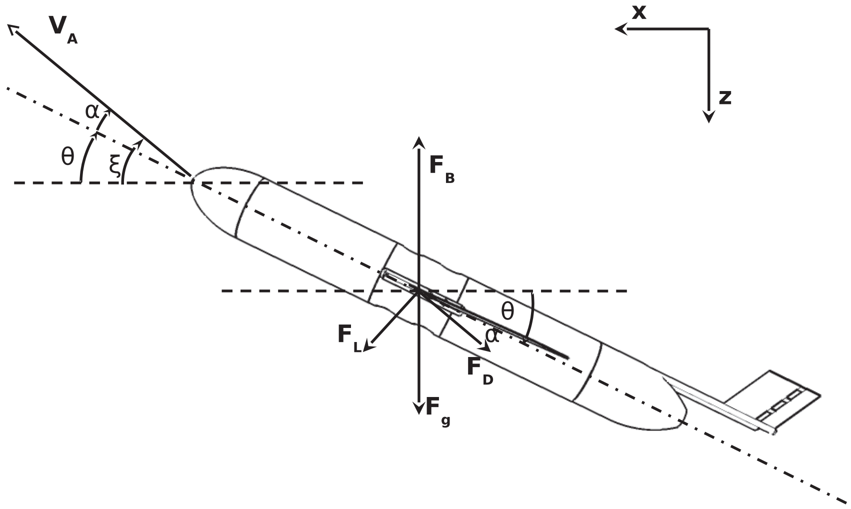

Figure 3.1: Free Body diagram of the forces experienced by the glider and the relevant angles where $\xi$ is the glide path angle, $\alpha$ is the angle of attack, $\theta$ is the pitch angle, $F_B$ is the buoyant force, $F_g$ is the gravitational force, $F_D$ is the drag force and $F_L$ is the lift force

cluded in the glide path estimate resulting in the vehicle pitch being the same as the glide path angle. However, more recent versions of the vehicle software include an optional estimator which can estimate an angle of attack based on the hydrodynamic parameters and measurements of the vehicle pitch and depth rate [164]. The vehicle velocity may be rotated to the horizontal plane and multiplied by the time between measurements $\Delta\mathbf{T}$ to produce the position updates $\Delta\mathbf{x}$ as in

$$\Delta\mathbf{x} = \Delta\mathbf{T} v_A \mathbf{M}(\phi, \xi, \psi + \delta) \tag{3.3}$$

where $\phi$ is the vehicle roll, $\xi$ is the glide path angle, $\psi$ is the vehicle magnetic heading, $\delta$ is the magnetic declination, and $\mathbf{M}$ is a rotation matrix from the vehicle to the inertial frame. The resulting dead-reckoning equation adds the position updates from

Eqn. 3.3 to the prior location estimate as in

$$\mathbf{x}_{k+1} = \mathbf{x}_k + \Delta\mathbf{x} \tag{3.4}$$

where $k$ is the time step related to $\Delta\mathbf{T}$ and $\mathbf{x}$ gives the vehicle location in the local coordinate frame. The dead-reckoning scheme for underwater gliders described above is functional for profiling missions with ready access to the surface for GPS updates. However, as the vehicle has no direct measurement of its speed over ground the accuracy of its velocity estimates are subject to a-priori unknown and changing water velocities. The vehicle attempts to compensate for this by assuming these water velocities are solely responsible for the difference between the dead-reckoning location and the first GPS fix upon surfacing, computing a depth averaged water velocity estimate based on this difference and the time between surfacings. This depth averaged water velocity estimate is then used as a corrective term to the vehicle velocity estimate in the next dive cycle. In highly stratified or dynamic areas of the ocean this assumption breaks down and as such the dead-reckoning algorithm can be subject to significant error. Additionally, in regions where surface access is denied this water velocity estimation method is not possible, resulting in a further degraded dead-reckoning solution.

# Chapter 4

# Energy Optimal Depth Control of a Hybrid Glider

The efficient control of a propeller driven vehicle in the vertical plane is a key component of its ability to perform long duration missions. For a gliding underwater vehicle the performance of its transit is a result of fixed vehicle parameters such as its lift, drag and ballast tank volume and mechanical efficiency [165]. Due to these fixed parameters a gliding vehicle's transit efficiency is less affected by the vehicle's control system as it reaches stable steady state glides. For a propeller driven vehicle, however, the net buoyancy of the vehicle must be compensated for in order to control the vehicle to a desired depth. For vehicles which are trimmed to be neutral at a specific water density prior to deployment, a net buoyancy is still possible due to temporal and spatial variations in the water density from the target density. In this case, depth control may be accomplished through lifting surfaces or through ballast changes. For a vehicle which primarily controls the depth through lifting surfaces, additional energy is lost to the lift induced drag. For this reason it is desirable to command a neutral buoyancy through ballast changes to minimize the energy lost to the lift induced drag during long duration horizontal maneuvers.

A hybrid underwater glider, in which an auxiliary propeller propulsion system is added, is capable of controlling its depth through pitching the body of the vehicle or through ballast changes. Initial tests used the legacy drift at depth buoyancy controller to maintain a commanded depth [166, 167]. The use of the ballast system as the depth control mechanism provided unsatisfactory results due to the long rise and settling times, and depth dependent energy consumption. Subsequent tests where the mass shifting mechanism was used to control the depth through pitching the vehicle suffered from steady state depth and pitch errors due to mistrimmed and misballasted vehicles [2]. The steady state pitch errors result in a lift induced drag force increasing energy consumption of the vehicle for a fixed velocity maneuver. To compensate for these steady state errors an integral term has been added to the depth error to provide feedback to the mass shifting controller. Additionally, the buoyancy is incremented towards neutral if the pitch is above a threshold and the depth rate is low. However, tuning these controllers involves a lengthy manual process which needs to be performed after changes to the vehicle mass distribution or external components in order to maintain performance.

In this chapter the energy lost in vehicles with a net buoyancy is examined. Following, the background theory for a linear time invariant model and a state feedback controller for an underwater glider are presented. The state feedback controller is augmented with an integral term to account for mistrim and misballast conditions as well as density differences over a range of target depths. The resulting state equations are then re-written to the state error equations such that they are suited to the computation of energy optimal gains. The methods are verified through field trials in Holyrood Arm, Newfoundland. In these trials a set of system identification missions were performed and the energy optimal gains computed using the model generated from that data. These energy optimal gains were then used to control the depth of the vehicle to verify the performance of the methodology.

## 4.1 Energy Lost to Net Buoyancy

Underwater gliders with a net buoyancy require a corresponding lifting force to counteract that buoyant force while servoing the depth to a desired value. In a Slocum underwater glider this is achieved by pitching the vehicle, resulting in the required lift force but also increasing the drag of the vehicle. This increase in drag is termed the lift induced drag.

The energy lost to lift induced drag shows up either as additional propulsive energy needed to maintain the same speed or as a loss in speed in a constant propeller torque/speed control scenario. In either case a loss of performance is realised that results in a reduced range. From Graver (2005) the lift and drag coefficients for an underwater glider are dependent on the angle of attack of the vehicle according to [163]

$$C_L(\alpha) = 11.76\alpha + 4.6\alpha|\alpha| \tag{4.1}$$

$$C_D(\alpha) = 0.214 + 32.3\alpha^2 \tag{4.2}$$

where $\alpha$ is the angle of attack of the vehicle in radians. The lift force and drag force experienced by the vehicle are then given by

$$F_L = 0.5\rho C_L(\alpha) A V^2 \tag{4.3}$$

$$F_D = 0.5\rho C_D(\alpha) A V^2 \tag{4.4}$$

where $\rho$ is the fluid density, $A$ is the cross sectional area of the hull and $V$ is the vehicle velocity. A hybrid underwater glider performing a constant depth maneuver with a non-zero buoyant force requires an equivalent non-zero lift force $F_L$, requiring a non-zero $C_L$ and therefore non-zero angle of attack $\alpha$ as illustrated in Fig. 4.1 increasing the drag coefficient and thereby drag force.

The propulsive power required may be represented by

$$P_p = \frac{F_D V}{\eta} = \frac{1}{\eta} 0.5 \rho C_D(\alpha) A V^3 \tag{4.5}$$

where $\eta$ is the propulsive efficiency and $P_p$ is the propulsive power. In a constant propulsive power scenario the velocity of the vehicle is reduced from the zero angle of attack velocity $V_0$ to the constant propulsive power velocity $V_1$ according to

$$V_1^3 = \frac{0.214}{0.214 + 32.3\alpha^2} V_0^3 \tag{4.6}$$

In the constant velocity scenario the propulsive power required is increased from the zero angle of attack power $P_0$ to the constant velocity propulsive power $P_1$ according to

$$P_1 = P_0 + \frac{32.3\alpha^2}{0.214} P_0 \tag{4.7}$$

The range of a hybrid underwater glider may be computed according to [168]

$$R = \frac{EV}{P_p + P_h} \tag{4.8}$$

where $E$ is the energy stored in the batteries and $P_h$ is the base power required by the sensors and vehicle systems. For a Slocum electric glider with alkaline batteries the nominal energy is 7.8 MJ which is derated based on operation temperature, age and other factors. For operations in Newfoundland the nominal energy is conservatively

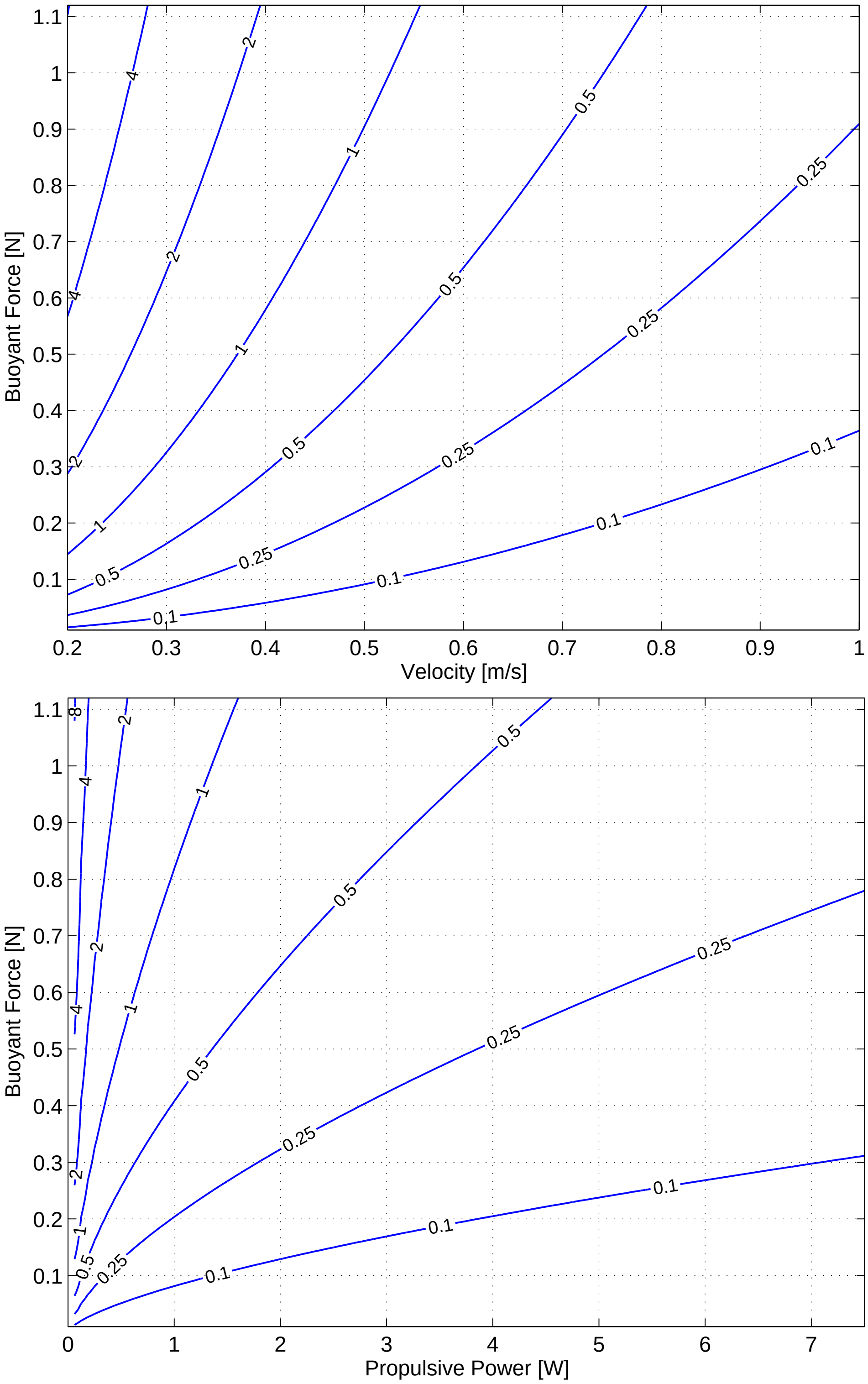

Figure 4.1: Angle of attack in degrees for a hybrid underwater glider for a range of buoyant forces where the velocity is held constant (top) and power is held constant (bottom) during horizontal flight modes.

derated by half because of the cold water temperatures. The base power consumption for the same glider with a CTD is around one watt. For these operational parameters the loss in range for a constant velocity or propulsive power control scheme is illustrated in Fig. 4.2.

Alternatively, the range lost expressed as a function of the total distance traveled by the vehicle given the energy and power usage described above is illustrated in Fig. 4.3.

The constant velocity scenario results in a maximum loss in range of over 60 km or around 10.0 percent of the total range at the speed of 0.2 m/s and the worst net buoyant force of 1.125 N. The constant propulsive power scenario results in a maximum loss in range of over 128 km or 32 percent of the total range at the lowest power considered of 0.1 W and the worst net buoyant force of 1.125 N. The constant velocity scenario results in lower range loss than the constant power scenario, especially at slower speeds and larger buoyant forces. This difference at slower speeds and larger net buoyant forces is due to the loss in velocity in the constant power scenario resulting in the base power becoming more significant in the range reduction. In both of these scenarios, however, the energy lost to the lift-induced-drag is a significant portion of the overall energy budget at speeds of less than 0.5 m/s or powers of 1 W and buoyant forces greater than 0.75 N. For comparison purposes an underwater glider of 50 kg ballasted to be neutral in seawater with a density of 1025 kg/m$^3$ would experience a 0.75 N buoyant force for a change in water density of 1.57 kg/m$^3$ . The range of density values a vehicle can experience are heavily location and season dependent, however, it is not uncommon for a vehicle to observe density variations on the order of 4 to 6 kg/m$^3$ over the course of a month long deployment. A methodology which controls the buoyancy to neutral while also controlling the vehicle's depth is therefore desirable.

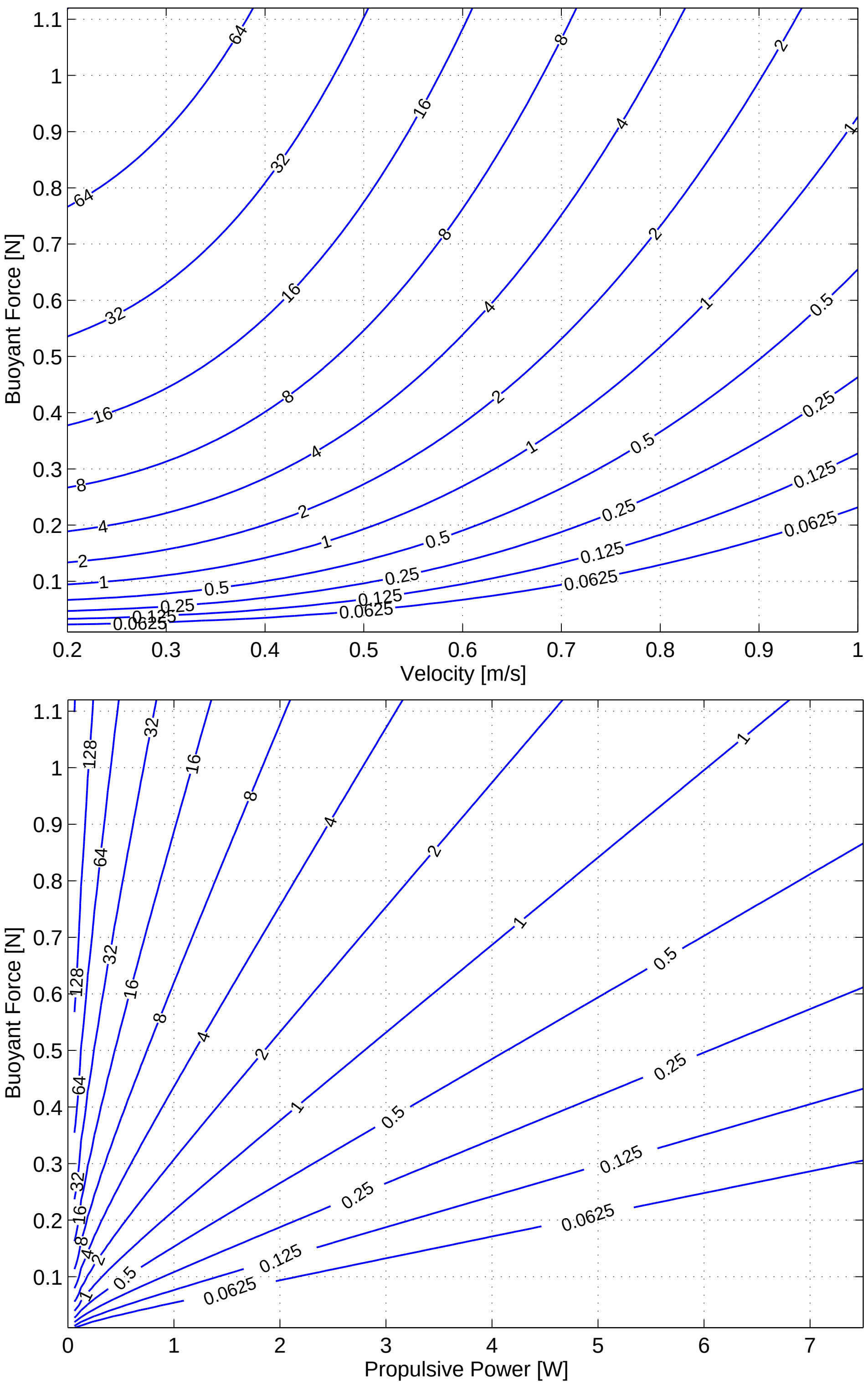

Figure 4.2: Range lost in kilometers due to lift induced drag as a result of buoyant force where the propulsion control scheme operates on a constant velocity principle (top) or a constant propulsive power principle (bottom)

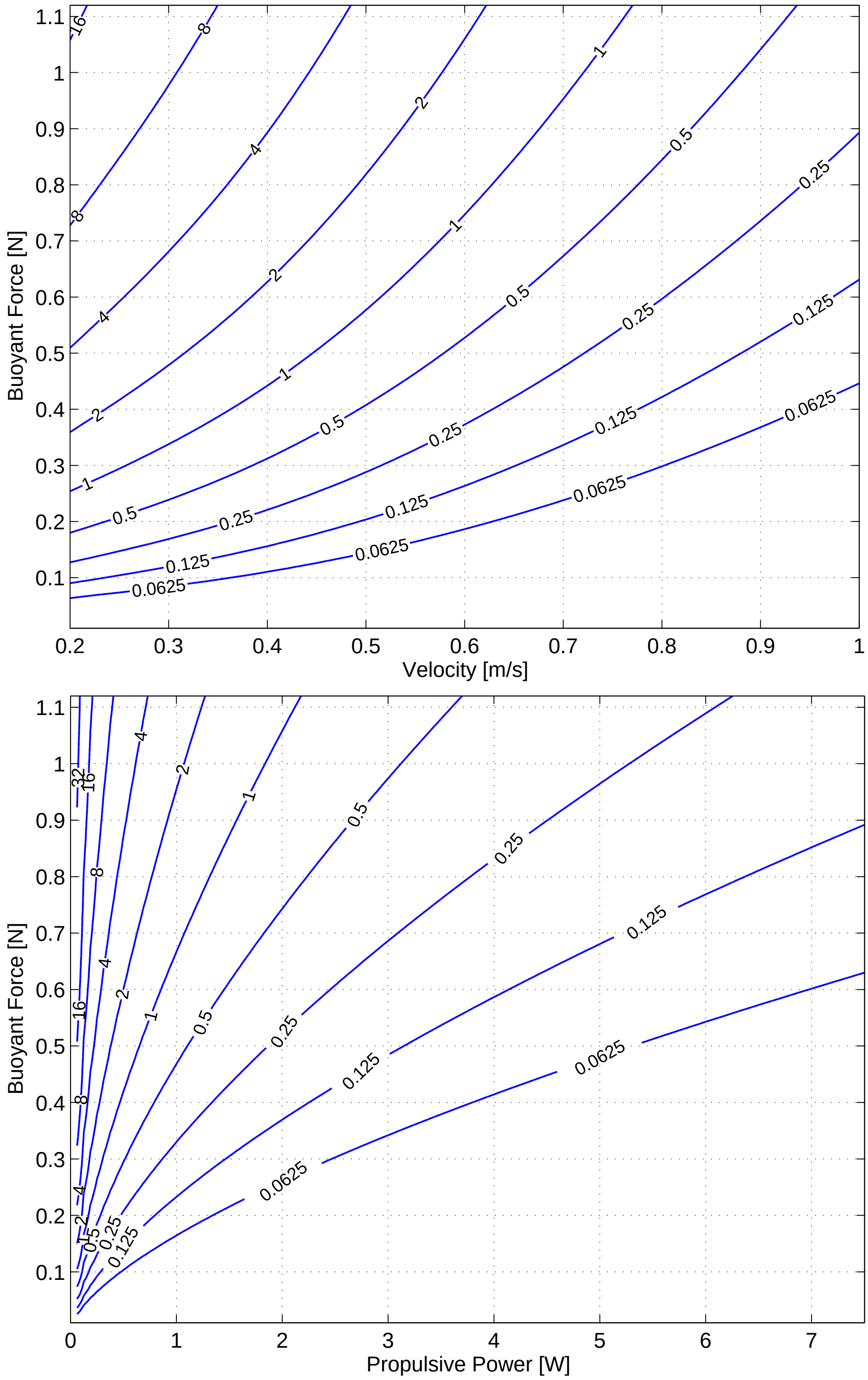

Figure 4.3: Percentage of range lost due to lift induced drag as a result of buoyant force where the propulsion control scheme operates on a constant velocity principle (top) or a constant propulsive power principle (bottom)

## 4.2 Linear Time Invariant Model

During steady state maneuvers the behavior of underwater gliders have been shown to fit linearized models reasonably well. While these models break down during dynamic events such as inflections or high levels of environmental disturbance, simulated tests have shown that they are well suited to designing multivariate control laws [163]. As such, the general linear time invariant discrete state space model is presented as

$$\mathbf{x}_{k+1} = \mathbf{A}\mathbf{x}_k + \mathbf{B}\mathbf{u}_k \tag{4.9}$$

$$\mathbf{y}_k = \mathbf{C}\mathbf{x}_k + \mathbf{D}\mathbf{u}_k \tag{4.10}$$

where $\mathbf{A}$ is the system matrix, $\mathbf{B}$ is the input matrix, $\mathbf{C}$ is the output matrix, $\mathbf{D}$ is the feed forward matrix, $\mathbf{x}$ is the state vector, $\mathbf{u}$ is the input vector, $\mathbf{y}$ is the output vector and $k$ is the time step.

To control the depth of an underwater glider the vehicle's depth and pitch are selected as state variables. The primary model inputs which influence these state variables are the underwater glider's ballast and mass shifting mechanism. The ballast mechanism for the underwater glider is located in the nose of the vehicle generating a pitching moment as well as a change in buoyancy. When the vehicle is under propulsion from the hybrid propulsion system the mass shifting mechanism, which is nominally used to control the vehicle pitch, also acts to control the vehicle's depth.

In order to identify model parameters an iterative prediction-error minimization method is used which minimizes a cost function through gradient descent methods [169, 170]. Two tests are performed to generate identification and verification data sets consisting of a hybrid glider operating under propulsion from the propeller and performing several dives and climbs such that both the mass shifting and ballast mechanisms are used. The profile depths were chosen to extend below the mixed layer depth of the top 20 to 30 meters as the water density varies most dramatically there. The resulting model parameters are given as

$$\mathbf{A} = \begin{bmatrix} 0.0216 & 0.0015 \\ -1.2624 & 0.9978 \end{bmatrix} \qquad \mathbf{B} = \begin{bmatrix} 0.00117 & -0.4433 \\ -0.00221 & -0.05372 \end{bmatrix} \tag{4.11}$$

$$\mathbf{C} = \begin{bmatrix} 1 & 0 \\ 0 & 1 \end{bmatrix} \qquad \mathbf{D} = \begin{bmatrix} 0 & 0 \\ 0 & 0 \end{bmatrix} \tag{4.12}$$

The time series of these tests are shown in Fig. 4.4 with a comparison to the identified state space model.

The model tracks the data in the verification set during steady state with some degradation during the more dynamic moments where the vehicle changes from diving to climbing and due to water density variations. The region of validity for the model is for absolute pitch values less than 0.5 radians and depths less than 50 meters where the thruster is at 75 percent power.

## 4.3 State Space Augmentation

The interdependence of the vehicle pitch and depth, with the model inputs suggests the use of a state feedback controller in which the control signals are given by the state feedback $\mathbf{u}_k$ as in

$$\mathbf{u}_k = -\mathbf{K}\mathbf{x}_k \tag{4.13}$$

where $\mathbf{K}$ is the state feedback gain matrix. However, in this arrangement the system controls the state variables to zero. To include a reference signal, an integral gain component is introduced into the state feedback controller by augmenting the state

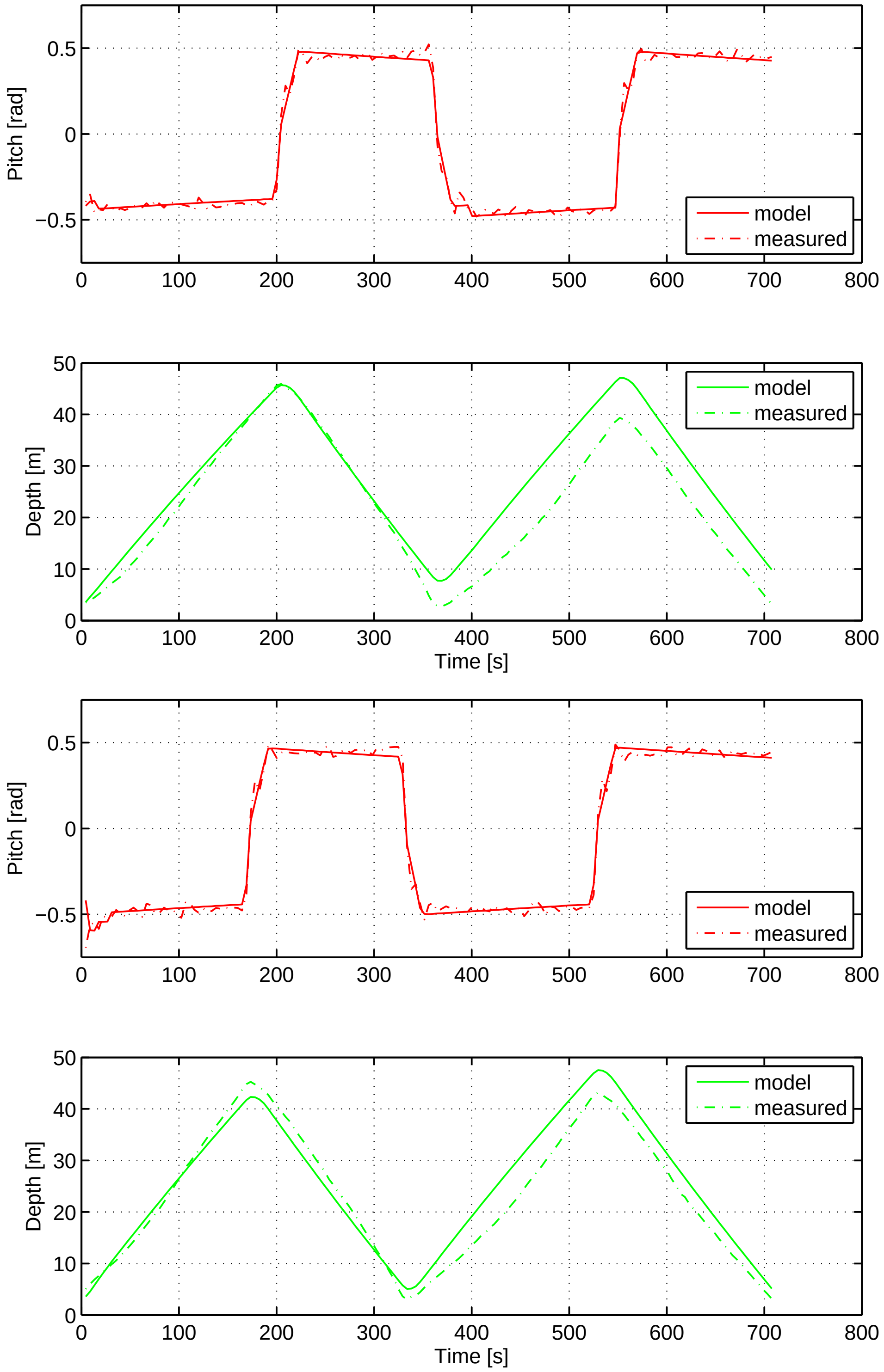

Figure 4.4: Time series of the identification data set (top) and the verification data set (bottom) showing the comparison between the measured values and the simulated values from the model. The measured values in this case are from field trials in September 2014 in Holyrood Arm, Newfoundland.

space equations with the state integral vector [171]. The state integral vector is initially defined by accumulating the error between a reference signal and the output according to

$$\mathbf{v}_k = \mathbf{v}_{k-1} + \mathbf{s}_k - \mathbf{y}_k \tag{4.14}$$

where $\mathbf{v}_k$ is the state integral vector, $\mathbf{s}_k$ is the control input and $\mathbf{y}_k$ is the output as before. Resulting in the new control signal equation

$$\mathbf{u}_k = -\mathbf{K}\mathbf{x}_k + \mathbf{K}_I\mathbf{v}_k \tag{4.15}$$

where $\mathbf{K}_I$ are the integral gains. To bring the state augmentation vector $\mathbf{v}_k$ into the state space formalism the time step is incremented as in

$$\mathbf{v}_{k+1} = \mathbf{v}_k + \mathbf{s}_{k+1} - \mathbf{y}_{k+1} \tag{4.16}$$

The output $\mathbf{y}_{k+1}$ is replaced by Eqn. 4.10 resulting in

$$\mathbf{v}_{k+1} = \mathbf{v}_k + \mathbf{s}_{k+1} - \mathbf{C}\mathbf{x}_{k+1} \tag{4.17}$$

where $\mathbf{D}$ is the null matrix as in Eqn. 4.12. Substituting Eqn. 4.9 for $\mathbf{x}_{k+1}$ results in

$$\mathbf{v}_{k+1} = \mathbf{v}_k + \mathbf{s}_{k+1} - \mathbf{C}[\mathbf{A}\mathbf{x}_k + \mathbf{B}\mathbf{u}_k] \tag{4.18}$$

which upon rearrangement becomes

$$\mathbf{v}_{k+1} = -\mathbf{C}\mathbf{A}\mathbf{x}_k + \mathbf{v}_k - \mathbf{C}\mathbf{B}\mathbf{u}_k + \mathbf{s}_{k+1} \tag{4.19}$$

The full augmented state space equations may be written through combining Eqn.

4.19 and Eqn. 4.9 as in

$$\begin{bmatrix} \mathbf{x}_{k+1} \\ \mathbf{v}_{k+1} \end{bmatrix} = \begin{bmatrix} \mathbf{A} & \mathbf{0} \\ -\mathbf{CA} & \mathbf{I} \end{bmatrix} \begin{bmatrix} \mathbf{x}_{k} \\ \mathbf{v}_{k} \end{bmatrix} + \begin{bmatrix} \mathbf{B} \\ -\mathbf{CB} \end{bmatrix} \mathbf{u}_k + \begin{bmatrix} \mathbf{0} \\ \mathbf{I} \end{bmatrix} \mathbf{s}_{k+1} \tag{4.20}$$

## 4.4 Linear Quadratic Regulator

The state feedback equation in Eqn. 4.15 contains 8 gain terms for a two state system. To tune these gains manually requires a significant number of trials. For an underwater glider these trials take around 30 to 60 minutes each and present a high level of risk to the platform in the case of gains with the wrong sign or order of magnitude. To minimize this risk and the amount of time needed for tuning the controller, a linear quadratic regulator (LQR) is proposed as a method of computing the energy optimal gains. A LQR computes energy optimal gains to regulate a system to zero by minimizing a quadratic cost function $\boldsymbol{\mathcal{J}}$ of the form [171, 172]

$$\boldsymbol{\mathcal{J}} = \frac{1}{\gamma} \sum_{k=0}^{\infty} [\bar{\mathbf{x}}' \boldsymbol{\mathcal{Q}} \bar{\mathbf{x}} + \bar{\mathbf{u}}' \boldsymbol{\mathcal{R}} \bar{\mathbf{u}}] \tag{4.21}$$

where $\boldsymbol{\mathcal{Q}}$ is the error weighted matrix and $\boldsymbol{\mathcal{R}}$ is the control weighted matrix.

By rewriting the system in Eqn. 4.20 to the state error equations, the LQR controller is able to regulate the state error and integral error to zero. The error equations are obtained by subtracting the final state values as in

$$\begin{bmatrix} \delta\mathbf{x}_{k} \\ \delta\mathbf{v}_{k} \end{bmatrix} = \begin{bmatrix} \mathbf{x}_{k} \\ \mathbf{v}_{k} \end{bmatrix} - \begin{bmatrix} \mathbf{x}_{\infty} \\ \mathbf{v}_{\infty} \end{bmatrix} \tag{4.22}$$

This change effectively removes the $\mathbf{s}_{k+1}$ term from the system as the control inputs are assumed to be constant resulting in Eqn. 4.20 being rewritten as the error augmented system shown in

$$\begin{bmatrix} \delta\mathbf{x}_{k+1} \\ \delta\mathbf{v}_{k+1} \end{bmatrix} = \begin{bmatrix} \mathbf{A} & \mathbf{0} \\ -\mathbf{CA} & \mathbf{I} \end{bmatrix} \begin{bmatrix} \delta\mathbf{x}_{k} \\ \delta\mathbf{v}_{k} \end{bmatrix} + \begin{bmatrix} \mathbf{B} \\ -\mathbf{CB} \end{bmatrix} \delta\mathbf{u}_k \tag{4.23}$$

and Eqn. 4.15 being rewritten as

$$\delta\mathbf{u}_k = -\mathbf{K}\delta\mathbf{x}_k + \mathbf{K}_I\delta\mathbf{v}_k \tag{4.24}$$

where $\delta\mathbf{x}$ and $\delta\mathbf{v}$ are the state error and state integral errors respectively. The introduction of the integral term requires additional consideration to limit overshoot due to integral windup. To accomplish this for the state-feedback system proposed in Eqn. 4.24 a limitation scheme is used based on the state outputs. In this scheme if the depth error exceeds a specified amount, in this case 2 meters was chosen, the integration terms are held constant. The premise behind this control law is to limit the integration to times when the vehicle is not actively diving or climbing to prevent overshoot from large changes in the depth command.

The system described in Eqns. 4.23 and 4.24 then permits the use of the theory developed for the computation of energy optimal gains based on the minimization of the function in Eqn. 4.21. To this end define

$$\bar{\mathbf{x}}(k+1) = \bar{\mathbf{A}}\bar{\mathbf{x}}(k) + \bar{\mathbf{B}}\bar{\mathbf{u}}(k) \tag{4.25}$$

where $\bar{\mathbf{x}}$, $\bar{\mathbf{u}}$, $\bar{\mathbf{A}}$ and $\bar{\mathbf{B}}$ are defined as

$$\bar{\mathbf{x}} = \begin{bmatrix} \delta\mathbf{x} \\ \delta\mathbf{v} \end{bmatrix} \tag{4.26}$$

$$\bar{\mathbf{u}} = -\bar{\mathbf{K}}\bar{\mathbf{x}} \tag{4.27}$$

$$\bar{\mathbf{A}} = \begin{bmatrix} \mathbf{A} & \mathbf{0} \\ -\mathbf{CA} & \mathbf{I} \end{bmatrix} \tag{4.28}$$

$$\bar{\mathbf{B}} = \begin{bmatrix} \mathbf{B} \\ -\mathbf{CB} \end{bmatrix} \tag{4.29}$$

The steady state Riccati equation which gives the solution to the minimum of the cost function is then

$$\bar{\boldsymbol{\mathcal{P}}} = \boldsymbol{\mathcal{Q}} + \bar{\mathbf{A}}'\bar{\boldsymbol{\mathcal{P}}}\bar{\mathbf{A}} - \bar{\mathbf{A}}'\bar{\boldsymbol{\mathcal{P}}}\bar{\mathbf{B}}(\boldsymbol{\mathcal{R}} + \bar{\mathbf{B}}'\bar{\boldsymbol{\mathcal{P}}}\bar{\mathbf{B}})^{-1}\bar{\mathbf{B}}'\bar{\boldsymbol{\mathcal{P}}}\bar{\mathbf{A}} \tag{4.30}$$

After iteratively solving for the solution to Eqn. 4.30 with the null matrix as the initial condition the optimal feedback gain matrix becomes

$$\bar{\mathbf{K}} = (\mathbf{R} + \bar{\mathbf{B}}'\bar{\boldsymbol{\mathcal{P}}}\bar{\mathbf{B}})^{-1}\bar{\mathbf{B}}'\bar{\boldsymbol{\mathcal{P}}}\bar{\mathbf{A}} = -\begin{bmatrix} \mathbf{K} & -\mathbf{K}_I \end{bmatrix} \tag{4.31}$$

In the presence of input constraints the optimality conditions for the functional in Eqn. 4.21 can change. Input constraints in the case of the underwater glider are present on the ballast and mass shifting mechanism due to their mechanical limits. To maintain optimality, the minimum energy control law is

$$\bar{\mathbf{u}}^* = -SAT\{\bar{\mathbf{K}}\bar{\mathbf{x}}\} \tag{4.32}$$

where the $SAT\{\}$ function denotes the saturation of the control signals at some limits while being able to take any value within those limits. This law has been shown to use the least energy for systems with input constraints, the difference being in rise/settling time due to the control signal saturating [172].

## 4.5 Simulated Response

The optimal gains for the controller may be computed according to Eqn. 4.31 by using the state parameters in Eqns. 4.11-4.12, rewriting them into the form of Eqns. 4.28-4.29 and iteratively solving the steady state Algebraic Riccati equation in Eqn. 4.30. The choice of error and control weighted matrices $\boldsymbol{\mathcal{Q}}$ and $\boldsymbol{\mathcal{R}}$ will impact the performance of the controller and should be selected to meet the design constraints. In this work the control weighted matrix is selected to penalize the control signals according to how much power they consume as in

$$\boldsymbol{\mathcal{R}} = \begin{bmatrix} 50 & 0 \\ 0 & 5 \end{bmatrix} \tag{4.33}$$

The power consumption of the ballast system is depth dependent, however, for simplicity the power is approximated to 50 W. In tuning the controller, the control weighted matrix is held constant and the error weighted matrix is adjusted. In the error weighted matrix the values along the main diagonal represent the weighting of the pitch, depth, integral pitch and integral depth error respectively in their real world units. By adjusting the relative weights of these values the desired performance may be achieved. In this work the values for the error weighted matrix were selected to give a high weighting to the pitch integral error and the depth integral error. The high integral pitch error weight is to minimize the angle of attack of the vehicle due to ballasting errors while the depth integral error weighting balances the integral pitch error weighting to still provide depth control with zero steady state error. On an infinite time horizon the values in $\boldsymbol{\mathcal{Q}}$ can be selected to be very small such that very little energy is expended and the response will have a very long settling time. Practically, the values in $\boldsymbol{\mathcal{Q}}$ must be higher to give a timely response. In this work it was attempted to choose values to give the fastest response with zero overshoot of the depth signal to a step input through repeated simulations using the identified system and are given by

$$\mathfrak{Q} = \begin{bmatrix} 100000 & 0 & 0 & 0 \\ 0 & 1 & 0 & 0 \\ 0 & 0 & 100 & 0 \\ 0 & 0 & 0 & 0.5 \end{bmatrix} \tag{4.34}$$

The gains are then computed to be

$$\bar{\mathbf{K}} = \begin{bmatrix} 1.8786 & -1.4815 & 1.3947 & 0.0154 \\ -0.2189 & 0.1308 & 0.0147 & -0.0047 \end{bmatrix} \tag{4.35}$$

Consideration is given to constant depth and constant altitude control. Constant depth control is typified by a step response and constant altitude control can be considered to be a tracking type problem. The simulated step response of the controller and its associated energy usage are shown in Fig. 4.5 where the energy consumed by the ballast and mass shifting systems is calculated according to

$$\mathbf{E}_{k+1} = \mathbf{E}_k + \Delta\mathbf{T}\mathbf{P}_u \tag{4.36}$$

where $\mathbf{E}_k$ is the energy matrix, $\Delta\mathbf{T}$ is the time difference matrix and $\mathbf{P}_u$ is the input power matrix.

The step response of the controller shows that the depth response is timely and exhibits no overshoot as desired. Additionally, the ballast is integrated to a non-zero value of around -20 cc to compensate for the mis-ballasted vehicle, causing the steady state pitch error to be zero. The energy consumed for this maneuver is reasonably well

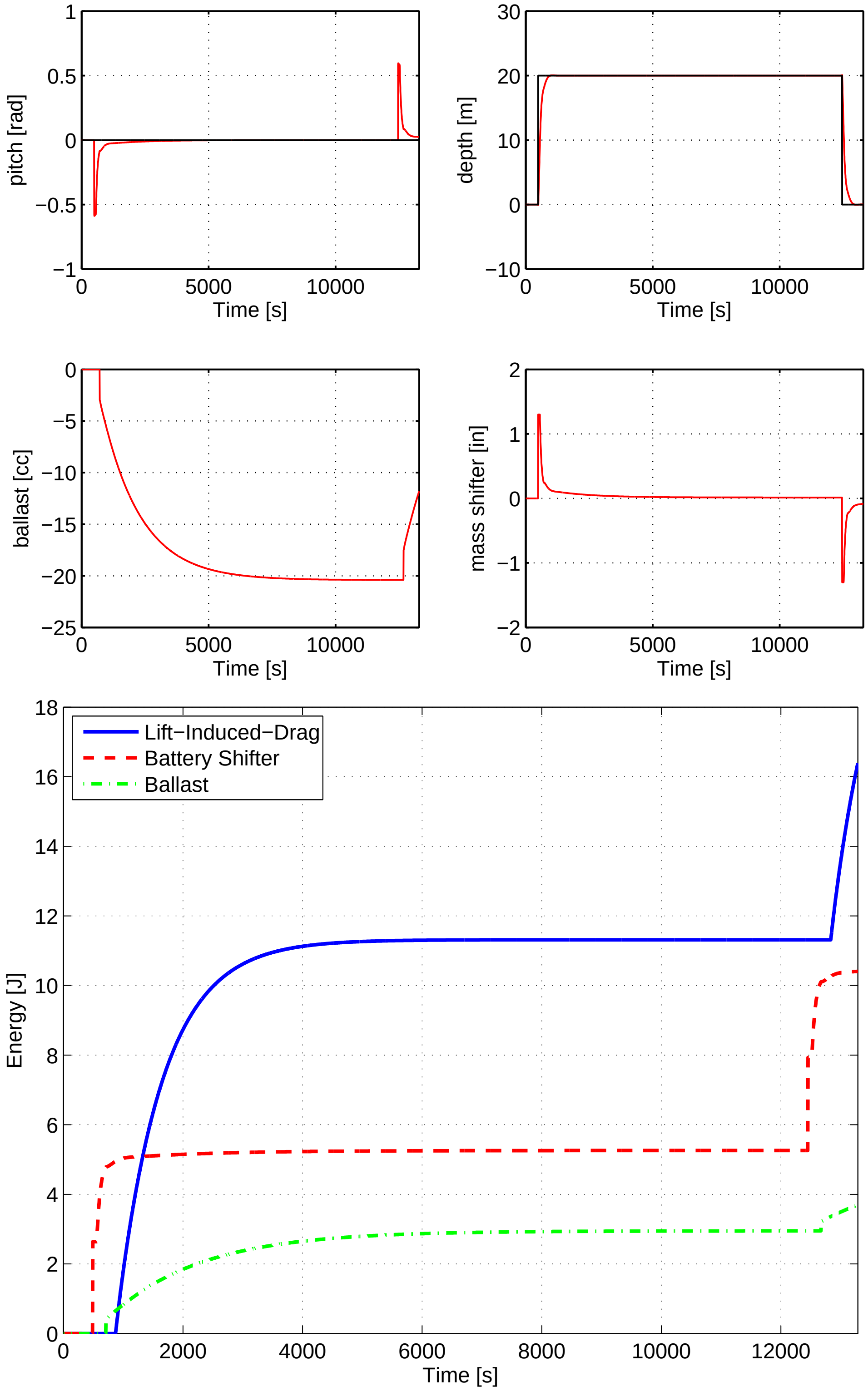

Figure 4.5: Pitch (top left) and depth (top right) simulated response to a 20 meter step input for the proposed controller and gains with the ballast (middle left) and mass shifting (middle right) commands where the black line is the commanded value and the red is the simulated value. The energy consumed by the ballast and mass shifting mechanism as well as the hydrodynamic energy lost to the lift induced drag (bottom)

balanced between the ballast and mass shifting mechanisms and the hydrodynamic energy lost to the lift induced drag is low and not increasing during the steady state portion of the response.

For the tracking problem a sinusoid is used to emulate a slowly undulating seafloor. The simulated tracking response and its associated energy usage are shown in Fig. 4.6. The tracking response of the controller shows the same timely response to the step input as well as decent tracking ability while also maintaining a low level of energy expenditure. In particular the tracking error is less than 0.5 meters and the total energy consumed over the course of the several hour simulation is around 50 Joules. This overall energy expenditure remains low in comparison to the energy spent by the base power of one Watt and propulsion system power of one Watt resulting in around 26000 Joules of energy expended over the same 3.7 hour period.

## 4.6 Experimental Response

The energy optimal depth controller was verified through further field trials taking place in Holyrood Arm, Newfoundland during September 2014. These trials used the state feedback controller presented in Section 4.4 with the energy optimal gains from Eqn. 4.35.

The vehicle control software was modified to include the state feedback controller. This modification was accomplished by adding an additional control state to the existing depth controller. The state-feedback code was then able to be called by simply running a controlled depth mission with the control state set to this experimental mode. The hybrid underwater glider has difficulty diving from the surface when using only the propeller and mass shifting mechanism to control the pitch. For this reason the vehicle was commanded to dive using a ballast command. Once the vehicle

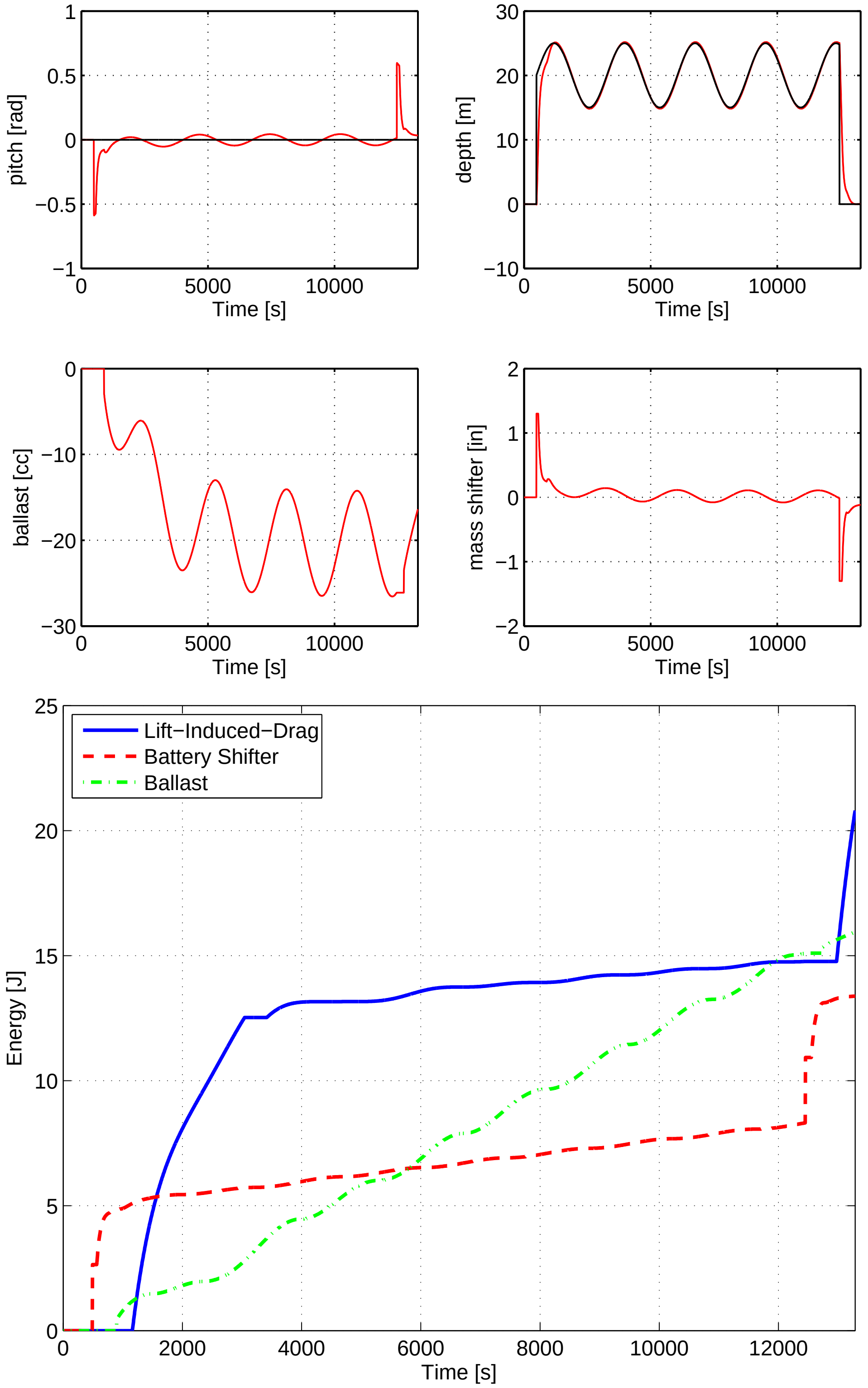

Figure 4.6: Pitch (top left) and depth (top right) simulated response to a 5 meter amplitude sinusoid at 20m depth for the proposed controller with the ballast (middle left) and mass shifting (middle right) commands where the black line is the commanded value and the red is the simulated value. The energy consumed by the ballast and mass shifting mechanism as well as the hydrodynamic energy lost to the lift induced drag (bottom)

reached a depth of 10 meters, such that it was certain to be underwater, the ballast was set to the neutral position and the thruster enabled to 75 percent. The experimental response for the energy optimal depth controller is shown in Fig. 4.7.

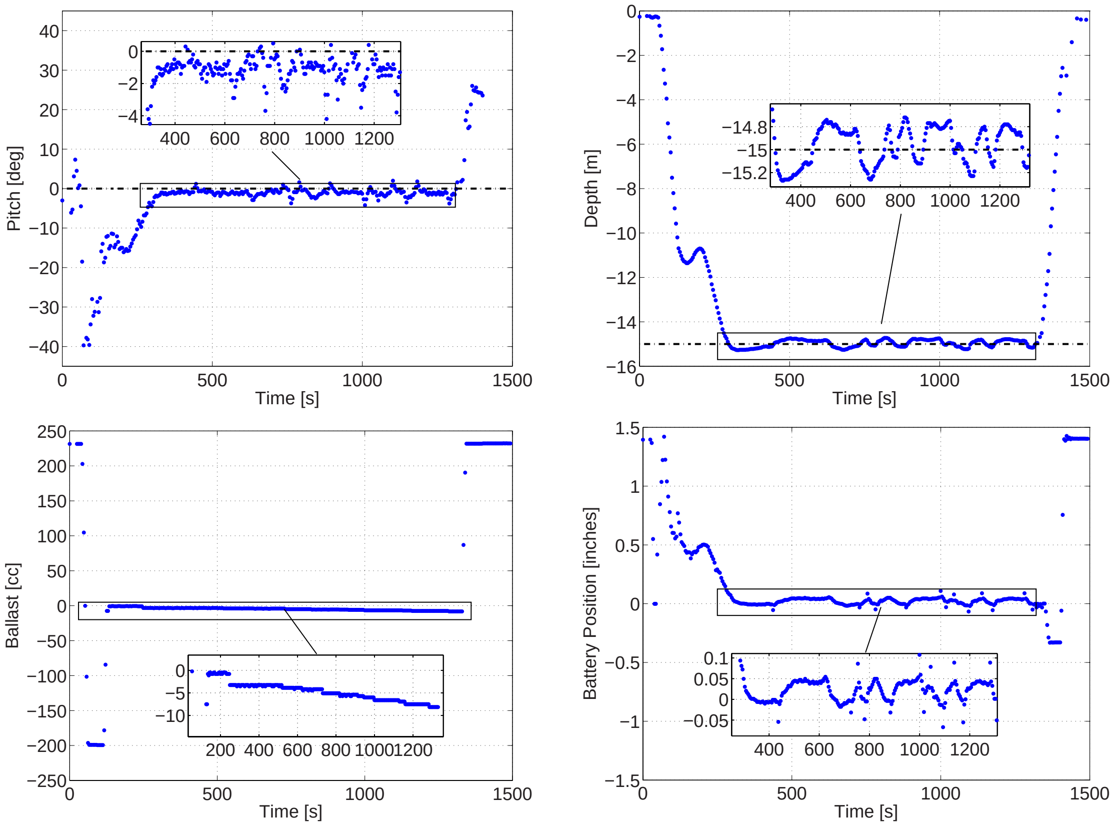

Figure 4.7: Pitch (top left), depth (top right), ballast (bottom left) and battery position (bottom right) for the energy optimal depth control trials performed in September 2014 in Holyrood Arm, Newfoundland.

Several observations are of note through examination of the response of the vehicle during these trials. First and foremost the vehicle's depth is controlled to the commanded 15 meter depth with a peak to peak error once converged of less than 0.5 meters. Second, the vehicle's pitch has a slight negative bias of around -1.0 degrees suggesting the vehicle is slightly too buoyant. This negative pitch corresponds to the response of the ballast system which is slowly integrating in a negative fashion.

Third, the vehicle's mass shifting mechanism tends to overcompensate for the depth error due to the dead-band present in its control loop. This dead-band is present to prevent the constant response of the actuator to noise in the position feedback. The amplitude of the response of the vehicle to the movement of the mass shifting mechanism is dependent on the vehicle's H-moment, or the separation of its center of buoyancy and gravity. By increasing the vehicle's H-moment, the amplitude of the response would decrease, subsequently decreasing the effect of the dead-band on the position sensor's feedback.

The energy consumed by the vehicle's actuators and lost to the lift induced drag is shown in Fig. 4.8.

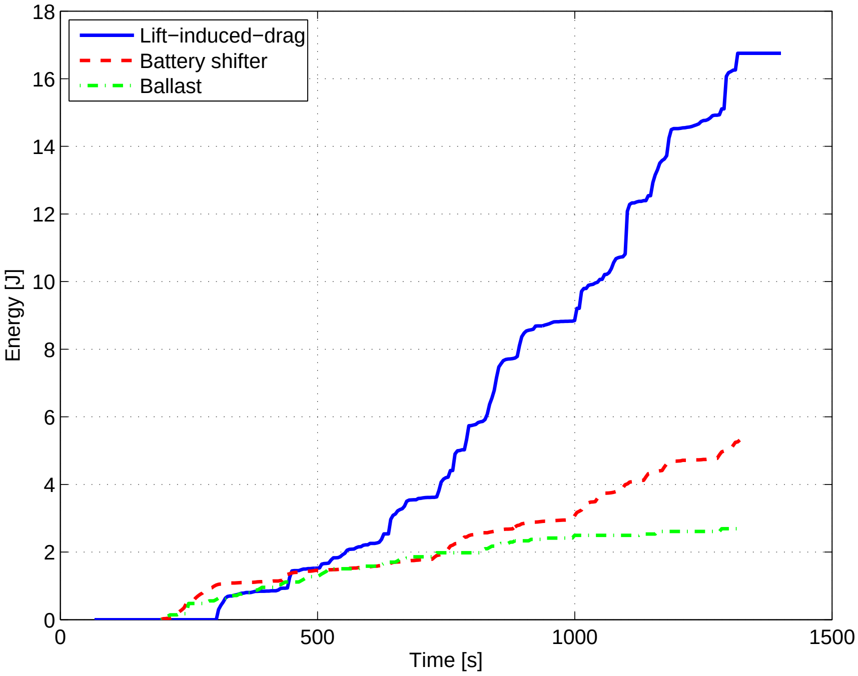

Figure 4.8: Energy consumed during the energy optimal depth control trials

The energy consumed during the field trials shows similarities to the simulations in the overall magnitude of the energy consumed. The ballast system and mass shifting mechanism both show a response on the order of several Joules. The energy lost to the lift induced drag does not level out during the field trials due to the trial length being limited to 30 minutes. However, it shows a response on the order of 10's of Joules which is in agreement with the simulations. The largest discrepancy is due to the mass shifting mechanism's continued use which represents a constant load. However, at only 5 Joules over a 30 minute run this energy consumption is minimal compared to the total vehicle energy consumption of nearly 2500 Joules. The energy lost to the lift induced drag of around 17 Joules represents 0.68 percent of the total energy consumed during the test mission. This loss is consistent with compensating for a net buoyant force of around 0.75 N and an advance velocity of 0.5 m/s from Fig. 4.3. However, if the measured pitch of 1.0 degree from the steady state portion of the mission is taken as the angle of attack, the net buoyant force from Fig. 4.1 is considerably higher. These discrepancies are possibly due to the misalignment of the pitch sensor and vehicle frames of reference or overestimation of the lift force at small angles of attack from the Graver hydrodynamic model [163]. To mitigate the case of a sensor and vehicle frame misalignment it is suggested to add a small dead-band of around 0.25 degrees to the pitch integrator. This dead-band is motivated by the relatively small penalty to the range from the lift induced drag at such an angle.

# Chapter 5

# Glider Terrain Aided Navigation

The general terrain aided navigation (TAN) problem attempts to localize a body using a-priori digital parameter models (DPMs), some knowledge of the body's movements and measurements which relate the body to the DPM. One set of solutions to these types of problems are broadly based on sequential importance sampling methods, also known as particle filters. These filters are broadly applicable to non-linear estimation problems and have a robust collection of literature explaining their derivations and use including; a visual explanation of the particle filter [173]; theoretical treatments [174, 175, 176]; as well as some history of the particle filter and its context with regards to other estimation techniques. [177]

The generic particle filter algorithm uses many guesses, or particles of where the most recent parameter measurement might be and compares that measurement to the DPM for each particle location. These particles are propagated according to an importance density function which attempts to allocate particles to the relevant part of the state space based on all of the prior states and all of the prior measurements. The selection of an importance density function is a significant consideration in the design of a particle filter with respect to a specific application. Each particle's location has an associated value from the DPM which is compared to the water depth measurement to evaluate its weight. These weights are normalized such that the sum of the weights is equal to one, shaping them into a probability distribution. The state estimate is then given by the sum of the product of each particle's location with the particle's weight, essentially computing the centroid of the particle cloud.

The classic particle filter algorithm presents several difficulties with its implementation. The first is related to the choice of the importance density function which for the original formulation requires complete knowledge of the entire set of states and measurements. While it has been shown that an optimal form of the importance density function can be approximated, it is only usable if analytic forms of the state transition probabilities are available such that the integrals have closed form solutions [175]. This difficulty has led to sub-optimal forms to be used such as the transitional prior, which simply applies the state update to the prior particle locations.

However, in using the transitional prior, as the prior densities accumulate, the weights of the particles become concentrated on very few particles, with the majority of particles having little weight and therefore contributing very little to the state estimate. This concentration of particle weights is termed sample impoverishment or degeneracy [178]. To help improve this situation the particles are often re-sampled such that those particles with very little weight are discarded and the particles with a lot of weight are divided into more. This process leads to another problem in which the particle cloud becomes very small and no longer provides any corrective behavior, termed particle collapse. One method used to deal with particle collapse is through the jittering or roughening of the particles in which their locations have some noise added to spread them back out in the state space [178].

The resulting methodology which includes these simplifications and improvements is termed the sequential importance re-sampling method. In this method re-sampling is only performed when needed as determined by some metric. When re-sampling is performed at every time step the method is termed the bootstrap method [178]. In the bootstrap method the evaluation of the weights is simplified as they will have equal value after re-sampling, however, the frequent re-sampling also accentuates the particle collapse requiring stronger jittering. The addition of jittering to the algorithm essentially introduces additional process noise into the estimator. This increased process noise has been shown to improve the robustness of the estimator to complete divergence, allowing reconvergence after periods of sparse measurements, flat terrain or DPM artifacts [179, 180]. The improved robustness comes at the cost of higher estimator noise which reduces the performance of a survey grade AUV but still provides an improvement over the dead reckoning solution in an underwater glider.

The jittered bootstrap method is used in the remainder of this work and is presented in Algorithm 1 and illustrated in Fig. 5.1.

**Algorithm 1** Jittered Bootstrap

```
[$\hat{\mathbf{x}}_k$,$\{\mathbf{x}_k^i\}_{i=1}^N$]=BOOTSTRAP [$\{\mathbf{x}_{k-1}^i\}_{i=1}^N$,$\Delta\mathbf{x}_k$,$\mathbf{z}_k$]
for $i = 1$ to $N$ do
    compute jitter: $\mathbf{r}_k = \mathbf{N}(0, \sigma_j^2)$
    state update: $\mathbf{x}_k^i = \mathbf{x}_{k-1}^i + \Delta\mathbf{x}_k + \mathbf{r}_k$
    compute weights: $\tilde{w}_k^i = p(\mathbf{z}_k|\mathbf{x}_k^i)$
end for
calculate total weight: $s_w = \sum_{i=1}^{N} \tilde{w}_k^i$
for $i = 1$ to $N$ do
    normalize weights: $w_k^i = \frac{\tilde{w}_k^i}{s_w}$
end for
re-sample: [$\{\mathbf{x}_k^i\}_{i=1}^N$]=RESAMPLE[$\{\mathbf{x}_k^i, w_k^i\}_{i=1}^N$]
estimate state: $\hat{\mathbf{x}}_k = \frac{1}{N} \sum_{i=1}^{N} \mathbf{x}_k^i$
```

The jittered bootstrap algorithm takes as inputs the prior particles $\{\mathbf{x}_{k-1}^i\}_{i=1}^N$, the state update $\Delta\mathbf{x}_k$ and the water depth estimate $\mathbf{z}_k$ at time step $k$ where $N$ is the number of particles and $i$ is the particle index. The outputs of the method are the

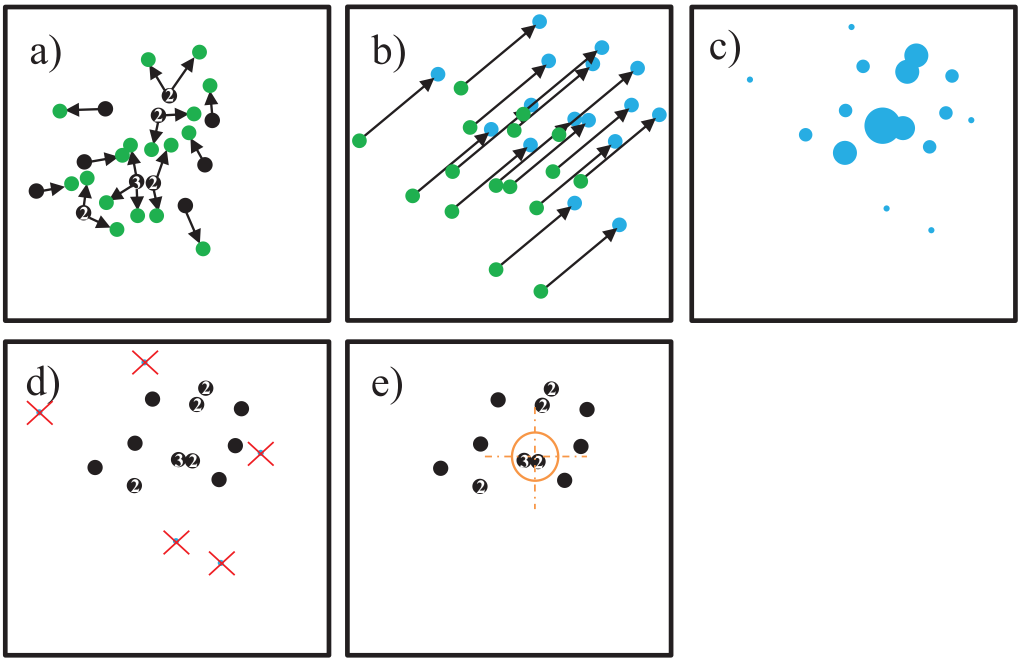

Figure 5.1: An illustration of the jittered bootstrap algorithm with two state variables for a small number of particles where a) shows the jittering of the particles, b) shows the particles before and after the state update, as indicated by the arrows, is applied, c) shows the particle weights where larger particles indicate a higher weight based on how closely the water depth measurement matches the DPM, d) shows the resampling process where small particles are discarded as indicated by the crosses and large particles divided and e) shows the state estimation as indicated by the cross hair. Particles with numbers overlaid represent a stack of particles.

state estimate $\hat{\mathbf{x}}_k$ and the particle locations $\{\mathbf{x}_k^i\}_{i=1}^N$ which are then saved for the next iteration. The operation of the algorithm begins with computing a particle jitter $\mathbf{r}_k$ based on a normal distribution with zero mean and $\sigma_j^2$ variance. The particle for time step $k$ is then drawn by updating the prior particle location $\mathbf{x}_{k-1}^i$ with the state update $\Delta\mathbf{x}_k$ and applying the particle jitter computed previously. The weight of each particle $\tilde{w}_k^i$ is then evaluated as the probability of the water depth estimate given the particle's location. This process is repeated $N$ times, drawing all of the particles and computing their weights. These weights are then normalized by the sum of the weights $s_w$. The particles are then re-sampled and the state estimate $\hat{\mathbf{x}}_k$ is computed through the sum of the particles divided by the total number of particles.

The re-sampling algorithm selected for this work is the systematic re-sampling method as outlined in Algorithm 2 [181]. The systematic re-sampling method provides a fast and simple way to represent the probability density through evenly weighted particles, requiring the particle locations and weights as inputs and providing the re-sampled particles as outputs. The algorithm operates by first taking the cumulative sum, $\{cs_k\}_{i=1}^N$, of the particle weights, forming an increasing set of values from zero to one. A random number $n$ is then drawn from a uniform distribution on the interval [0,1] and the index $s_k^i$ of the cumulative sum found to which the random number is equal to the cumulative sum. The particle at that index is then stored for output. In this way particles with high weight are divided into many particles as they occupy a large portion of the cumulative sum and particles with small weights are discarded as they occupy a negligible portion of the cumulative sum.

**Algorithm 2** Systematic Re-Sampling

```
$[\{\mathbf{h}_k^i\}_{i=1}^N]$=RESAMPLE$[\{\mathbf{x}_k^i, w_k^i\}_{i=1}^N]$
cumulative sum: $\{cs_k\}_{i=1}^N$ = CUSUM($\{w_k^i\}_{i=1}^N$)
for $i = 0$ to $N$ do
    draw random number on [0 1]: $n$ =RAND(0,1)
    find where it belongs: $s_k^i$ =FIND($n$,$\{cs_k\}_{i=1}^N$)
    store particle: $\mathbf{h}_k^i$ =$\{\mathbf{x}_k^i\}_{i=1}^N(s_k^i)$
end for
```

## 5.1 Digital Parameter Model

The DPM used in this work is constructed from ship based multi-beam surveys done by Memorial University's Marine Institute. The DPM is gridded by latitude and longitude at an equivalent distance of roughly 2 meters. Since the DPM is generated from data collected by a ship an error model dependent on the DPM water depth similar to the method in the International Hydrographic Organization's Standards for Hydrographic Surveys is used [182, 183]. This error model has a variance of $\sigma^2_{DPM}$ as in

$$\sigma^2_{DPM} = \frac{1}{2}\sqrt{1 + (0.023 z_{DPM})^2} \tag{5.1}$$

where $z_{DPM}$ is the water depth of a particular location of the DPM. The value of the DPM at each particle's location is then obtained through bilinear interpolation. Any depth bias present in the DPM is accounted for in the water depth estimate as $z_b$. A depth bias may result from a combination of a misregistration of the multi-beam data during processing, errors in sound velocity profile estimates or errors in the tidal estimates.

Two flags are inserted into the DPM, one at the shoreline and one at the DPM boundary to allow for decisions to be made when a particle's water depth estimate from the DPM returns one of these flags. The shoreline flag prevents values for the DPM being returned where there is no water but does not transition the algorithm to a dead-reckoned solution. The DPM boundary flag allows the algorithm to check if there is a new DPM to load and if not, reverts to the dead-reckoned navigation solution.

## 5.2 Water Depth Measurement Model

The water depth estimate from the glider combines the depth of the vehicle given by the pressure sensor with the altitude of the vehicle given by the altimeter. The altimeter is a 170 kHz, narrow beam sonar (3 degrees), located in the nose of the vehicle and angled at 26 degrees forward of the vertical such that at the nominal dive angle of 26 degrees the altimeter points straight down. The 300 psi pressure transducer for the vehicle is ported in the rear bulkhead and connected to the sensor located in the aft of the glider. The locations and orientations of these devices relative to the center of buoyancy are illustrated in Fig. 5.2.

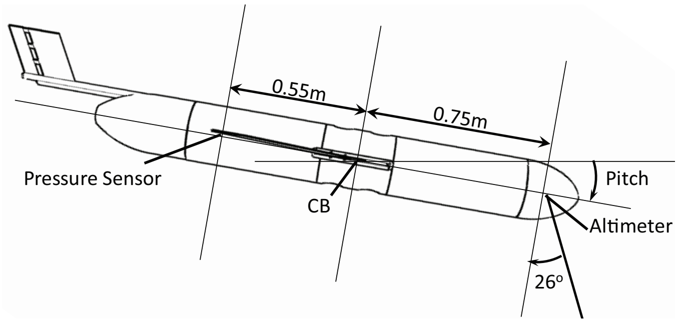

Figure 5.2: Locations of the altimeter and pressure transducer relative to each other and the center of buoyancy where CB is the center of buoyancy

Since the altimeter and pressure transducer are not co-located their vertical separation must be accounted for in the water depth estimate. Additionally, as the density of water changes, the speed and direction of the sound through the water changes as well. To correct for this a simple ray tracing procedure, shown in Algorithm 3, is performed which uses Snell's law to compute the path based on the sound speed profile obtained from the glider's conductivity, temperature and depth (CTD) sensor and the initial beam angle [184].

The glider altimeter assumes a uniform sound speed of 1500 m/s and reports an altitude, $z_{a,k}$. The ray tracing is performed by backing the travel time out of this initial estimate, using the glider roll $\phi_{g,k}$ and pitch $\theta_{g,k}$ to compute the beam angle from vertical $\theta_v$ and using the glider depth $z_{g,k}$ as the starting depth. Initial estimates of the speed of sound $c$ are computed through linear interpolation which is used to compute the ray tracing constant $a$. The algorithm then iterates the water depth estimate by $\Delta z$ until the one way travel time is exceeded, keeping track of

**Algorithm 3** Glider Altitude Ray Tracing

```
$[\hat{z}_{rt,k}, \Delta\mathbf{x}_{rt,k}]$=RAYTRACE $[z_{g,k}, z_{a,k}, \phi_{g,k}, \theta_{g,k}, \psi_{g,k}, SV(z)]$
initialize $\hat{z}_{rt,k}$ to $z_{g,k}$
initialize $x$ and $t$ to zero
set increment: $\Delta z = 0.1$
compute beam angle from vertical: $\theta_v = \arccos(\cos\phi_{g,k}\cos(\theta_{g,k} - 26^o))$
compute one way travel time: $t_{1way} = \frac{z_{a,k}}{1500}$
compute c: $c =$LINEARINT$[SV(z), \hat{z}_{rt,k}]$
compute a: $a = \sin\frac{\theta_v}{c}$
while $t < t_{1way}$ do
    increment water depth estimate: $\hat{z}_{rt,k} += \Delta z$
    update x: $x += \Delta z \tan(\theta_v)$
    update t: $t += \frac{\sqrt{(\Delta z \tan(\theta_v))^2 + \Delta z^2}}{c}$
    update c: $c =$LINEARINT$[SV(z), \hat{z}_{rt,k}]$
    update angle: $\theta_v = \arcsin(ac)$
end while
compute beam heading: $\psi_{b,k} = \arctan(\frac{\sqrt{2z^2_{rt,k}(1-\cos\phi_{g,k})}}{(\hat{z}_{rt,k} - z_{g,k})\tan(\theta_{g,k} - 26^o)})$
compute x offset: $\Delta x_{rt,k} = -x\sin(\psi_{g,k} + \psi_{b,k})$,
compute y offset: $\Delta y_{rt,k} = -x\cos(\psi_{g,k} + \psi_{b,k})$
```

the horizontal distance $x$ the beam travels. The results of this calculation are the ray traced water depth, $\hat{z}_{rt,k}$ and the measurement location offsets, $\Delta\mathbf{x}_{rt,k}$, which are computed using the horizontal beam distance and the combined beam and vehicle headings $\psi_{b,k}$ and $\psi_{g,k}$.

The tidal variation may also be included in the water depth model to account for the time varying signal of the water depth. The tidal correction, $z_{T,k}$, may be either historical measurements or from a predictive model. In this work the historical measurements from the St. John's, Newfoundland station in the Canadian Tides and Water Levels Data Archive were used [185].

The resulting water depth measurement model is given as

$$z_{w,k} = \hat{z}_{rt,k} + x_{ap} sin(\theta_{g,k}) + z_{T,k} + z_b \tag{5.2}$$

where $\hat{z}_{rt,k}$, $\theta_{g,k}$ and $z_{T,k}$ are the ray traced altitude, vehicle pitch and tidal signal at time step $k$. The distance from the pressure sensor to the altimeter along the vehicle axis is $x_{ap}$ and the DPM depth bias is $z_b$ which is defined in Section 5.1.

## 5.3 Glider Terrain Aided Navigation

An unmodified Slocum Electric underwater glider has rudimentary versions of all of the components necessary for an implementation of the jittered bootstrap method shown in Algorithm 1. It computes a dead-reckoned navigation solution which may be used for the state update as in Eqn. 3.4 and has an altimeter and pressure sensor which combined allow for a water depth estimate as in Eqn. 5.2. The only other inputs to the bootstrap algorithm are the prior particles, which once initialized are propagated from time step to time step and the DPM. After initialization, the algorithm computes a location estimate for every new altimeter reading. In this way each altimeter reading increments the glider TAN time step. The complete glider TAN method is shown in Algorithm 4 as an extension of the bootstrap method shown in Algorithm 1 with the initialization procedure as follows:

1. get initial Lat/Lon: $\hat{Lat}_{k-1}$,$\hat{Lon}_{k-1} = Lat_{GPS}$,$Lon_{GPS}$
2. set Local Mission Coordinate frame: $\hat{\mathbf{x}}_{k-1}$ ={0,0}
3. set prior particles: $\{\mathbf{x}^i_{k-1}\}^N_{i=1} = \mathbf{0}$
4. wait for first altimeter reading

The initialization procedure requires an initial location, which, on an underwater glider, is obtained by the GPS while the vehicle is at the surface before the mission begins. This initial location sets the origin for the Local Mission Coordinate (LMC) reference frame in units of meters. The prior particles are initialized to zero, relying on the jittering of the particles to spread the particles by the appropriate amount. The glider TAN algorithm is now ready to run every time there is a new altimeter reading.

The glider TAN algorithm's inputs are the prior particles $\{\mathbf{x}_{k-1}^i\}_{i=1}^N$, the prior state estimate $\hat{\mathbf{x}}_{k-1}$ in LMC and in latitude $\hat{Lat}_{k-1}$ and longitude $\hat{Lon}_{k-1}$, the state update $\Delta\mathbf{x}_k$ from the glider, the glider depth $z_{g,k}$ and the glider altitude $z_{a,k}$. Other inputs include $\phi_{g,k}$, $\theta_{g,k}$ and $\psi_{g,k}$ which are the glider's roll, pitch and heading, the sound velocity profile $SV(z)$ and the DPM.

The outputs of the algorithm are the glider TAN state estimate $\hat{\mathbf{x}}_k$ in LMC, and in latitude $\hat{Lat}_k$ and longitude $\hat{Lon}_k$ and the particles $\{\mathbf{x}_k^i\}_{i=1}^N$.

The algorithm begins by ray tracing the altitude to obtain the ray traced water depth $\hat{z}_{rt,k}$ and the water depth measurement offsets $\Delta\mathbf{x}_{rt,k}$ using Algorithm 3. The water depth estimate $z_{w,k}$ is then computed according to Eqn. 5.2 by adding the pressure sensor and altimeter vertical separation, the tidal signal and the DPM depth bias to the ray traced water depth. For the offline trials the DPM depth bias was computed by taking the average water depth estimate error over the entire set of measurements. During the online trials an estimate of the DPM depth bias was formed from values measured during a set of initialization profiles.

The algorithm next enters the particle update and weight computation loop which first checks the dead-reckoning flag. If the vehicle is not dead-reckoning the algorithm proceeds to compute the particle jitter $\mathbf{r}_k$ which are randomly generated using a normally distributed pseudo-random number generator based on the Mersenne Twister with variance $\sigma_j^2$ and zero mean [186]. The particle's location is then computed in LMC through adding the state update $\Delta\mathbf{x}_k$, the particle jitter and the water depth measurement offsets to the prior particle's locations. To interface with the DPM the

**Algorithm 4** Glider TAN

```
$[\hat{\mathbf{x}}_k,\{\mathbf{x}_k^i\}_{i=1}^N,\hat{Lat}_k,\hat{Lon}_k]$
$=$gTAN $[\{\mathbf{x}_{k-1}^i\}_{i=1}^N,\hat{\mathbf{x}}_{k-1},\hat{Lat}_{k-1},\hat{Lon}_{k-1},\Delta\mathbf{x}_k,z_{g,k},z_{a,k},\phi_{g,k},\theta_{g,k},\psi_g,SV(z),DPM]$
Ray trace altitude: $[\hat{z}_{rt,k},\Delta\mathbf{x}_{rt,k}]$=RAYTRACE $[z_{g,k},z_{a,k},\phi_{g,k},\theta_{g,k},\psi_{g,k},SV(z)]$
Compute water depth estimate: $z_{w,k} = \hat{z}_{rt,k} + x_{ap}sin(\theta_{g,k}) + z_{T,k} + z_b$
for $i = 0$ to $N$ do
    if Not Dead-Reckoning then
        Compute jitter: $\mathbf{r}_k = \mathbf{N}(0,\sigma_j^2)$
        Compute particle location in LMC: $\mathbf{x}_k^i = \mathbf{x}_{k-1}^i + \Delta\mathbf{x}_k + \mathbf{r}_k + \Delta\mathbf{x}_{rt,k}$
        Convert LMC to Lat/Lon: $[Lat_k^i,Lon_k^i]$=LMC2LL$[\mathbf{x}_k^i,\hat{\mathbf{x}}_{k-1},\hat{Lat}_{k-1},\hat{Lon}_{k-1}]$
        if $Lat_k^i,Lon_k^i$ within DPM bounds then
            get DPM water depth: $z_{DPM,k}$=BILINEAR$[Lat_k^i,Lon_k^i,DPM]$
            if Shoreline Flag then
                Set DPM water depth to zero: $z_{DPM,k}$=0
            end if
            if Map Bounds Flag then
                Check for new DPM
                Set Dead-Reckon Flag
            end if
            compute DPM variance: $\sigma_{DPM}^2 = 1/2\sqrt{1 + (0.023z_{DPM,k})^2}$
            compute weight: $\tilde{w}_k^i$ = NORMPDF$[z_{w,k},z_{DPM,k},\sigma_{DPM}^2]$
        else
            Set Dead-Reckon Flag
        end if
    end if
end for
if Not Dead-Reckoning then
    compute particle weight sum: $s_w = \sum_{i=1}^{N} \tilde{w}_k^i$
    for $i = 1$ to $N$ do
        normalize weights: $w_k^i = \frac{\tilde{w}_k^i}{s_w}$
    end for
    re-sample: $\{\mathbf{x}_k^i\}_{i=1}^N$=RESAMPLE$[\{\mathbf{x}_k^i,w_k^i\}_{i=1}^N]$
    compute state estimate in LMC: $\hat{\mathbf{x}}_k = \frac{1}{N}\sum_{i=1}^{N} \mathbf{x}_k^i$
    convert LMC to Lat/Lon: $[\hat{Lat}_k,\hat{Lon}_k]$=LMC2LL$[\hat{\mathbf{x}}_k,\hat{\mathbf{x}}_{k-1},\hat{Lat}_{k-1},\hat{Lon}_{k-1}]$
else
    compute state estimate in LMC: $\hat{\mathbf{x}}_k = \hat{\mathbf{x}}_{k-1} + \Delta\mathbf{x}_k$
    convert LMC to Lat/Lon: $[\hat{Lat}_k,\hat{Lon}_k]$=LMC2LL$[\hat{\mathbf{x}}_k,\hat{\mathbf{x}}_{k-1},\hat{Lat}_{k-1},\hat{Lon}_{k-1}]$
    Reset particles: $\{\mathbf{x}_k^i\}_{i=1}^N = \hat{\mathbf{x}}_k$
    Reset Dead-Reckon Flag
end if
```

LMC location is converted to latitude and longitude by assuming the change in LMC location, indicated by $\Delta x$ and $\Delta y$, is approximated by the length of an arc as in

$$Lat_k = Lat_{k-1} + (\Delta y)/r_e \tag{5.3}$$

$$Lon_k = Lon_{k-1} + (\Delta x)/(r_e cos(Lat_{k-1})) \tag{5.4}$$

where $r_e$ is the radius of the earth.

Once the particle's latitude and longitude are computed, the particle's location may be checked against the general DPM bounds. If it is within the bounds, the DPM water depth $z_{DPM,k}$ is retrieved through bilinear interpolation, otherwise, the dead-reckoning flag is set. If the DPM water depth is equal to the shoreline flag then it is zeroed. If it is equal to the map bounds flag then the dead-reckoning flag is set. Otherwise the DPM variance $\sigma^2_{DPM}$ is computed as in Eqn. 5.1. The particle weight is then computed by comparing the water depth estimate to the DPM water depth through a normal probability density function with the DPM variance. This procedure is repeated for all $N$ particles.

The algorithm now moves on to check once more if the dead-reckoning flag is not set before computing the particle weight sum $s_w$ and using it to normalize the weights. The particles are next re-sampled using the systematic re-sampling method described in Algorithm 2. After the re-sampling process all of the particles have equal weight allowing the state estimate to be computed in LMC using the mean of the particle locations. The state estimate is then converted to latitude and longitude and the algorithm is done for this iteration.

If the dead-reckoning flag is set, meaning that at least one of the particles is outside of the map bounds, the algorithm skips directly to the dead-reckoning state estimation. In this case, the state estimates in LMC, latitude and longitude are computed using only the state update and the particle's states are reset to the dead-reckoned state estimate. The dead-reckoning flag is then reset in case all of the particles are back within the map bounds on the next iteration.

## 5.4 Offline Field Trials

The glider TAN algorithm was evaluated offline through data collected during two sets of field trials in Holyrood Arm of Conception Bay, Newfoundland. These experiments took place in October 2010 and October 2012 using a 200m electric Slocum underwater glider. In the 2010 trials the glider flew straight out of Holyrood Arm and past the boundary of the DPM for a total distance of approximately 12 km as in Fig. 5.3 and in the 2012 trials the vehicle flew in overlapping rectangles up Holyrood Arm for a total distance of approximately 91 km as illustrated in Fig. 5.4.

In both experiments the glider recorded its navigation data to allow for the glider TAN algorithm to be evaluated through post-processing. As no independent localization method, such as an ultra-short baseline system, was available the glider was programmed to surface approximately every hour and correct for the drift in its position estimate. As a result the glider's recorded dead-reckoned locations were able to be corrected using these GPS updates as illustrated in Fig. 5.5.

These corrections are performed by first assuming the difference between the dead-reckoned location estimate and GPS location estimate upon surfacing are the result of a constant velocity error term. This velocity, called the water depth averaged water velocity, is used to correct the locations of the previous leg producing the GPS corrected glider locations. These locations are used as the benchmark locations for comparison with the performance of the glider TAN algorithm. This method of

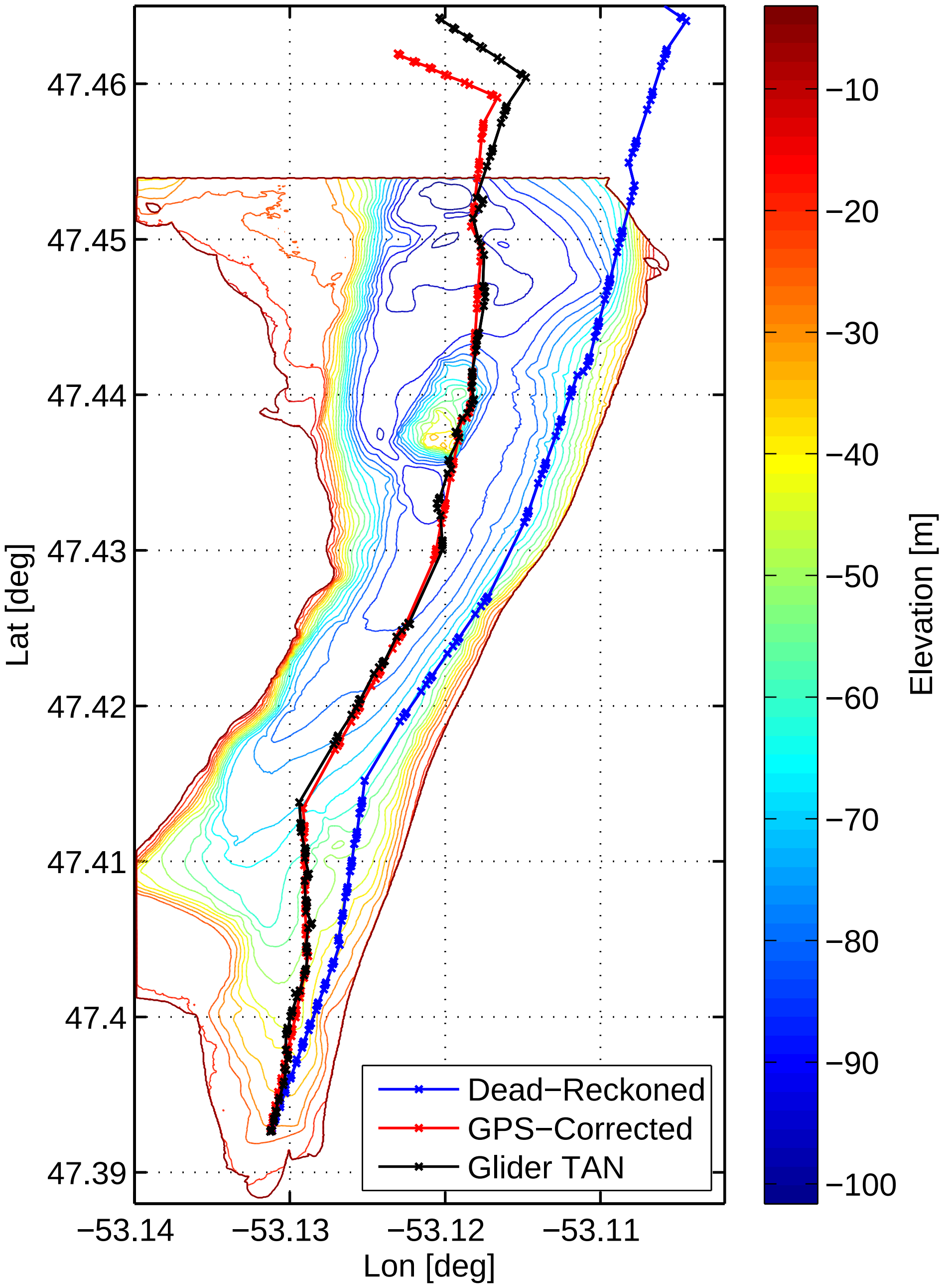

Figure 5.3: Location estimates from the glider TAN algorithm (black) against the GPS corrected dead-reckoned locations (red) and the dead-reckoned locations (blue) from the 2010 offline field trials

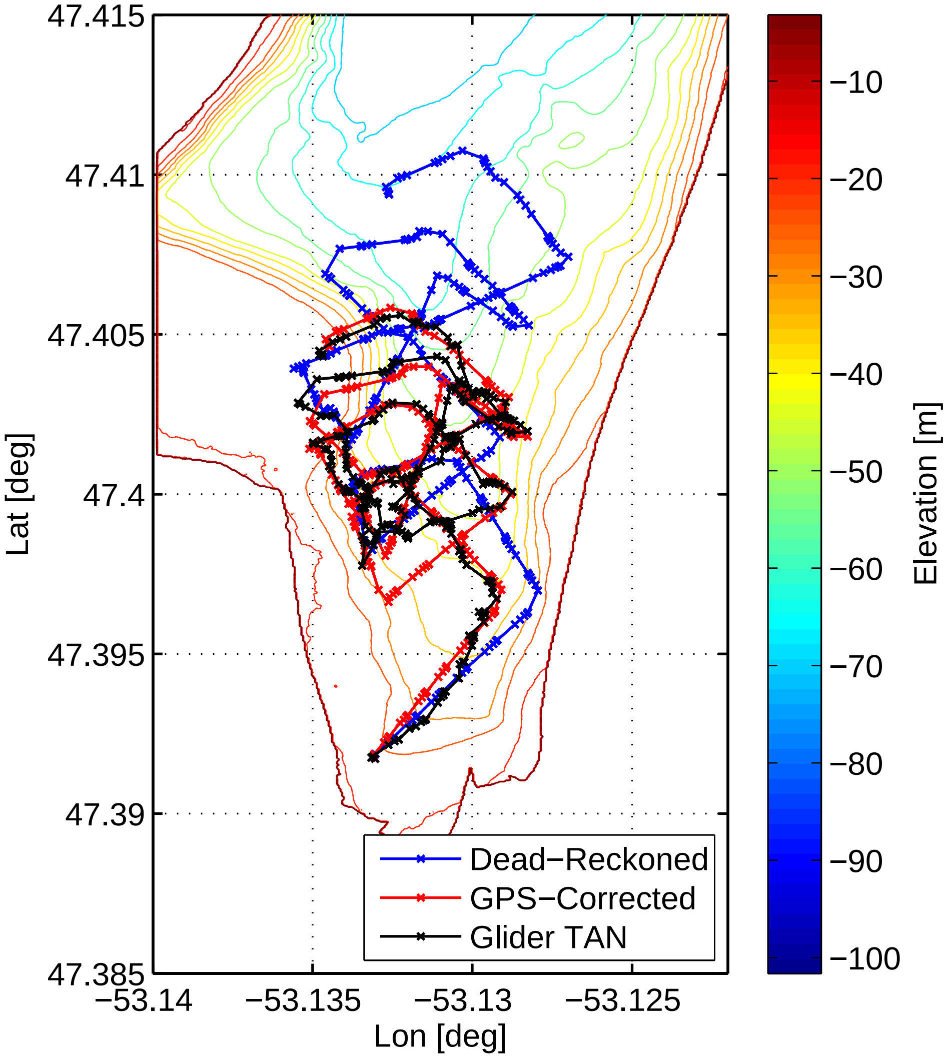

Figure 5.4: Location estimates from the glider TAN algorithm (black) against the GPS corrected dead-reckoned locations (red) and the dead-reckoned locations (blue) from the first 10 kilometers of the 2012 offline field trials

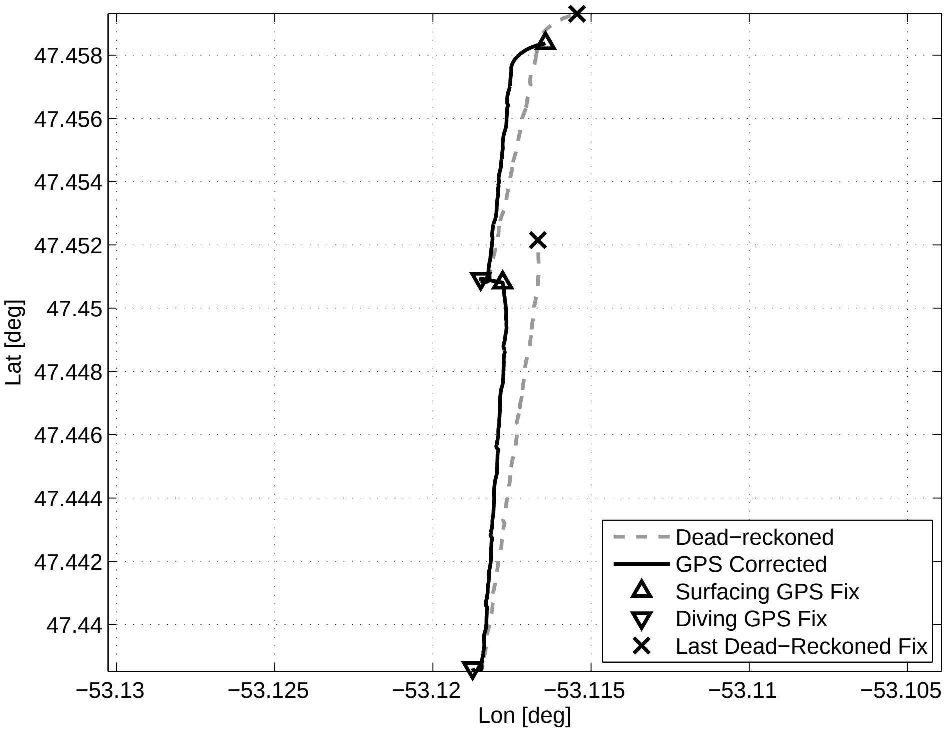

Figure 5.5: GPS corrected dead-reckoned location estimates computed from the dead-reckoned estimates using the difference between the last dead-reckoned estimate and the GPS fix upon surfacing applied as a constant disturbance from the diving GPS fix to the last dead-reckoned estimate

comparison is most accurate at the locations of the GPS updates during surfacing events with the uncertainty increasing to a maximum halfway between updates. It should also be noted that the glider does not record dead reckoning estimates during surfacing events. As such the surface drift is removed from the glider dead reckoning location estimates. In this process, the difference between the surfacing GPS location and the diving GPS location is removed such that dead reckoned locations do not have large discontinuities. Otherwise, the glider TAN algorithm only uses the GPS information for initialization of the algorithm prior to the first dive.

Altitude measurements are only acquired on the downward glide due to the shallow grazing angle on the upward glide as is illustrated in Fig. 5.6. Additionally, the period

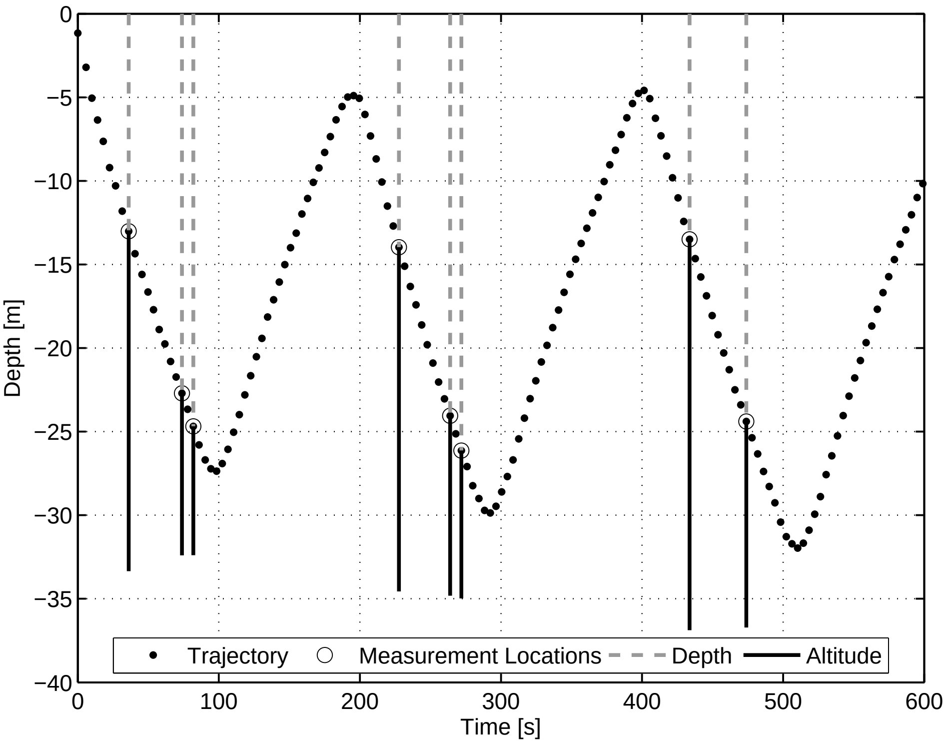

Figure 5.6: A sequence of measurements illustrating the construction of the water depth estimate using the vehicle depth and altitude measurements

between altitude measurements is not constant. In general the period is around 30 seconds, decreasing when it approaches the seafloor to about 10 seconds. This behavior is due to the vehicle's altimeter filter, which attempts to reject bad values and limit the energy consumed by the device. The histogram showing the time between altimeter measurements is shown in Fig. 5.7 with longer periods associated with the gap in measurements due to the climbing segments as shown in Fig. 5.6. The amount of time between subsequent measurements when the glider is climbing is dependent on the depth of the profiles the glider is performing. For the field trials in Holyrood Arm the maximum profile depth was around 100 meters. The glider's vertical velocity during these climbs was around 0.1 m/s, limiting the maximum time between measurement updates to around 20 minutes.

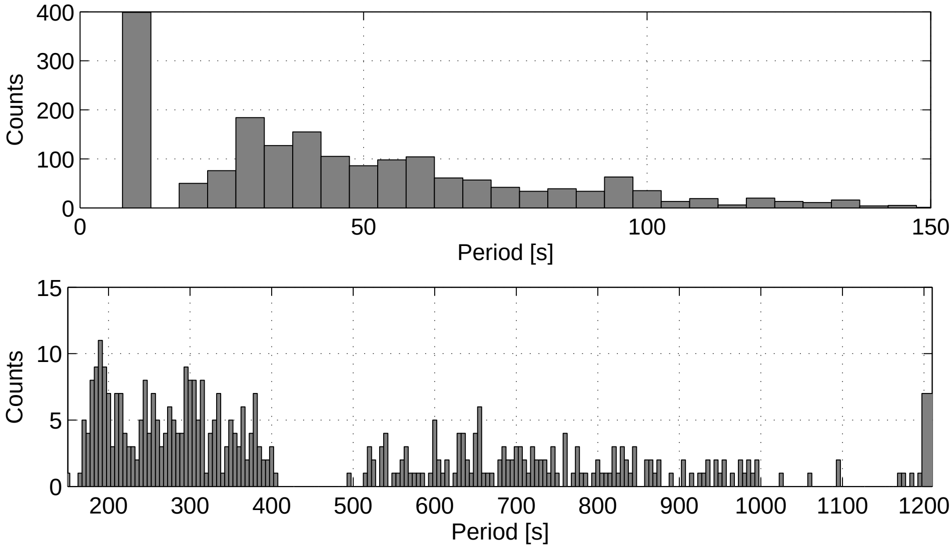

Figure 5.7: Histogram of the period between altimeter measurements in 5 second bins for periods between 0 and 150 seconds (top) and 150 and 1200 seconds (bottom)

The non-constant frequency of the altitude measurements during the downward glide followed by the large amount of time during the upward glide with no altitude measurements creates a unique challenge for a TAN algorithm. The structure of the bootstrap algorithm with jittering is well suited to this problem as it makes no assumptions about the frequency of the measurements. Additionally, because jittering and re-sampling are performed at every time step, the particle distribution rapidly adjusts to an accurate representation of the prior density function. This behavior is particularly helpful in maintaining convergence during large measurement update gaps due to a climbing section. For this work convergence was defined as whenever the glider TAN estimates improved on the dead reckoned location estimates.

The ray tracing algorithm's influence is illustrated in Fig. 5.8 by contrasting the error between the water depth estimates measured by the vehicle and the value given by the DPM before and after the ray tracing algorithm is applied. The water depths through which the altimeter's beam is ray traced are between 5 and 80 meters which is

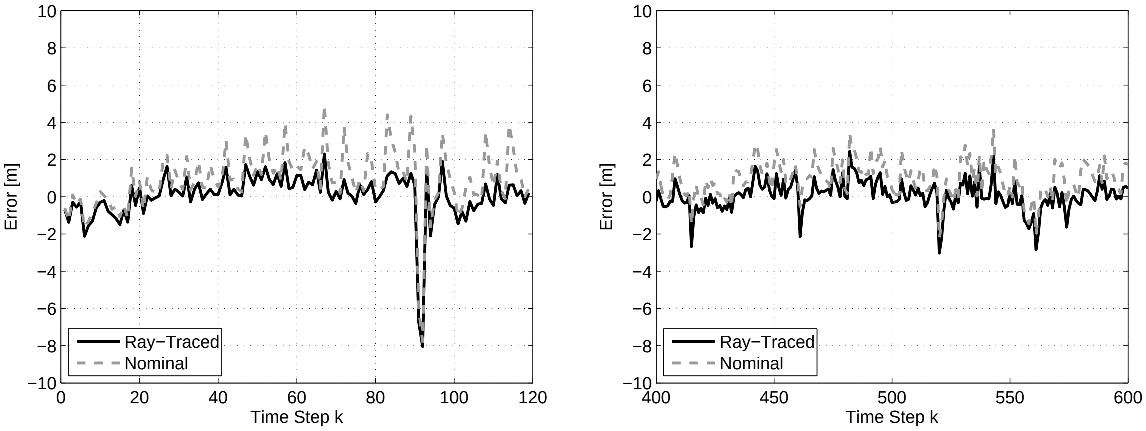

Figure 5.8: Water depth estimation error for the nominal and the ray traced estimate during the full set of 2010 trials (left) and a subset of the 2012 trials (right)

a relatively short distance for significant errors to accumulate for sound speed profiles in the deep ocean. However, in a coastal environment sharp gradients can be present in the sound speed profile leading to significant errors in the measured water depth estimate. This effect is evident in the difference between the ray traced and nominal errors in Fig. 5.8 where the ray traced errors are typically reduced. Occasional large errors are not corrected by the ray tracing procedure. These errors are attributed to fish or other unknown causes.

### 5.4.1 Offline Software Implementation

The software for the glider TAN post-processing was written using MATLAB®. To post-process the data from the 2010 and 2012 field trials the benchmark locations from the GPS corrected dead-reckoning and the dead-reckoning solutions with no GPS influence were computed. The glider's navigation system uses a correction algorithm to compensate for the water velocities based on the difference between the dead-reckoned error and the first GPS location upon surfacing. This correction is embedded in the dead-reckoning estimates the vehicle records requiring the post processing algorithms to strip out this effect in order to obtain the state updates independent of any GPS influence. The code then initializes the particle filter and runs through Algorithm 4 for every valid altimeter measurement. For comparison purposes, location errors are computed as the difference between the benchmark GPS corrected dead-reckoning locations and the location estimates produced by the glider TAN algorithm.

### 5.4.2 Sensitivity Analysis

The glider TAN algorithm's performance is impacted by a number of factors which may be varied to determine the sensitivity of the factor on the algorithm's convergence. These factors include the number of particles $N$, the jittering variance $\sigma_j^2$ and grid cell size of the DPM. The jittering variance was tested first using a relatively large number of particles, $N = 1000$, and the highest resolution DPM which is gridded at 2 meters. These tests were run five times for a range of jittering variance values between 2 $m^2$ and 30 $m^2$ with the results shown in Fig. 5.9.

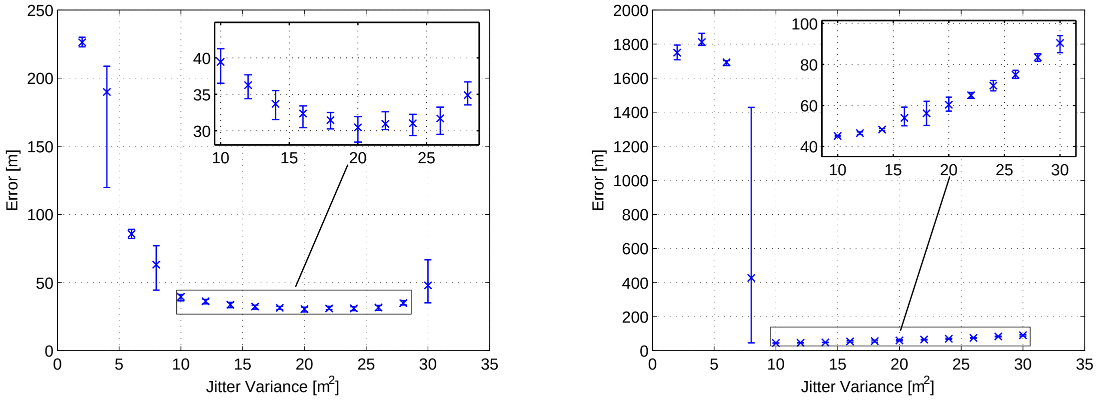

Figure 5.9: RMS errors of the glider TAN algorithm for different values of the jittering variance for the 2010 offline field trials (left) and the 2012 offline field trials (right) where the number of particles was 1000 and the DPM was gridded at 2 meters. The cross marks the mean RMS error and the upper and lower bars represent the maximum and minimum RMS error over a total of 5 Monte Carlo runs at each level. Insets show a close up of the area bounded by the box in each case.

The results of these tests show that there is a minimum jittering variance required for the algorithm to achieve convergence in both cases of around 10 $m^2$. The best values for the jittering variance in the 2010 trials appears to be in the range of 16 $m^2$ to 26 $m^2$. For the 2012 trials the best jittering variances are in the range of 10 $m^2$ to 14 $m^2$ with the RMS errors increasing steadily past this point. The differences in the RMS errors between the two trials for the jittering variance tests are attributed to the trials operating in different regions of the DPM and to variations in the accuracy of the dead-reckoning algorithm.

The effect of the grid size of the DPM was investigated next by re-gridding the DPM to a range of values from 2 meters up to 180 meters. The DPM was re-gridded by taking the mean of all of the points in the multibeam survey data that fell within each grid cell. The tests were run for 1000 particles and a jittering variance of 10 $m^2$, 15 $m^2$ and 20 $m^2$ as shown in Fig. 5.10.

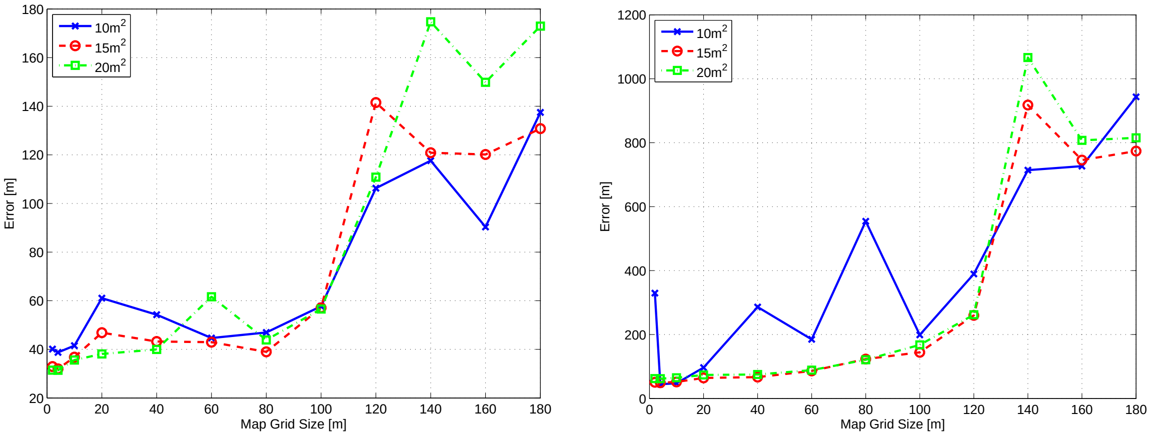

Figure 5.10: Average RMS errors of the glider TAN algorithm over five runs for different values of the grid cell size for the 2010 offline field trials (left) and the 2012 offline field trials (right) where the number of particles was 1000 and the jittering variance was 10 $m^2$, 15 $m^2$ and 20 $m^2$.

For both trials the algorithm maintained convergence for grid cell sizes ranging from 2 meters to 100 meters. The different values for the jittering variance are insignificant in the case of the 2010 trials but show a slight preference for 15 $m^2$ in the 2012 trials at the smaller grid cell sizes. In both cases the tests with a jittering variance of 10 $m^2$ showed a higher probability of divergence and no significant improvement in the RMS error.

While the degradation of the map grid cell size up to 100 meters may work well in Holyrood Arm it is unlikely that this constraint is able to be extrapolated to other regions. The accuracy with which a given grid represents the underlying bathymetry is location specific. It is therefore still uncertain whether global grids with a grid cell size of over 1 kilometer would be suitable. Likely, if further concessions to the accuracy of the TAN location estimates were able to be made, use of these global grids could be possible. Collection of data in offshore regions for offline evaluation is the subject of future work.

The number of particles for convergence was also tested, ranging from between 100 and 2000 as shown in Fig. 5.11. In these tests the jittering variance was 15 $m^2$ and the grid cell size was 2 meters.

In general, for particle filter algorithms more particles provides a better estimate of the underlying probability density function and thereby more confidence at the cost of processing time. Finding the number of particles to use for a particular application becomes an exercise in determining the minimum number of particles required to reliably retain convergence of the algorithm. In this case, a processing time of 0.105 seconds was required for each timestep at 1000 particles on a desktop computer with an i5 660 3.33 GHz processor. For the five Monte Carlo runs examining the number of particles needed for convergence during the 2010 and 2012 field trials, the average RMS error levels out at around 500 particles in both cases. To ensure convergence, 1000 particles were selected for nominal use.

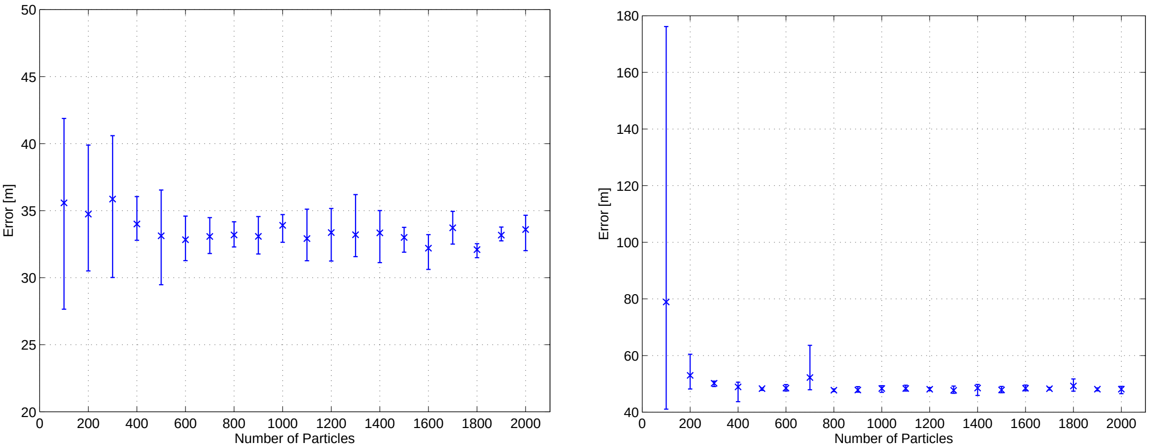

Figure 5.11: RMS errors of the glider TAN algorithm for different values of the number of particles for the 2010 offline field trials (left) and the 2012 offline field trials (right) where the jittering variance was 15 $m^2$ and the grid cell size was 2 meters. The cross marks the mean RMS error and the upper and lower bars represent the maximum and minimum RMS error over a total of 5 Monte Carlo runs at each level.

### 5.4.3 Results

Using the jittering variance and number of particles determined from the sensitivity analysis the glider TAN location estimates are computed through 100 Monte Carlo simulations with the RMS and peak errors shown in Fig. 5.12.

Convergence was maintained in all of the 100 Monte Carlo simulations of the glider TAN algorithm for a jittering variance of 15 $m^2$, 1000 particles, and a grid cell size of 2 meters for both trials. The average RMS error in the 2010 trials was 33 meters with an average peak error of 96 meters. For the 2012 trials the average RMS error was 50 meters with an average peak error of 532 meters. To determine the efficiency of an estimator an estimate is often compared with a lower bound to illustrate how well it performs relative to the best possible case. To this end a comparison of the mean error with the dead-reckoned location estimates along with the Monte Carlo Lower Bound (MCLB) is shown in Fig. 5.13 where the MCLB is the minimum value over the set of Monte Carlo runs.

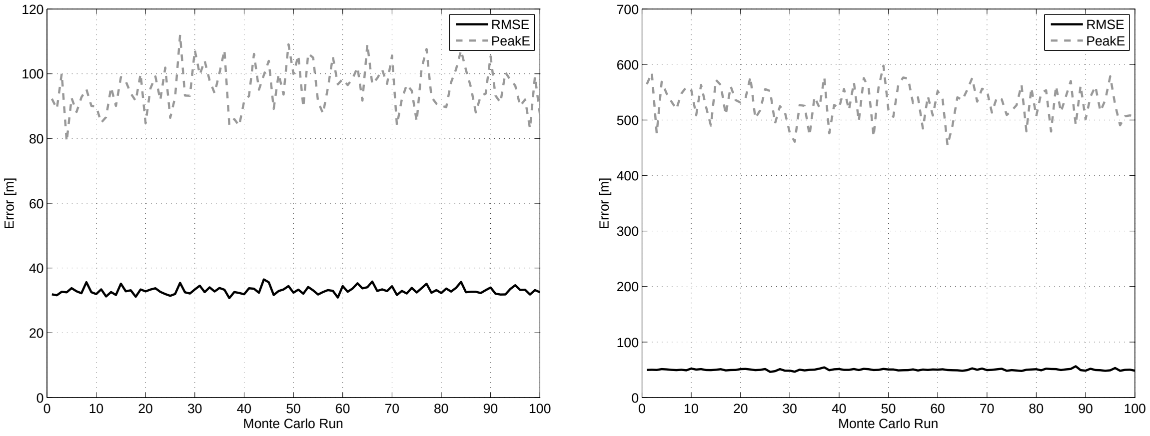

Figure 5.12: RMS error and peak error from 100 Monte Carlo simulations of the glider TAN algorithm for the 2010 offline trials (left) and the 2012 offline trials (right) with a jittering variance of 15 $m^2$, 1000 particles, and a grid cell size of 2 meters

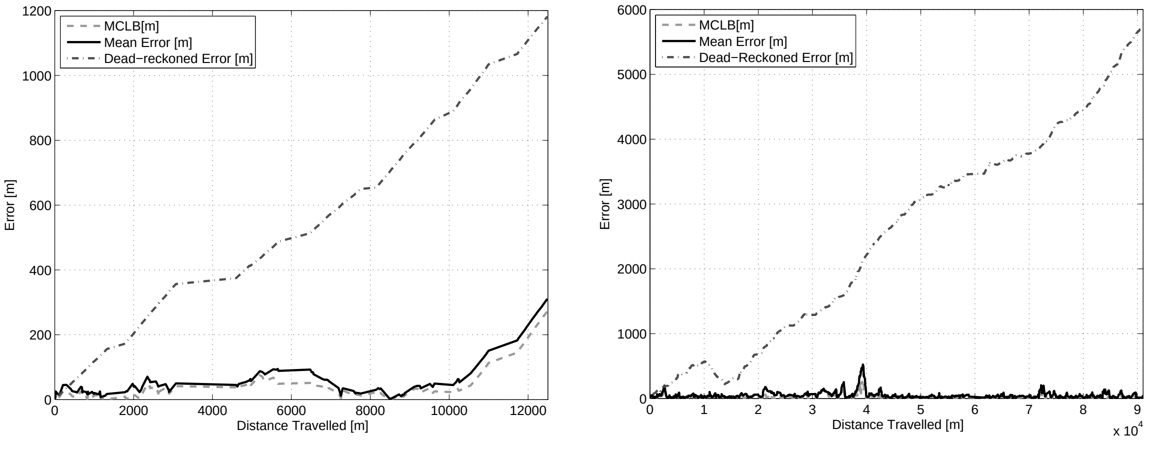

Figure 5.13: Improvement of the glider TAN algorithm over the dead-reckoned error computed from 100 Monte Carlo simulations of the glider TAN algorithm from the 2010 offline trials (left) and the 2012 offline trials (right)

The improvement of the glider TAN location estimates over the dead-reckoned location estimates is shown by the bounded error estimates as in Fig. 5.13. In the 2010 trials the dead-reckoned error reaches around 900 meters during the time the algorithm is within the bounds of the DPM while the glider TAN error at the same time step is only around 44 meters. In the 2012 trials the dead-reckoned error reaches over 5.5 km while at the end of the mission the glider TAN error is only 16 meters. Additionally, while the glider TAN algorithm shows occasional periods of divergence, the algorithm is able to re-converge shortly after. These periods of divergence along with a closer look at the mean error, Monte Carlo Upper Bound (MCUB), Monte Carlo Lower Bound (MCLB) and DPM flags are illustrated in Fig. 5.14.

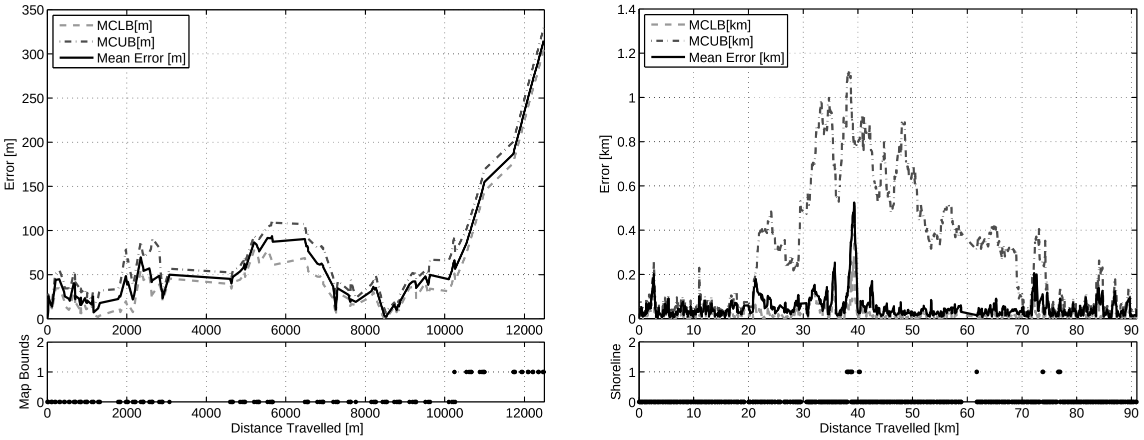

Figure 5.14: Mean RMS error, Monte Carlo Upper Bound (MCUB) and Monte Carlo Lower Bound (MCLB) from 100 Monte Carlo simulations of the glider TAN algorithm from the 2010 offline trials (top left) with the map bounds flag shown (bottom left). The mean RMS error, MCUB and MCLB from the 2012 offline trials (top right) with the shore line flag shown (bottom right). The flag markers are shown at every altimeter reading with a 1 indicating a particle is out of bounds.

In the 2010 trials the main divergence is after the map bounds flag goes high due to the vehicle leaving the bounds of the DPM. At this point the dead reckoned location estimates take over. For the 2012 trials the glider TAN algorithm maintains convergence during most of the deployment. Occasional spikes in the error are noticeable with the largest occurring around 38 kilometers into the mission and reaching 532 meters. This large error corresponds with the shoreline flag and is due to the glider being in shallow water during this portion of the trials. In shallow water the glider's 200 meter pump is not fast enough to keep the vehicle's speed up, resulting in the dead reckoning algorithm deteriorating on the vehicle and many altimeter measurements being performed in the same region. In effect the vehicle estimates it is moving faster than it is and water depth estimates are not changing very much during this time. However, once the vehicle leaves the proximity of the shore line the algorithm quickly re-converges.

The MCUB and MCLB represent the maximum and minimum value observed at a time step over the entire set of Monte Carlo runs. The MCUB and MCLB give an indication of the absolute worse and best possible scenario.

A visual representation of the performance of the glider TAN algorithm for the 2010 trials and for the first 10 kilometers of the 2012 trials is presented in Figs. 5.3 and 5.4. These figures highlight the improvement provided by the glider TAN algorithm over the pure dead-reckoning location estimates and give confidence towards online localization efforts.

## 5.5 Hardware and Software Integration

The Teledyne Webb Research Slocum Electric glider has two embedded processors on-board, one for navigation and control termed the glider computer and one for the integration of payloads and sensors termed the science computer. These processors run a derivative of DOS on a 14 MHz Motorolla MC68CK338 which is packaged into the Persistor CF1 embedded computer. The Persistor has 1 Mb of flash memory and a standard suite of embedded interfaces including a hardware interface to Compact

Flash memory storage. While these devices provide a low power, reliable platform for the operation and control of the vehicle the memory and processing requirements of the particle filter algorithm exceeds their ability. As such, this section describes the integration of an additional single board computer into the glider in order to run the algorithm.

Initial tests were performed with low power ARM M0 processors which have similar memory capacities as the CF1 but run at frequencies of 40 MHz. The memory limitations required approximating the particle filter to avoid storing the prior particle states and placed a limit on the number of particles. While these processors are capable of running the algorithm in real-time, the approximated method was found to insufficiently represent the underlying probability density function resulting in unsatisfactory performance [187].

Subsequently, the more powerful Beagle Bone Black (BBB), Fig. 5.15 single board computer was selected for use. The BBB has a 1 GHz ARM Cortex-A8 processor with 512 Mb of RAM, 4 Gb of on-board flash and standard set of embedded peripheral options. For this work the BBB's operating system was selected to be Ubuntu 13.04,

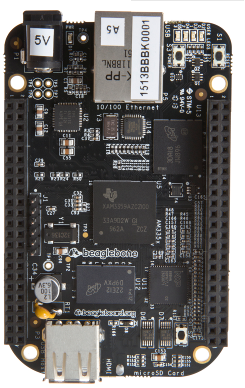

Figure 5.15: The Beagle Bone Black 1 GHz Arm Cortex-A8 processor with 512 Mb of RAM and 4 Gb of onboard flash

allowing the particle filter to be programmed in C/C++. The BBB has a frequency scaling module which adjusts the processor frequency depending on the demand. The voltage supply to the board is 5 Volts with a current draw of around 300 mA during boot (10 seconds) and while processing, dropping to 100 mA while idle. The BBB is powered through a separate switching regulator from the standard power pins in the payload module which supplies 10 to 15 Volts. The communication interface connects from the 5 Volt UART on the BBB through a logic level converter to the standard RS232 port on the science computer of the glider. In this way the BBB connects to the glider as any payload or science sensor would as illustrated in Fig. 5.16.

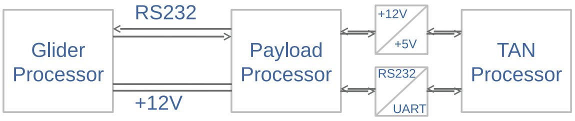

Figure 5.16: Diagram of the glider Terrain Aided Navigation hardware integration showing the power and communication connections to the science computer

The particle filter program that runs on the BBB is configured to run as a background process once the operating system has booted. The UART and processor options are also configured at boot-time. The particle filter code accepts an initialization command and an update command from the vehicle. The initialization command sets the reference location for the local mission coordinate frame and resets the particle locations to this initial location. The update command computes one iteration of the particle filter and sends a location update and status flag back to the vehicle. The status flag indicates if the location update is nominal, near shore, or near the map bounds. The computation time for the update command is approximately 10 milliseconds making it more than adequate for the fastest possible update rate of 4 seconds.

On the science processor a glider TAN "proglet" interfaces to the BBB issuing commands to the BBB and requesting the attitude; altitude; depth; dead-reckoned latitude and longitude; GPS latitude and longitude; and the local mission coordinate locations from the glider computer. These variables are updated from the glider processor to the science processor as they are available. Whenever the GPS latitude and longitude variables are updated on the science processor it sends the initialization command to the BBB. In this way the best navigation data is always used. Subsequent to the first initialization, any updates to the altitude variable trigger the transmission of the update command to the BBB. The BBB then computes a location based on the TAN particle filter and sends a location update and status flag back to the science computer where the open loop locations are logged for future analysis. While closed loop trials are the ultimate goal of this work, sending variables back to the glider requires modification of the glider processor's source code which was not possible at this time. Additionally, an independent localization method such as a USBL is desired for validation of the results which was not available for use as of this writing. For this reason closed loop trials remain the subject of future work.

## 5.6 Online Field Trials

Online tests of the glider TAN method were performed in Holyrood Arm of Conception Bay, Newfoundland during September, 2014. During these tests the glider was flown in a northward and southward straight line segment for roughly one hour in each direction. The glider TAN processor computed open loop location estimates which were then stored on the science computer's flash memory. An initial set of three profiles was performed to extract the depth bias of the DPM and confirm the operation of the TAN system. The vehicle was configured to not correct for water velocities which requires multiple surfacing events, as this is most representative of a longer distance closed loop mission. The results of the open loop glider TAN locations are shown relative to the dead-reckoning location estimates and GPS corrected locations in Fig. 5.17.

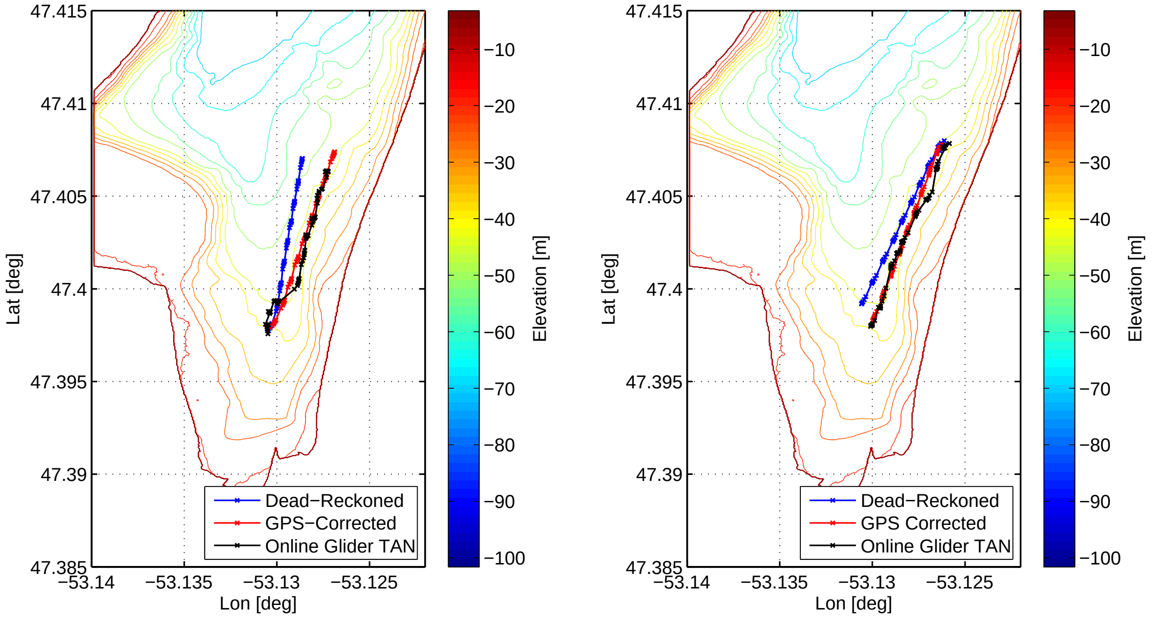

Figure 5.17: Online open loop location estimates from the glider TAN algorithm (black) against the GPS corrected locations (red) and the dead-reckoned locations (blue) from the 2014 online trials northward leg (left) and southward leg (right)

During the northward trial the GPS corrected estimates are slightly east of the dead-reckoned estimates likely due to some local tidal current. The online glider TAN estimates converge to the correct water depth after a short period with some along track error.

During the southward trial the GPS corrected estimates are again slightly east of the dead-reckoned estimates. As these trials occurred immediately following the northward leg, this further supports the existence of an easterly tidal current that is decreasing in magnitude. For these trials the online glider TAN estimates again converge to the vehicle track after a short period, this time with less along track error.

The error between the GPS corrected location estimates and the online glider TAN estimates are shown relative to the dead-reckoned error in Fig. 5.18.

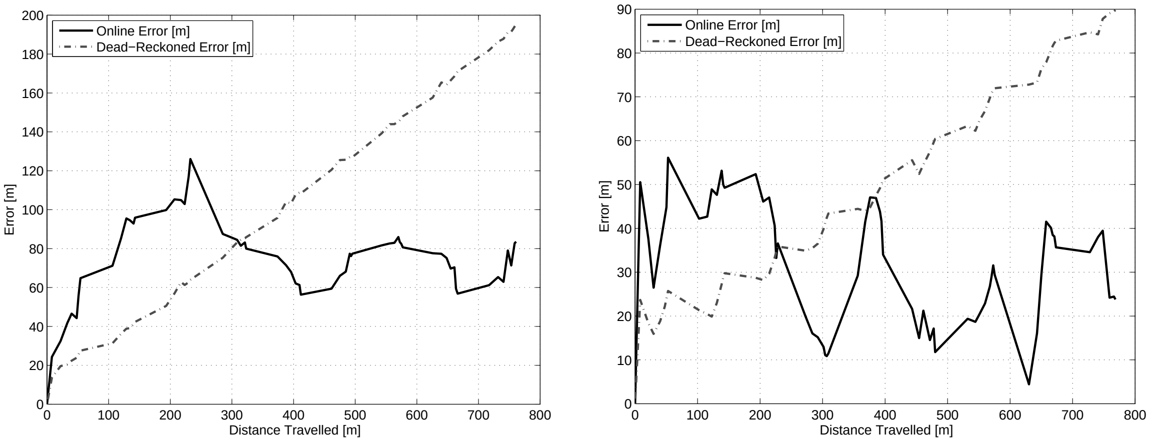

Figure 5.18: Improvement of the glider TAN algorithm over the dead-reckoned error during the 2014 online trials northward leg (left) and southward leg (right)

The online glider TAN errors in both the northward and the southward leg improve upon the dead-reckoned error. Specifically the mean RMS error in the northward leg was 76 meters and during the southward leg was 32 meters. The dead-reckoned error growth rates were 25.6 and 11.6 percent of distance traveled for the northward and southward legs respectively. The relatively large RMS error of the online glider TAN estimates during the northward leg is therefore attributed to this increased dead-reckoning error growth rate. These large error growth rates are due to the vehicle's slow speed relative to the tidal water currents during the tests and the dead-reckoning computation relying on the speed through water instead of the speed over ground. Despite the presence of the variable tidal current the glider TAN algorithm is able to provide bounded error location estimates, improving on the dead reckoned location estimates.

# Chapter 6

# Magnetic Data Collection

The use of magnetic field measurements as a heading reference for navigation in underwater vehicles has been well established [21]. In recent work earth magnetic information has also been suggested for possible use in total-field map based relative navigation techniques [38, 37]. This use of magnetic measurements for online navigational aiding is the motivation for this research. In such a system, magnetic measurements are capable of augmenting a terrain relative navigation scheme in regions of low terrain variability or when the terrain is beyond the range of the vehicle's acoustic sensors. However, an online implementation of a magnetic aided navigation system has not been realised. This lack of progress has been limited by the challenges involved in instrumenting and calibrating an underwater vehicle for accurate online magnetic measurements and the lack of suitably high resolution magnetic maps.

As a step towards a real time total field magnetically aided navigation system this chapter examines suitable methods for calibrating, instrumenting and performing magnetic measurements with an underwater glider. The variable locations of the mass shifting and ballast mechanisms on the underwater glider provide an additional challenge for calibrating the magnetic measurement system. As such, a calibration method where the vehicle actuators are stationary is presented first. Following which, a parameterized calibration method is presented which attempts to fit polynomial functions to the calibration parameters based on the actuator locations. To this end the theory for fixed calibrations and parameterized calibrations is presented and the underwater glider equipped with the magnetic instrumentation developed for this work is introduced. Lastly, the calibration procedures are demonstrated on field data gathered using the underwater glider during trials in the East Arm of Bonne Bay, Newfoundland and in the Labrador Sea. The calibrated data are compared with magnetic anomaly models of each respective region.

## 6.1 Calibration Methods

Measurements of the earth's magnetic field must be calibrated to remove the effects of the sensing platform. These effects can be due to instrument non-linearities as well as hard and soft magnetic effects. Scalar calibration of vector magnetometers has shown to be a robust method of calibration based on a geometric fit to an ellipsoid [132, 162, 157]. Another method relies on projecting the measurement vector onto the horizontal plane and fitting an ellipse [143, 144]. Of these methods, the second is more suited to vehicles which have limitations in the controllable degrees of freedom such as an underwater glider. However, it requires a precision attitude reference to rotate the magnetic measurements to the horizontal plane which is infeasible on an underwater glider due to their energy consumption. Additionally, long range underwater vehicles, and underwater gliders in particular, require additional effort to calibrate the magnetic field measurements. This extra effort is due to the use of an adjustable internal mass for attitude control which is typically composed of a battery pack and therefore includes hard and soft magnetic materials.

### 6.1.1 Fixed Calibration

If the moving masses in the underwater glider are held stationary the hard and soft magnetic effects from the vehicle as well as scaling, bias and other instrument errors may be calibrated for using geometric batch methods [132, 162, 157]. These methods assume a constant magnetic field and rely on rotations of the instrument through the calibration space such that an ellipsoid may be fit to the data.

An ideal magnetic sensor at a fixed location produces measurements with a constant magnitude resulting in the data lying on the surface of a sphere, centered on the origin with the radius equal to this magnitude. Distortions due to the sensor errors and the vehicle have been shown to cause the measurements to be translated, rotated and scaled such that the sphere becomes an ellipsoid. The problem of finding a set of translation, scaling and rotation coefficients can be expressed in a matrix notation as

$$[\mathbf{M}, \mathbf{S}, \mathbf{T}] = G(\mathbf{H}_r) \tag{6.1}$$

where $\mathbf{M}$, $\mathbf{S}$, and $\mathbf{T}$ are the rotation, scaling and translation matrices that are representative of the ellipsoidal fit $G()$ to the raw magnetic data $\mathbf{H}_r$. Geometrically, the translation coefficients are the distance from the center of the ellipsoid to the origin, the scaling coefficients are the magnitudes of the major and minor ellipsoid axes and the rotation coefficients are the rotations of the major and minor axes of the ellipsoid. The ellipsoid equation representing the relationship between the raw magnetic data and the corrected data is written in matrix notation as

$$\mathbf{H}_r = H_e^{-1}\mathbf{S}\mathbf{M}\mathbf{H}_c + \mathbf{T} \tag{6.2}$$

The raw magnetic data may then be translated, rotated and scaled accordingly by re-arranging the ellipsoid equation to

$$\mathbf{H}_c = H_e \mathbf{S}^{-1} \mathbf{M}^{-1} (\mathbf{H}_r - \mathbf{T}) \tag{6.3}$$

where $\mathbf{H}_c$ is the calibrated magnetic data in the sensor frame. This calibration procedure normalizes the magnitude of the magnetic measurements due to the product of the inverse of the scaling coefficients. To give the calibrated values units, the normalized values must be scaled by the magnitude of the local magnetic field at the calibration location $H_e$ which often may be approximated from the International Geomagnetic Reference Field (IGRF). The IGRF does not include many of the higher frequency components and the local magnetic anomalies. If a local anomaly map is available these anomaly values may be included as in

$$H_e = ||\mathbf{H}_{IGRF}|| + H_a \tag{6.4}$$

where $H_a$ is the magnitude of the magnetic anomalies at the calibration locations. The resulting values given by $\mathbf{H}_c$ are the calibrated measurements of the magnetic field for a vehicle with fixed locations of the hard and soft magnetic influences and no significant electrical currents.

### 6.1.2 Parameterized Calibration

For vehicles with moving hard or soft magnetic parts that have a number of steady state values a parameterized version of the geometric calibration method is proposed. In this method the fixed calibration procedure from Section 6.1.1 is performed for a number of different steady state values for each of the moving parts. In this way the variation in the calibration coefficients may be represented by a polynomial function.

In the case of underwater gliders, the primary factors are the moving mass mechanism used for fine control of the vehicle pitch and the ballast mechanism which is responsible for the large pitch and buoyancy changes between diving and climbing. The geometric fitting then becomes of the form

$$[\mathbf{M}, \mathbf{S}, \mathbf{T}](p_m, p_b) = G(\mathbf{H}_r(p_m, p_b)) \tag{6.5}$$

where each of the rotation, translation and scaling coefficients is a function of the moving mass location $p_m$ and the ballast piston location $p_b$. The parameterized functions are found by fitting polynomials to the set of individual calibration coefficients found for a geometric fit to the magnetic measurements for a given moving mass and ballast location. The parameterized ellipsoid equation is similarly given as

$$\mathbf{H}_r = H_e^{-1}\mathbf{S}(p_m, p_b)\mathbf{M}(p_m, p_b)\mathbf{H}_c + \mathbf{T}(p_m, p_b) \tag{6.6}$$

Upon re-arranging, the raw magnetic data may be corrected by computing the translation, rotation and scaling matrices for a given moving mass and ballast location as in

$$\mathbf{H}_c = H_e\mathbf{S}(p_m, p_b)^{-1}\mathbf{M}(p_m, p_b)^{-1}(\mathbf{H}_r - \mathbf{T}(p_m, p_b)) \tag{6.7}$$

## 6.2 Instrumentation

An underwater glider's energy is provided by onboard batteries which gives it an endurance of around one month when using alkaline primary cells and six months when using lithium primary cells. In a standard configuration of a vehicle equipped only with a conductivity, temperature and pressure sensor (CTD), the vehicle uses an average power of around one Watt. To not significantly impact the endurance or range of the vehicle, additional sensors should use as little power as possible. Therefore, to instrument an underwater glider with a magnetic sensor, the power consumption of the device must remain low to minimize the impact on the vehicle's endurance.

While progress is being made towards lower power cesium vapour magnetometers which would be well suited to integration in mobile platforms, the power consumption of currently available devices still remains on the order of Watts [140, 141]. Fluxgate sensors, on the other hand, have power requirements down to the level of 10s of milliwatts. For this reason the chosen sensor is a low power tri-axial Mag-648 fluxgate magnetometer by Bartington Instruments which consumes around 14 milliwatts [137]. Low power fluxgates of this type are often subject to higher degrees of noise, orthogonality errors, and offset errors than higher power versions [136]. While the impact of the higher noise is mitigated through low frequency sampling requirements, the orthogonality errors and offset errors require careful calibration. Additionally, the offset error settles to a slightly different value each time the sensor is powered on requiring the sensor to remain energized once calibrated.

The fluxgate sensor is mounted in a strap-down configuration in the vehicle's payload bay. The device is powered by a set of independent batteries and is sampled using an isolated analog to digital converter (ADC) as illustrated in Fig. 6.1. The differential output voltages of the sensor are read by the 24-bit AD7794 sigma-delta ADC. This ADC uses several different internal low pass filters and modifies the filter coefficients based on the sampling rate selected. The effective resolution of the device is therefore variable with the sampling rate. The inputs to the ADC have anti-aliasing filters with a corner frequency of 1 Hz to mitigate high frequency noise from the electronics and other systems. The ADC uses the serial peripheral interface (SPI) to send the data to the glider payload computer where it is logged at a frequency

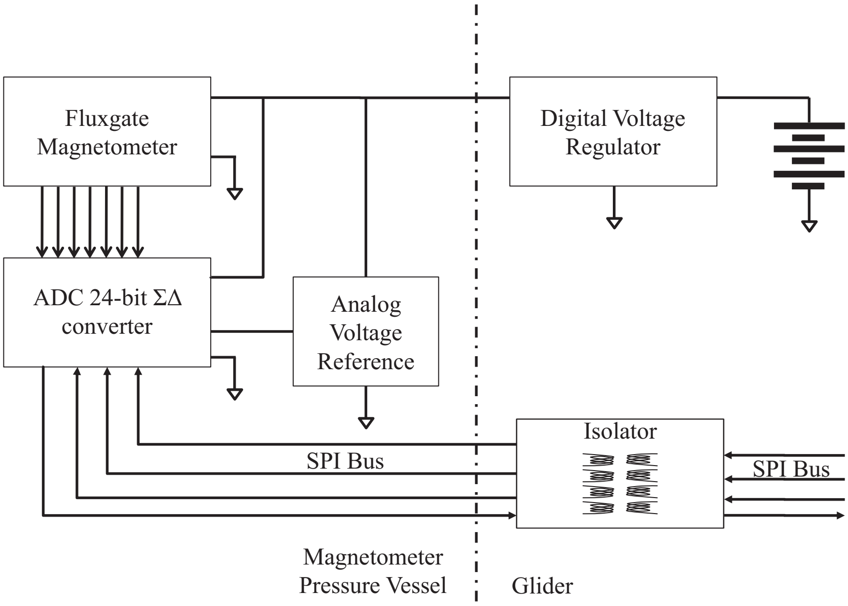

Figure 6.1: Fluxgate sampling electronics diagram illustrating the signal flow from the fluxgate sensor to the analog to digital converter (ADC) and onwards through the digital isolator to the vehicle payload computer for logging. Power for the device is provided by a dedicated set of batteries to isolate the system from the vehicle noise.

of 0.25 Hz. The ADC used has a single digitizer and samples of each channel are taken at different times requiring the time stamp of each channel's measurement to be recorded such that the measurements may be interpolated to the same time base. The electrical current drawn by the fluxgate and its electronics is around 4.5 mA. As a result of this low energy consumption, a single set of three AA alkaline cells connected in series will power the fluxgate and its electronics for one month. The goal of not influencing the endurance of the underwater glider while staying within the size and weight requirements for the payload are therefore achieved.

## 6.3 Field Trials

Two sets of field trials using the magnetic fluxgate sensor installed on the 200 meter Slocum Electric glider were performed to evaluate the efficacy of making magnetic measurements using this platform. The initial trials were performed to evaluate the parameterized calibration method. During these trials it was determined that the calibration could be performed for a single set of parameters and the subsequent trials made use of this method. The field trials utilizing the single set of parameters took place in the Labrador Sea in July, 2014 and will be presented first. The parameterized calibration method trials took place in December, 2013 in the East Arm of Bonne Bay, Newfoundland and will be presented second. The trials are presented out of chronological order to match the presentation of the theory earlier in which the parameterized calibration method is an extension of the fixed calibration method. The locations of these trials are shown in Fig. 6.2 in relation to Newfoundland and Labrador.

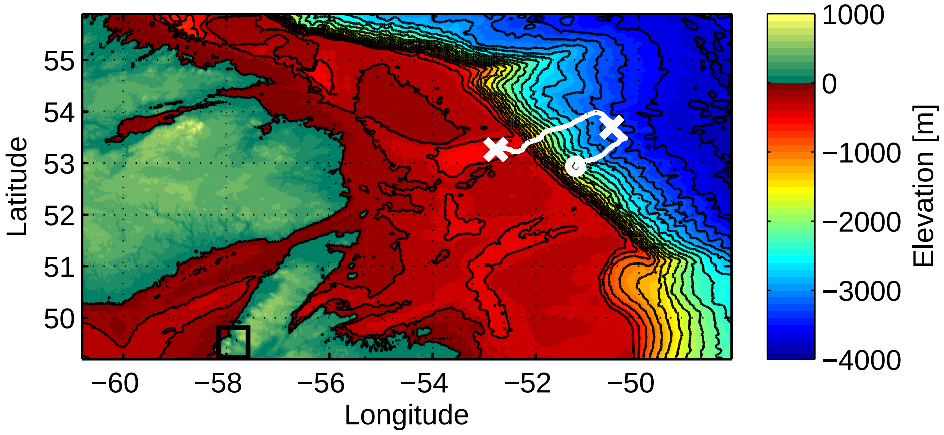

Figure 6.2: Locations of the magnetic data collection trials where the Bonne Bay trials are marked by the black square and the Labrador Sea trials are marked by the white line, circle and crosses. In the Labrador Sea trials the start of the trials is indicated by the circle and the two crosses indicate the calibration locations.

### 6.3.1 Fixed Parameter Trials in the Labrador Sea

The Labrador Sea field trials utilizing a fixed parameter calibration method started on July 4th, 2014. The underwater glider equipped with the fluxgate sensor was launched from the Canadian Coast Guard Ship Hudson's fast rescue craft as shown in Fig. 6.3 as part of the larger Ventilation, Interactions and Transports Across the Labrador Sea project. In total, 13 days of data were collected for a total linear distance of around 250 kilometers. On July 17 the vehicle reported a leak, cutting short the mission and requiring the recovery of the platform.

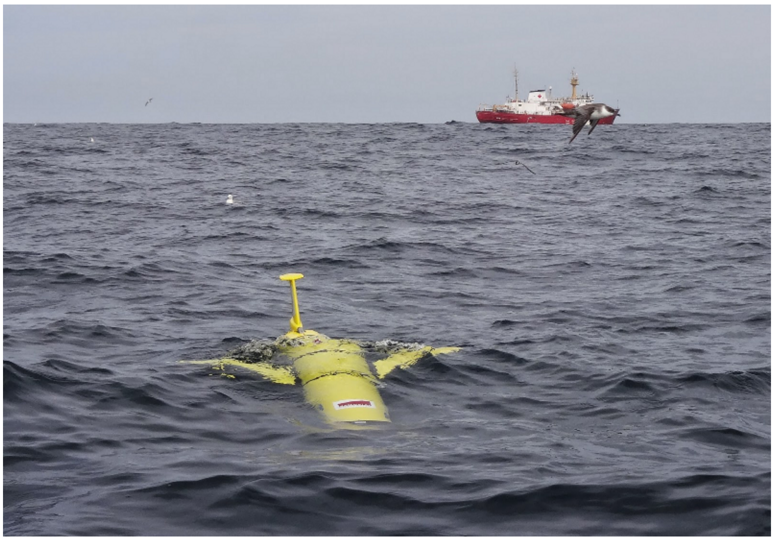

Figure 6.3: Launch of an autonomous underwater glider during the Labrador Sea experiments from the Canadian Coast Guard Ship Hudson's fast rescue craft. Image Credit: Robin Matthews

Prior to deployment the vehicle was carefully ballasted and trimmed such that the commanded ballast results in symmetric dive and climb speeds and the mass shifting mechanism is capable of controlling the pitch to the desired value for an assumed water density. During the launch of the vehicle an initial profile was performed to half the rated depth of ballast engine to depassivate the lithium batteries as per the manufacturers recommendations. During this profile the vehicle was allowed to servo the mass shifting mechanism to a commanded pitch of 26 degrees. Upon surfacing, the mass shifting locations from the steady state portions of the profile were extracted as illustrated by Fig. 6.4. The primary mission script, as well as the calibration mission scripts, were then programmed to use this steady state mass shifting location from the dive and the climb as shown in Table 6.1.

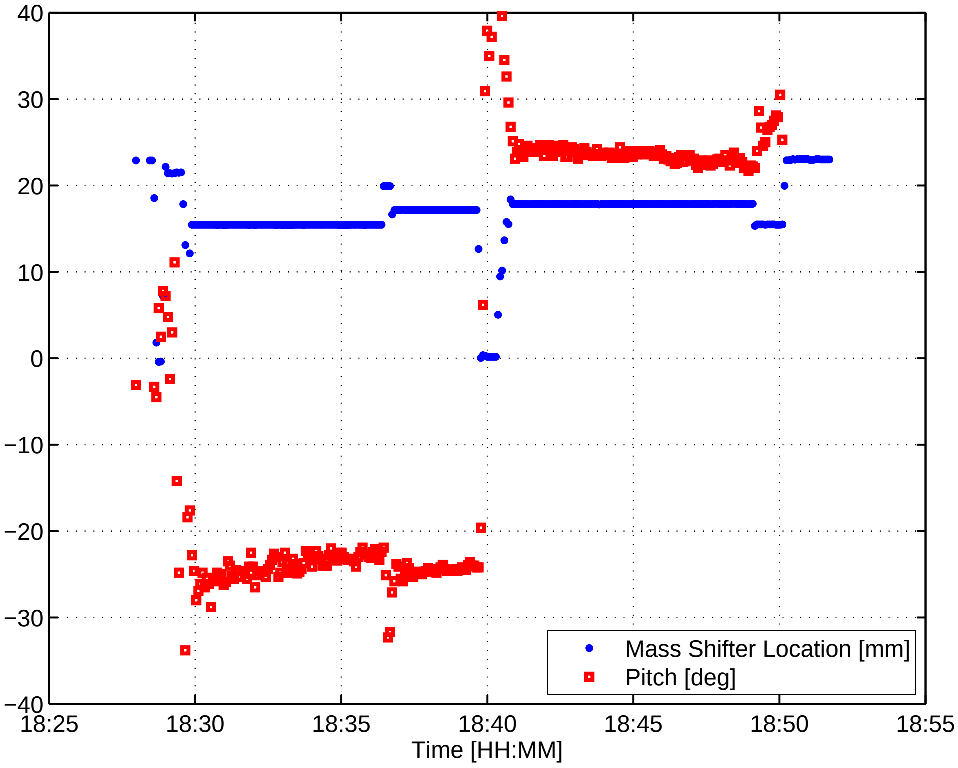

Figure 6.4: Mass shifting mechanism location and pitch for the underwater glider during the depassivation profile from which the steady state values of the mass shifting mechanism locations are extracted.

The battery locations resulting in nominally 26 degree profiles are both set forward of the neutral location due to mass distribution in the vehicle, suggesting the vehicle is heavy in the tail. The range of the mass shifter values from the dive to climb is only 0.062 inches. In the Labrador Sea mission this range was within the deadband of the mass shifting mechanism controller. The mass shifting mechanism, therefore,

Table 6.1: Calibration runs for the fixed magnetic calibration trials

| Run | Direction | Ballast [$cm^3$] | Rotation | Battery Command Trial 1 [mm] | Battery Command Trial 2 [mm] |
|---|---|---|---|---|---|
| 1 | Dive | -200 | CW | 16.25 | 16.25 |
| 2 | Climb | 200 | CW | 17.83 | 17.83 |
| 1 | Dive | -200 | CCW | 16.25 | 16.25 |
| 2 | Climb | 200 | CCW | 17.83 | 17.83 |

did not move between the dive and climbing portions of the profile in this mission.

Twice throughout the trials, around once a week, a set of clockwise and counter-clockwise spiralling profiles were performed. The locations of these calibration spirals against the magnetic anomaly model are shown in Fig. 6.5.

The extraction of the magnetic calibration parameters using ellipsoid fit methods generally requires adequate coverage of the calibration space such that the ellipsoid is constrained. A single descending or ascending spiral results in a single circle in the calibration space which is insufficient to constrain the ellipsoid. To deal with this sparsity, an initial global fit was performed by using this full set of raw measurements from the diving and climbing calibration runs. In this case the calibration data appears as two circles representing the diving and climbing spirals as shown in Fig. 6.6. Further, the ellipsoid was constrained in rotation such that $\mathbf{M} = \mathbf{I}$ to reduce the number of calibration parameters. Normally, the rotations in $\mathbf{M}$ account for the orthogonality errors in the instrument. While the Mag648 fluxgate sensor is known to have slight orthogonality errors the coverage of the calibration space as illustrated in Fig. 6.6 is insufficient to resolve these rotations [137].

If the scaling and translation parameters from the initial ellipsoid fit are used to correct the magnetic data from these calibration spirals, with the magnitude $H_e$ given

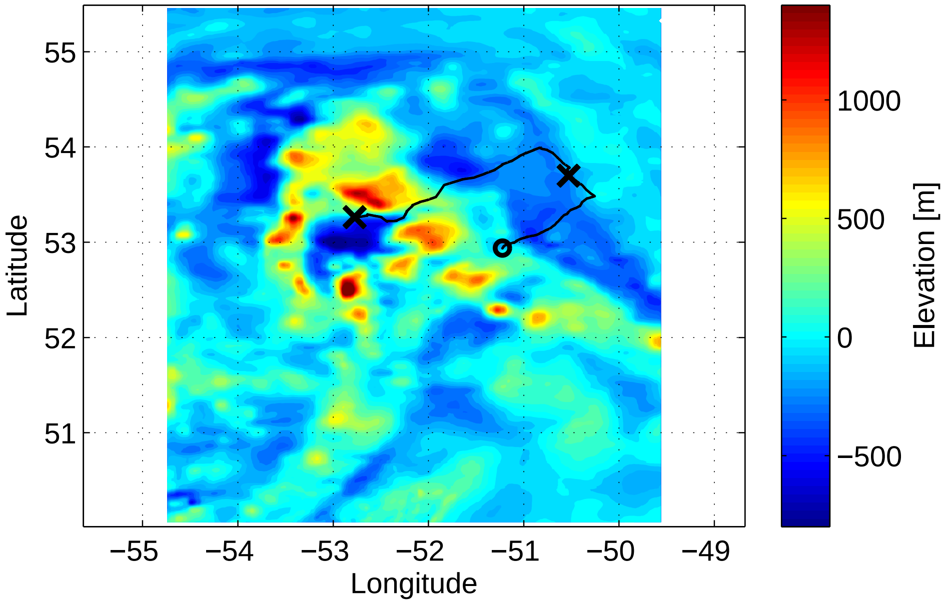

Figure 6.5: Locations of the calibration runs, indicated by the x's, shown against magnetic anomaly values in nanoteslas from the North American magnetic anomaly map [10]. The trajectory of the glider is shown as a black line with the starting location indicated by a circle.

by the local field at the calibration location, an RMS error of 56 nT is achieved. Prior to calibration the magnetic signal had an RMS error of 8437 nT. The magnitude of the raw magnetic signal compared to the calibrated signal for each of the calibration runs is shown in Fig. 6.7.

The global fit was then locally optimized using an iterative search algorithm on the scaling and translation parameters. The diving and climbing data were separated due to the different location of the mass shifting and ballast mechanism resulting in the calibration parameters and their respective calibration errors shown in Table 6.2.

The calibrated magnetic data from the diving and climbing spirals against the IGRF are shown in Fig. 6.8. The global calibrations result in a poor fit to the local field as is expected due to the different locations of the ballast and battery shifting mechanisms. During the first calibration run, the separate diving and climbing cali-

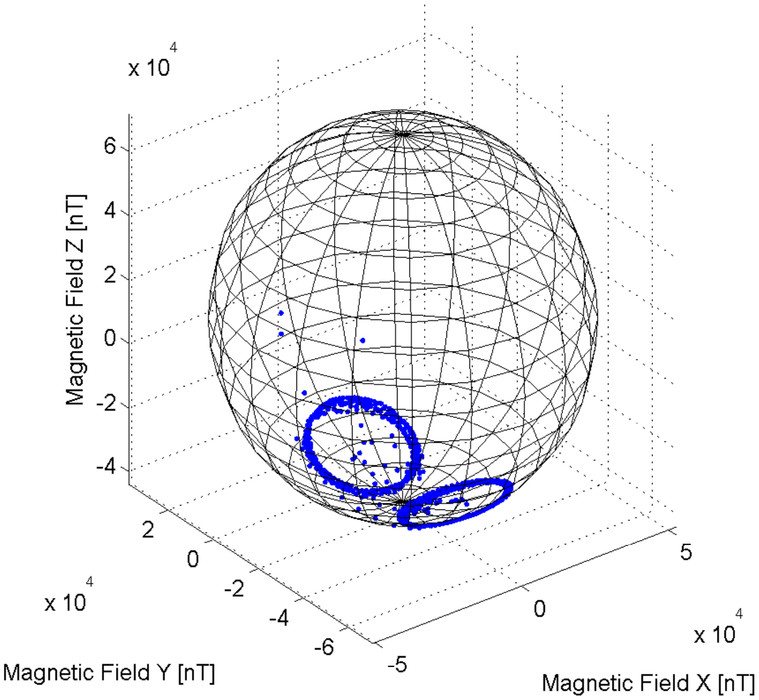

Figure 6.6: Raw magnetic data from the clockwise and counterclockwise calibration runs over the global calibration ellipsoid

brations result in a nice fit to the local field. The second calibration run performed profiles to depths of 200 meters instead of the 100 meters in the first. This increased depth resulted in a larger horizontal distance being travelled by the vehicle. When combined with the higher magnetic anomalies in the region, the second calibration showed poor fit to the local field. To mitigate this effect the second calibration set was limited to a single revolution from the diving and the climbing data resulting in a significantly improved RMS error.

Each of the locally optimized fits were then used to correct the magnetic data gathered during the entire glider deployment. The magnitudes of the corrected and uncorrected data using each set of calibration coefficients are shown in Fig. 6.9-6.10. Alternatively, the calibrated magnetic values are shown against the magnetic anomaly

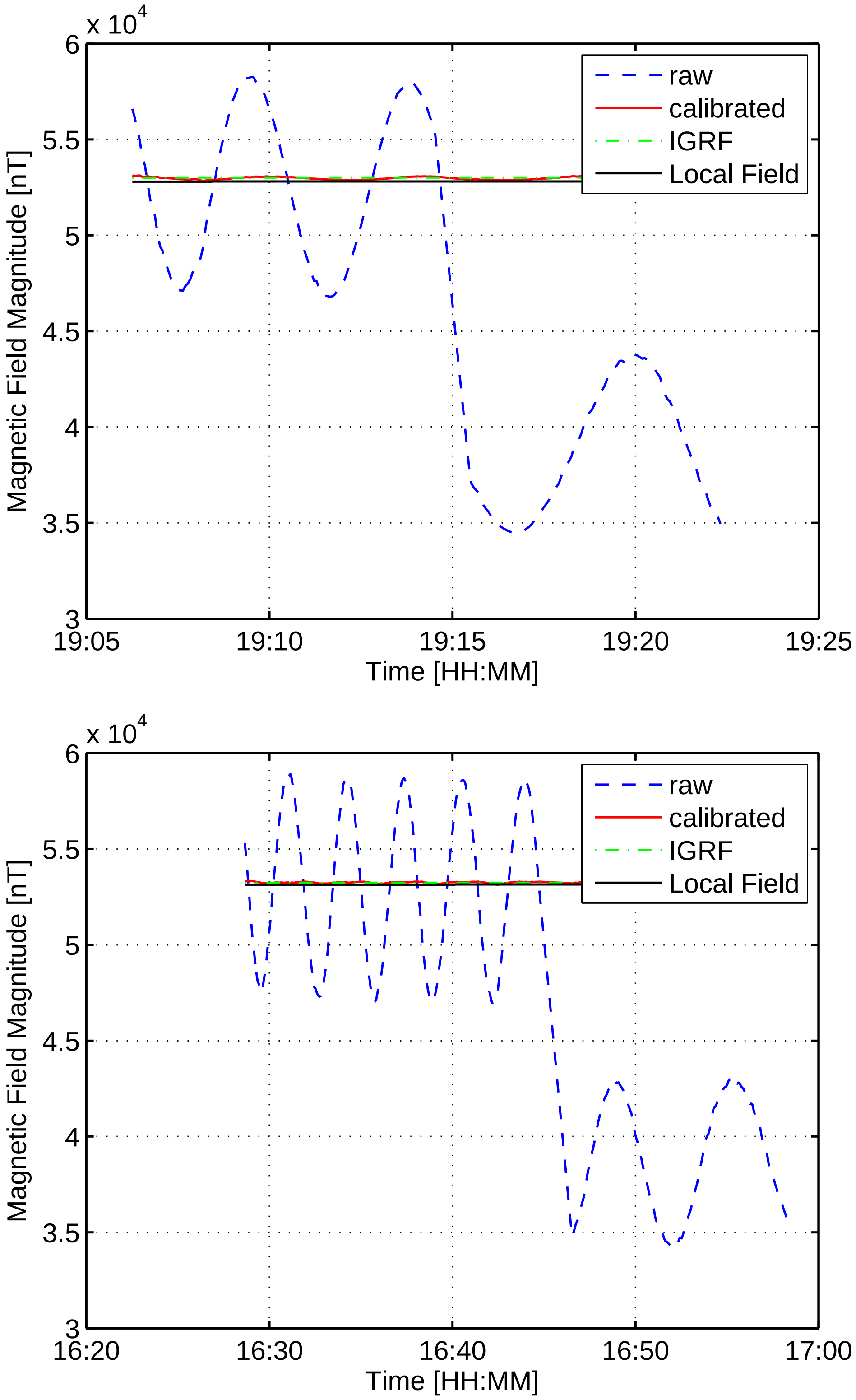

Figure 6.7: Magnitude of the global calibration spirals before and after calibration shown against the IGRF and the local field values for the Labrador Sea field trials for the first (top) and second (bottom) calibration where the local field is the IGRF plus the magnetic anomaly values from the North American magnetic anomaly map.

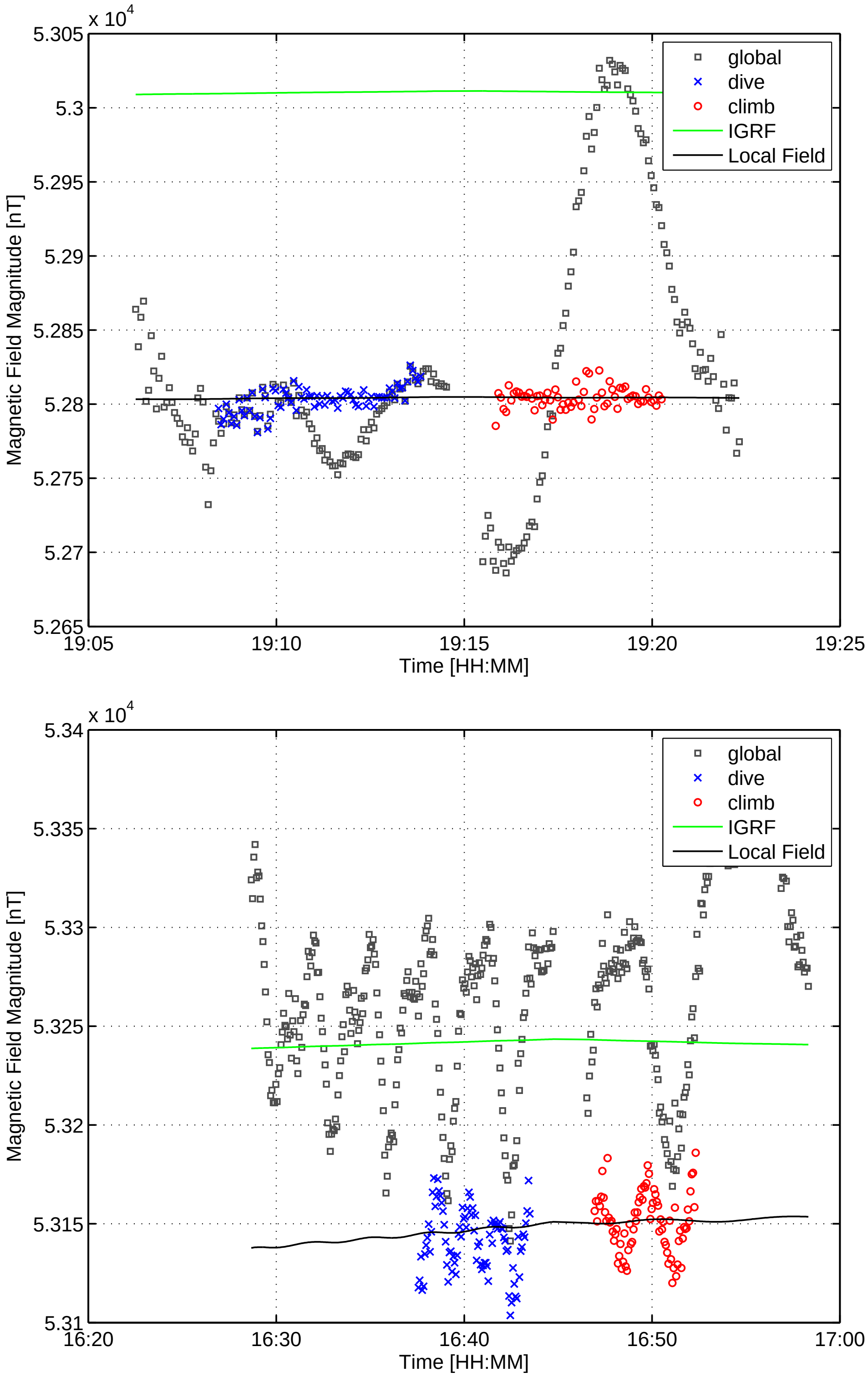

Figure 6.8: Magnitude of the diving and climbing calibration data calibrated using the locally optimized fits shown against the IGRF and local field values for the first (top) and second (bottom) calibration. The global fit is shown for reference.

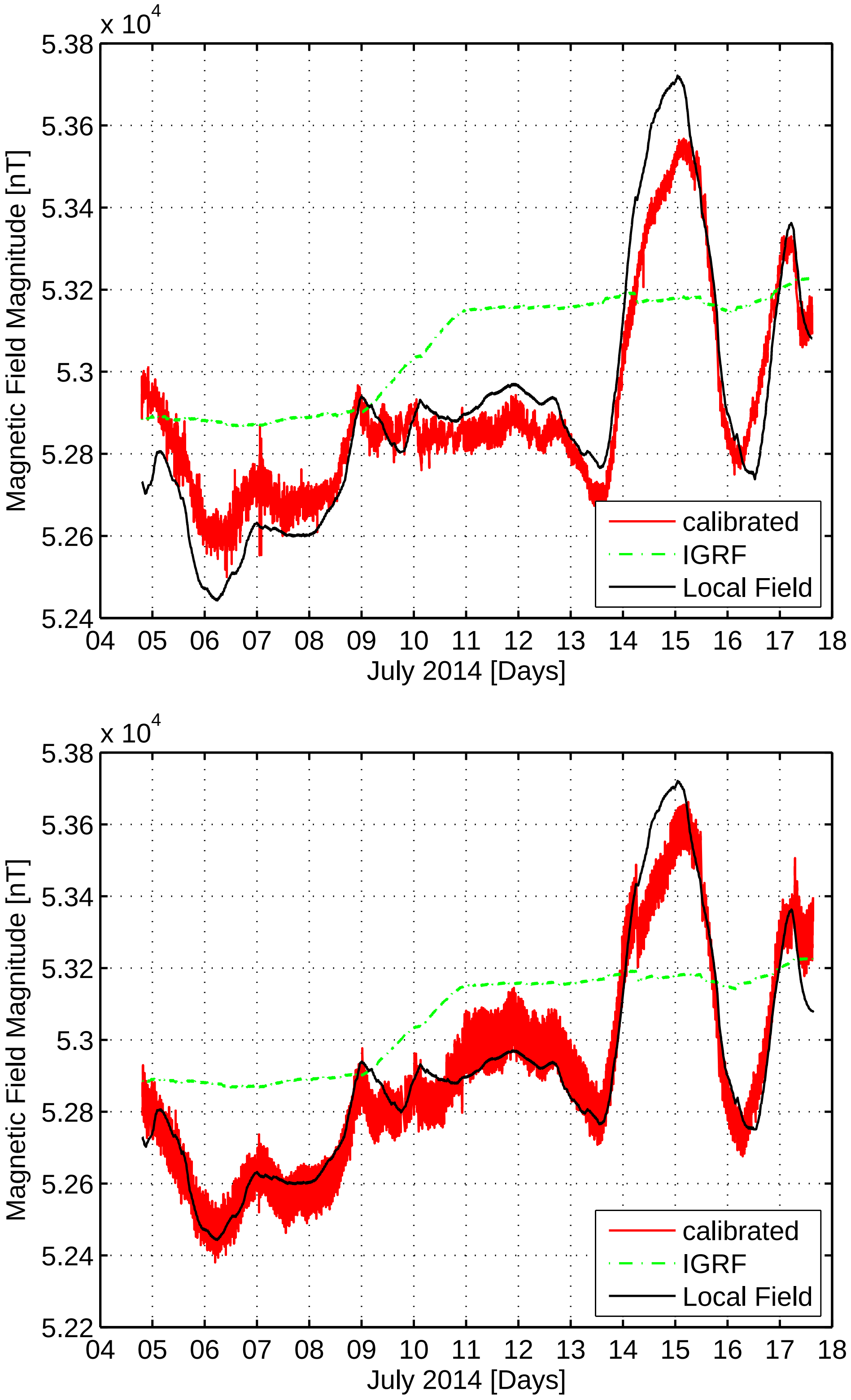

Figure 6.9: Magnitude of the calibrated and raw magnetic data collected in the Labrador Sea shown against the IGRF and local field values using the diving (top) and climbing (bottom) coefficients from the first trial

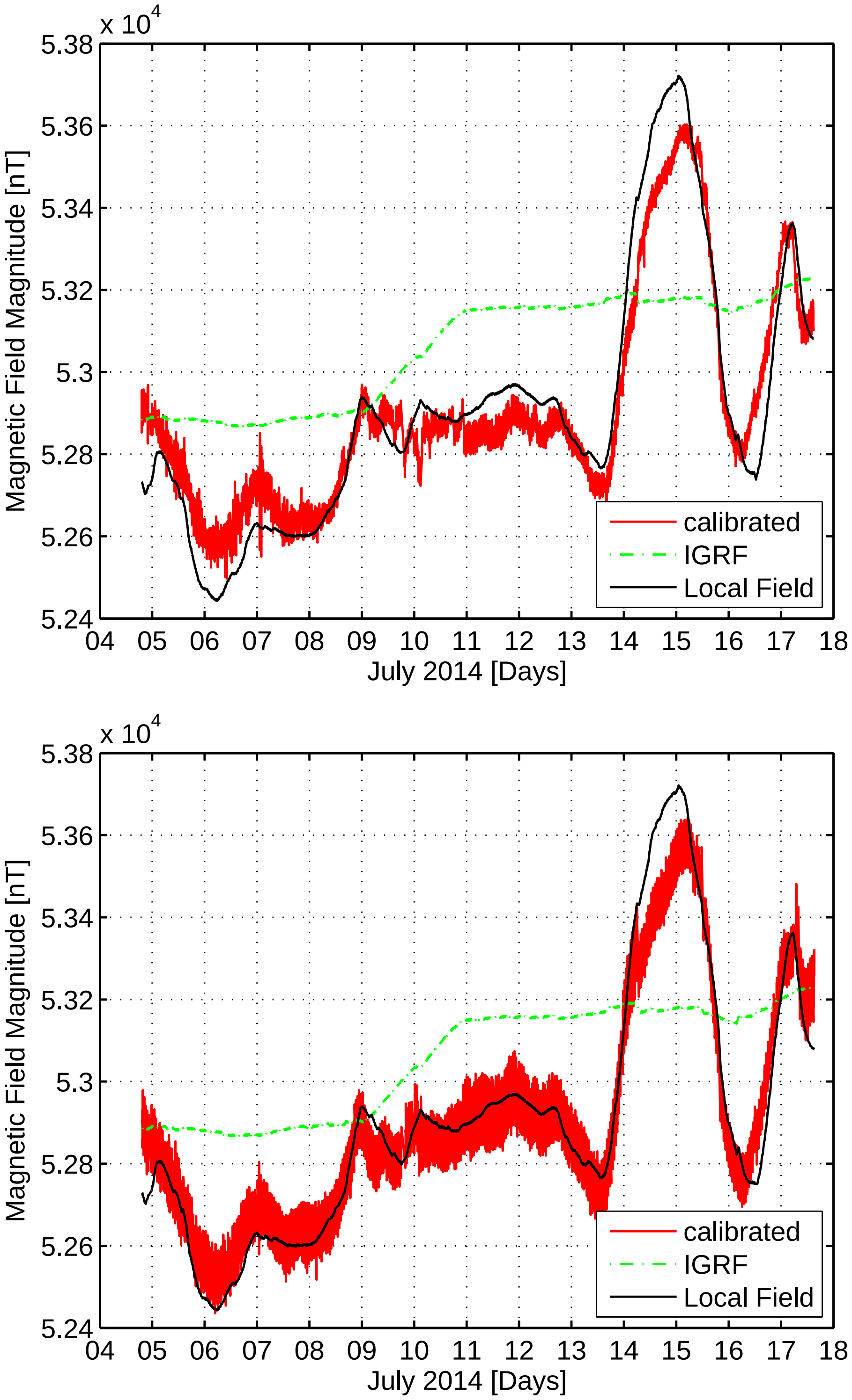

Figure 6.10: Magnitude of the calibrated and raw magnetic data collected in the Labrador Sea shown against the IGRF and local field values using the diving (top) and climbing (bottom) coefficients from the second trial

Table 6.2: Calibration coefficients and their respective errors for the global, diving and climbing calibrations from the first and second calibration runs in the Labrador Sea fixed parameter trials

| Trial | Translate X [nT] | Translate Y [nT] | Translate Z [nT] | Scaling X [nT] | Scaling Y [nT] | Scaling Z [nT] | RMSe [nT] |
|---|---|---|---|---|---|---|---|
| 1-global | 771 | -16763 | 14367 | 51777 | 54296 | 57385 | 56 |
| 2-global | 983 | -16652 | 13832 | 51547 | 54351 | 57358 | 57.5 |
| 1-dive | 729 | -16834 | 14416 | 51970 | 54392 | 57385 | 6.2 |
| 1-climb | 1179 | -16476 | 14270 | 51719 | 53481 | 57383 | 5.1 |
| 2-dive | 904 | -16841 | 13982 | 51983 | 54289 | 57385 | 10.3 |
| 2-climb | 996 | -16092 | 13815 | 51895 | 53350 | 57385 | 9.3 |

grid from the North American Magnetic Anomaly map are shown in Fig. 6.11.

The calibrated magnetic values measured by the underwater glider show a general agreement with the values from the North American magnetic anomaly grid [10]. The measured values have significant high frequency components that are filtered out of the North American grid as well as regional discrepancies. The RMS errors between the magnetic anomaly map and the measured values are shown in Table 6.3. Both of the calibration runs correct the data to a similar level of error, however, the diving coefficients leave a higher level of noise in the data which is strongly correlated with the vehicle's depth and pitch.

Table 6.3: The RMS errors between the magnetic anomaly map values and the calibrated measurements using the first and second set of diving and climbing calibration coefficients during the Labrador Sea fixed parameter trials.

| Trial | Diving | Climbing |
|---|---|---|
| First | 90.4 nT | 66.4 nT |
| Second | 74.9 nT | 61.5 nT |

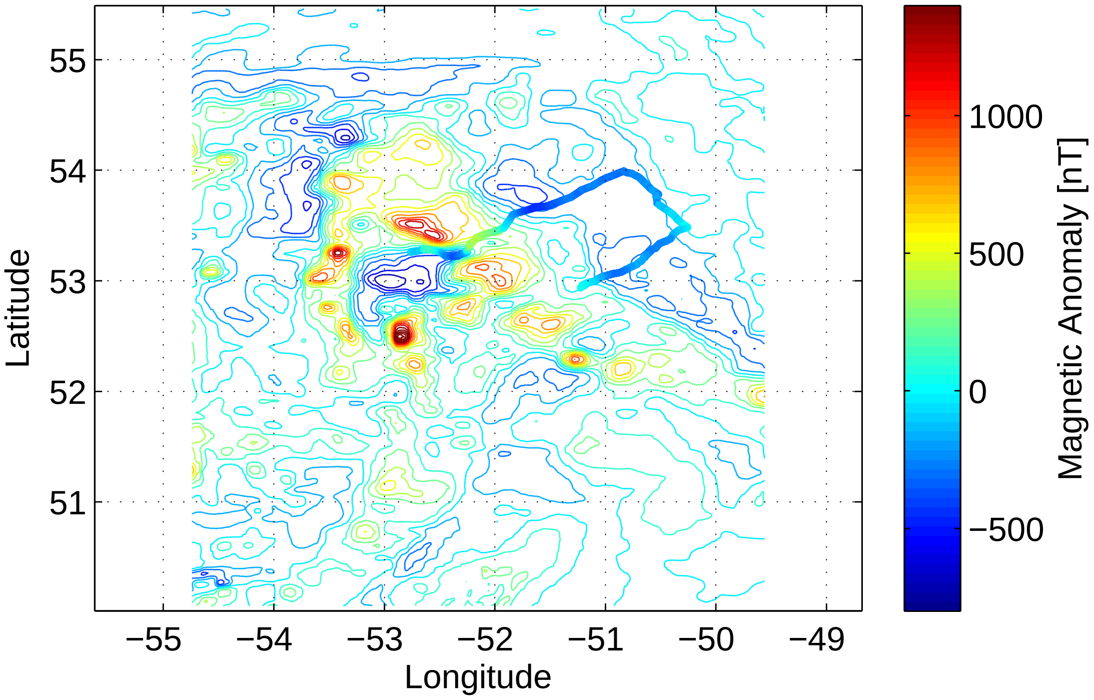

Figure 6.11: Labrador Sea magnetic anomaly data measured from an underwater glider calibrated using the second set of fixed parameter calibration coefficients shown against the magnetic anomaly values in nanoteslas from the magnetic anomaly map of North America [10]. Values calibrated with the first set of values are indistinguishable in this format and are therefore not presented.

### 6.3.2 Parameterized Trials in Bonne Bay

Field trials to evaluate the performance of a parameterized magnetic calibration method were performed from December 9 to 13th, 2013 in the East Arm of Bonne Bay, Newfoundland. In these trials the underwater glider was launched from the small aluminum boat Freezy shown in Fig. 6.12 and after launch was controlled from the Bonne Bay Marine Station. During the deployment there were light winds and the air temperature was around - 10 degrees Celsius. Recovery of the vehicle was originally planned for December 12th but had to be delayed due to strong winds. The vehicle was left to loiter in the lee of the head on Norris Point until a lull in the winds on the 13th allowed the recovery of the vehicle.

Figure 6.12: The Bonne Bay Marine Station's boat Freezy shown with the Slocum autonomous underwater glider during the parameterized trials in December 2013.

After the deployment, a series of clockwise calibration spirals were performed with the vehicle commanded to set the movable battery once during each ascent or descent to achieve a certain pitch according to a look up table. In this way five different battery locations were tested for two different ballast conditions. The ballast is also set to a single value once for each ascent or descent. Each calibration run therefore consists of a single spiralling descent and ascent with the ballast and battery at a fixed location and takes around 30 minutes to complete. Another full calibration procedure was repeated prior to recovery. The calibration runs are summarized in Table 6.4.

Table 6.4: Calibration runs for the parameterized magnetic calibration trials

| Run | Direction | Ballast [$cm^3$] | Pitch Command [deg] | Battery Locations Trial 1 [in] | Battery Locations Trial 2 [in] |
|---|---|---|---|---|---|
| 1 | Dive | -200 | -14 | 0.272 | 0.226 |
| 2 | Climb | 200 | 14 | -0.181 | -0.139 |
| 3 | Dive | -200 | -18 | 0.380 | 0.274 |
| 4 | Climb | 200 | 18 | -0.234 | -0.191 |
| 5 | Dive | -200 | -22 | 0.428 | 0.375 |
| 6 | Climb | 200 | 22 | -0.289 | -0.246 |
| 7 | Dive | -200 | -26 | 0.491 | 0.400 |
| 8 | Climb | 200 | 26 | -0.344 | -0.300 |
| 9 | Dive | -200 | -30 | 0.527 | 0.472 |
| 10 | Climb | 200 | 30 | -0.401 | -0.348 |

The vehicle was then flown in a criss-cross pattern down into the bay and back again with a commanded pitch of plus or minus 26 degrees and a commanded ballast of plus or minus 200 $cm^3$. The calibration locations along with the vehicle track-line are shown against the local magnetic anomalies in Fig. 6.13.

To provide reference measurements, aeromagnetic data overlapping the East Arm of Bonne Bay was used from the Newfoundland and Labrador Geoscience Atlas [48]. Unfortunately, the East Arm is split in half by the boundary of two different surveys,

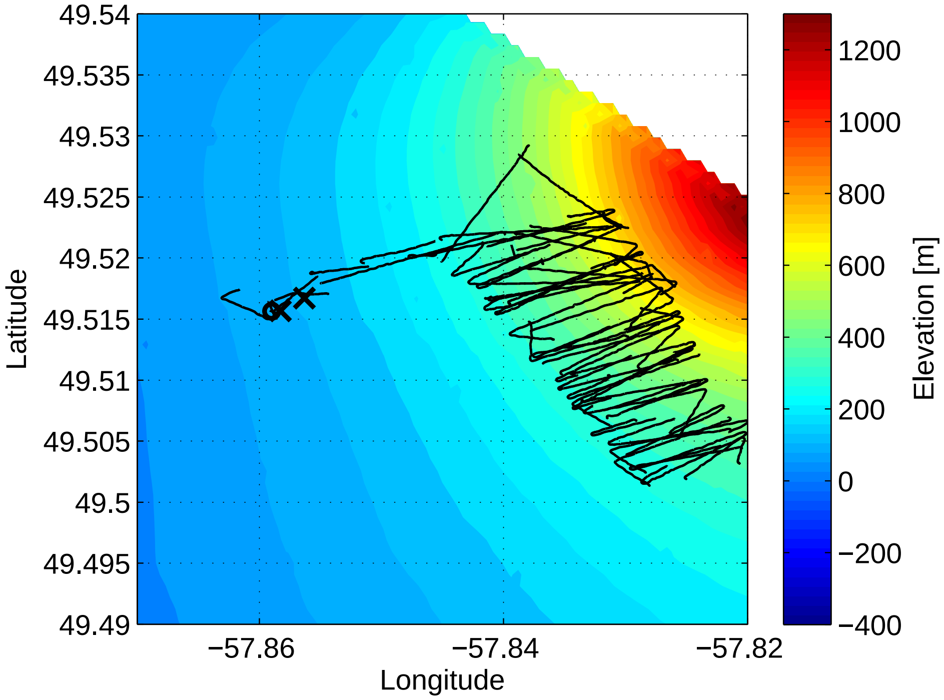

Figure 6.13: Calibration locations (x's) and the Bonne Bay Trials track-line (black line) starting from the circle and proceeding to crisscross south and then north in the East Arm of Bonne Bay. The magnetic anomaly grid of the Bonne Bay region is shown in the background.

the 2009 Corner Brook survey and the 2012 Offshore Western Newfoundland survey. To obtain a reference grid both magnetic anomaly grids were upward continued to a constant altitude of 90 meters. The grids were then combined, using the average value in the regions of overlap. A mask was applied to these larger grids to limit the region to the area of the East Arm of Bonne Bay. To smooth any discontinuities, 20 passes of a 3x3 Convolution (Hanning) filter was applied to remove the high frequency content introduced by combining the grids. The resulting grid is shown in Fig. 6.13.

For the parameterized calibration method, an initial global fit was performed by using the full set of raw measurements from each of the calibration runs. To constrain the ellipsoid in this initial fit it was necessary to make the x and z scaling values equal as there are no calibration measurements in the "northern hemisphere." Additionally, the ellipsoid was constrained in rotation such that $\mathbf{M} = \mathbf{I}$. The global fit was then locally optimized using an iterative search algorithm on the scaling and translation parameters to minimize the error between the magnitude of the calibration measurements and the local field. In this optimization scheme the local field was computed from the IGRF model and the magnetic anomaly values at the calibration location, altitude and time. The resulting magnitude of the global calibrated measurements are shown in Fig. 6.14

The global fit results in a root mean square error between the total field estimate from the IGRF and aeromagnetic data and the calibrated data of 153 nT and 145 nT for the first and second set of calibration runs. To compensate for the different locations of the battery and ballast mechanism the global fit is used as the initial conditions for the local optimization scheme on each run for each set.

A further local optimization on the polynomial coefficients was run to obtain the final set of calibration parameters of the form of Eqn. 6.5. The optimized calibration coefficients are then fit in a least squares sense to a fourth order polynomial as shown for the first set of calibration runs in Fig. 6.15 and the second set of calibration runs in Fig. 6.16.

The resulting magnitude of the calibration measurements, corrected with the parameterized coefficients are shown in Fig. 6.17. The optimized parameterized fit results in a root mean square error between the total field estimate from the IGRF and aeromagnetic data and the calibrated data of 38 nT and 31 nT for the first and second calibration trials. Each of these fits is then used to correct the magnetic data gathered during the remainder of the deployment as shown in Fig. 6.18.

The calibrated magnetic measurements gathered by the glider may then be compared to the magnetic anomaly values. The resulting interpolated values have a constant bias when compared to the glider magnetic data. Additionally, the glider

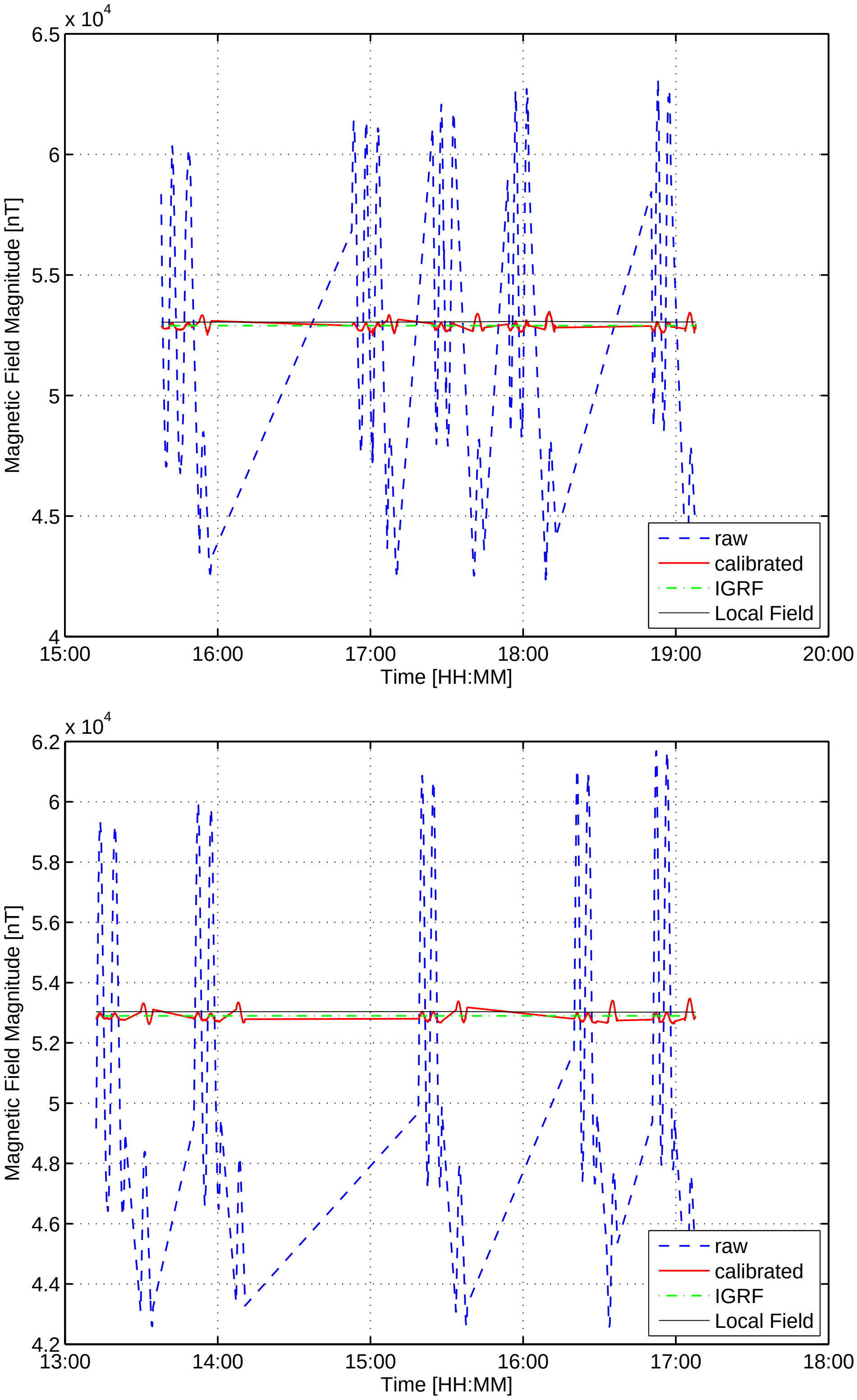

Figure 6.14: Magnitude of the magnetic data from the global calibration fit before and after calibration shown against the IGRF values for the Bonne Bay field trials using the first (top) and second (bottom) set of calibration coefficients

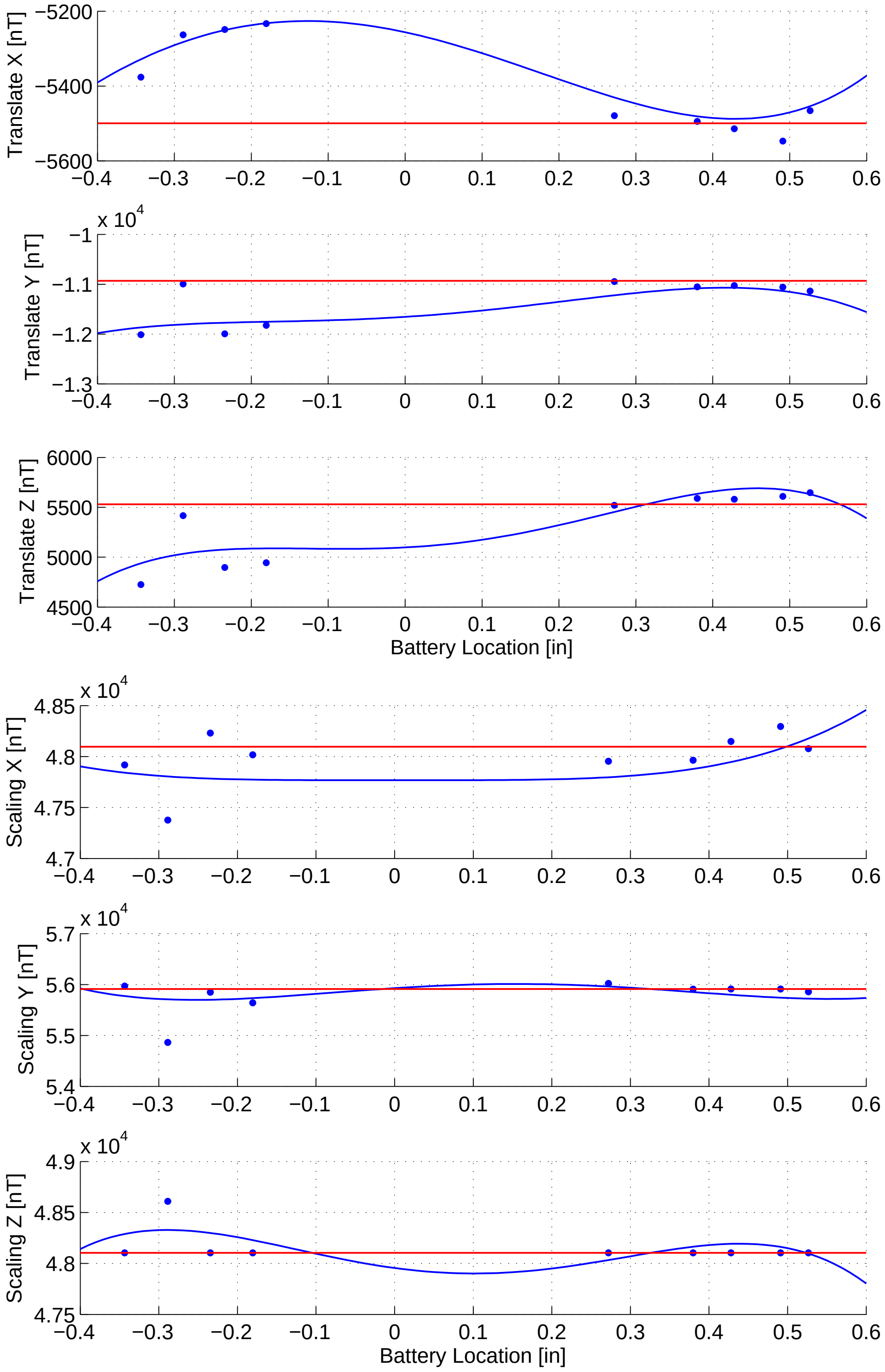

Figure 6.15: Translation (top) and scaling (bottom) calibration coefficients from the first set of calibration runs showing the optimized fourth order polynomials (blue lines) which are parameterized across the battery locations for both the diving and climbing ballast locations. The values of the coefficients from the initial global fits are shown as red lines.

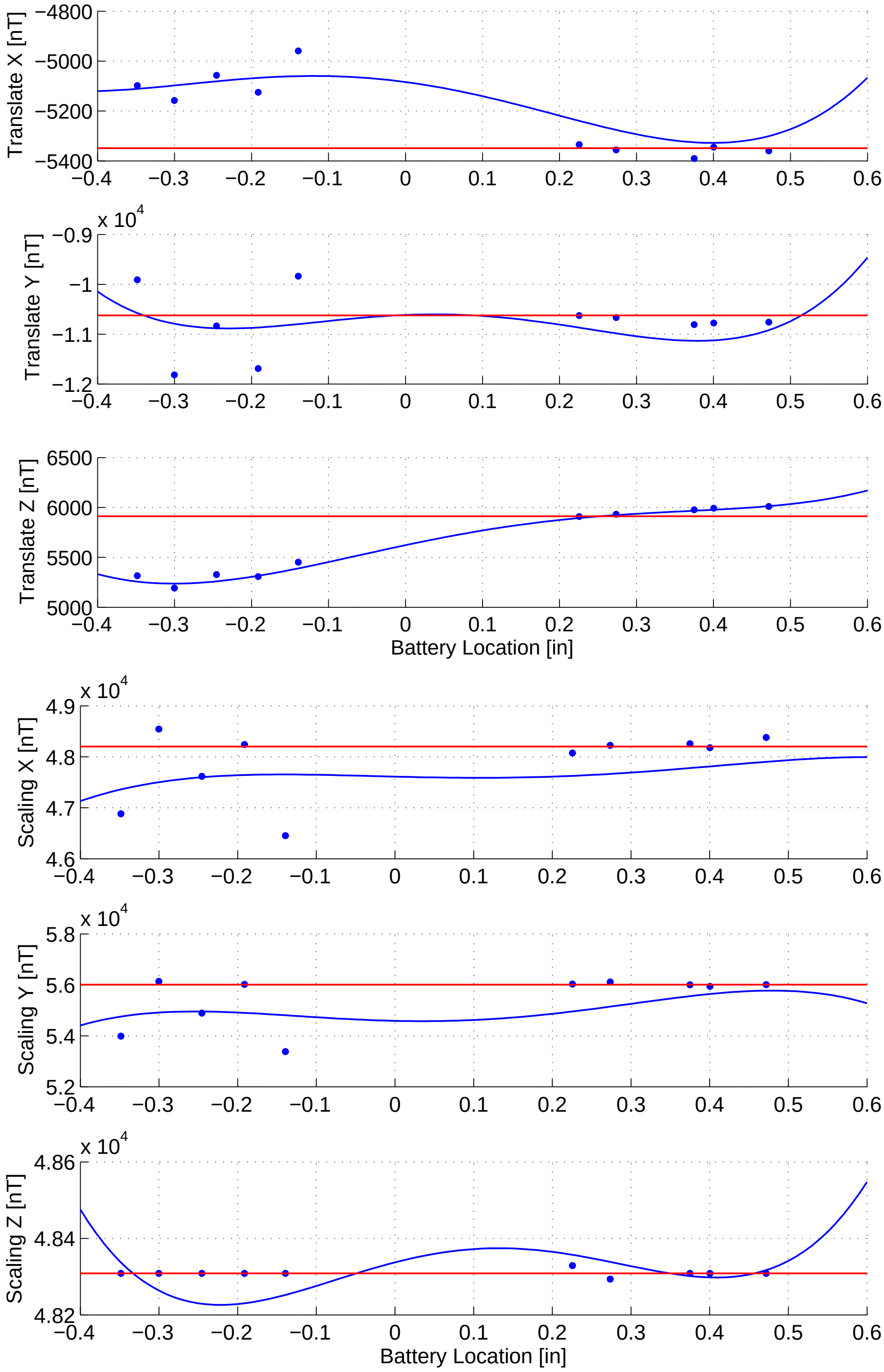

Figure 6.16: Translation (top) and scaling (bottom) calibration coefficients from the second set of calibration runs showing the optimized fourth order polynomials (blue lines) which are parameterized across the battery locations for both the diving and climbing ballast locations. The values of the coefficients from the initial global fits are shown as red lines.

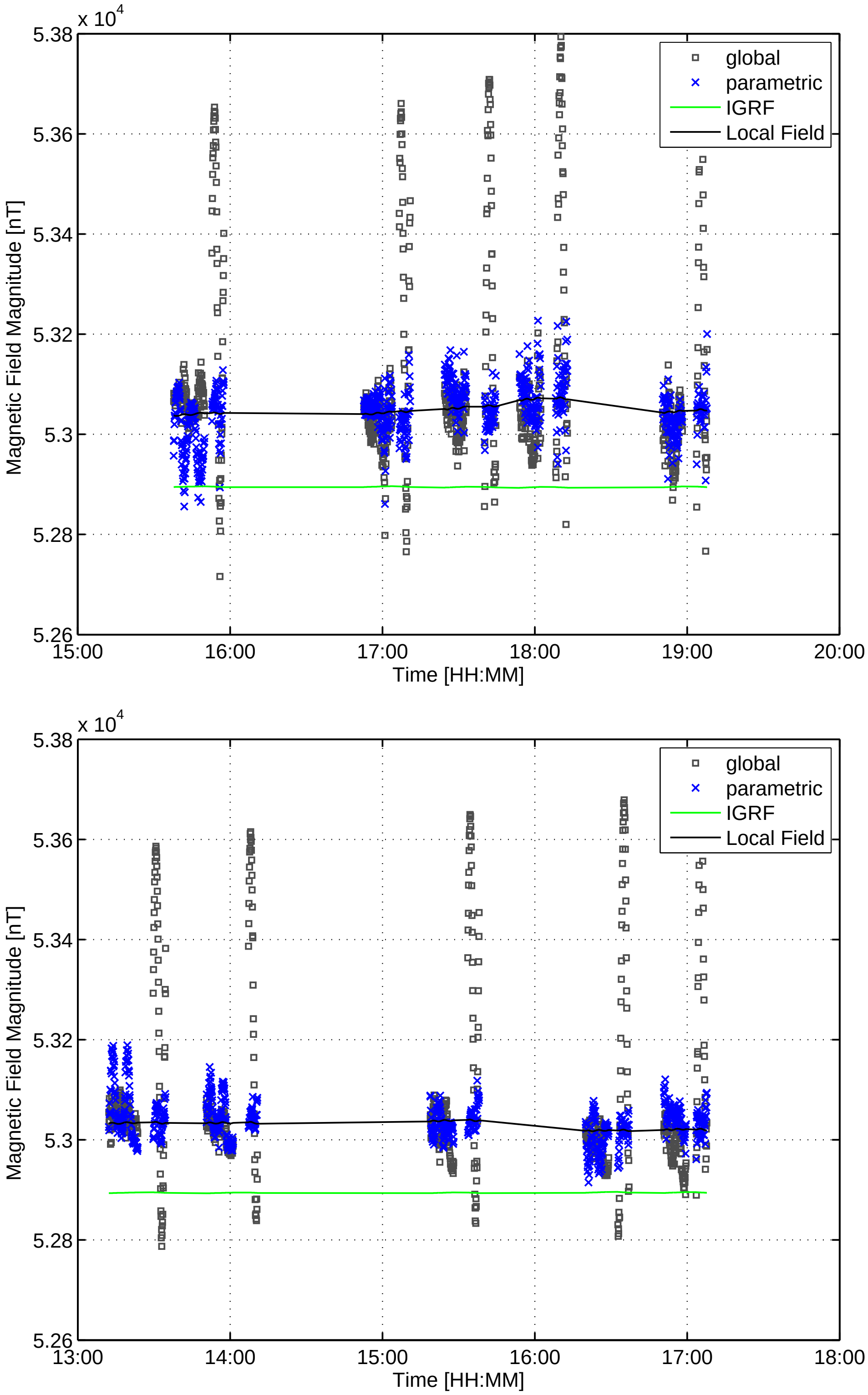

Figure 6.17: Magnitude of the diving and climbing calibration data calibrated using the parameterized fits from the first (top) and second (bottom) set of trials shown against the IGRF and local field values for the Bonne Bay trials

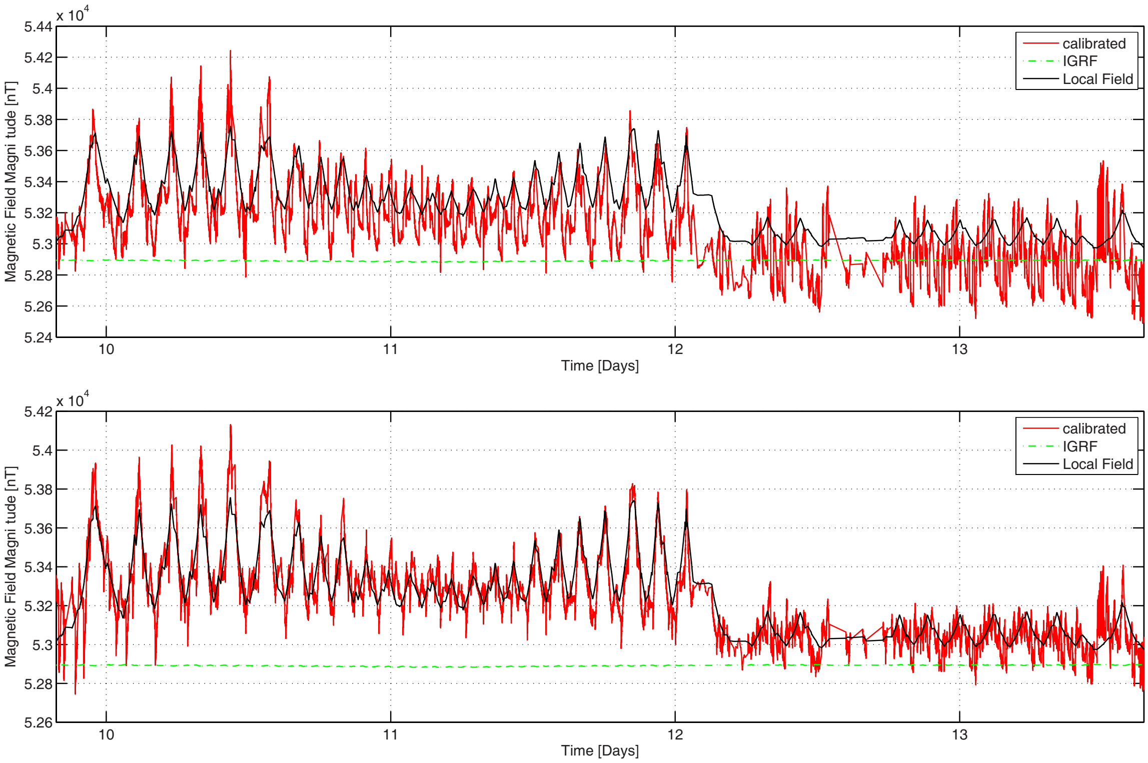

Figure 6.18: Magnetic data collected during the Bonne Bay deployment in December 2013 shown against the IGRF and local field values calibrated using the first (top) and second (bottom) set of parameterized calibration coefficients

data contains significantly more high frequency components than the aeromagnetic grids. These differences are attributed to the aeromagnetic data being collected at a higher altitude reducing the high frequency signatures present in the reference data as well as the significant low-pass filter applied during the gridding operations. The magnitude of the interpolated aeromagnetic data is shown against the glider magnetic data with the bias removed in Fig. 6.19

The first set of parameterized calibration coefficients perform well only for a short period of time. After the first day or so of measurements, there is a significant bias present in the measured values when compared to the local field. The second set of parameterized calibration coefficients does not display this change in bias, remaining

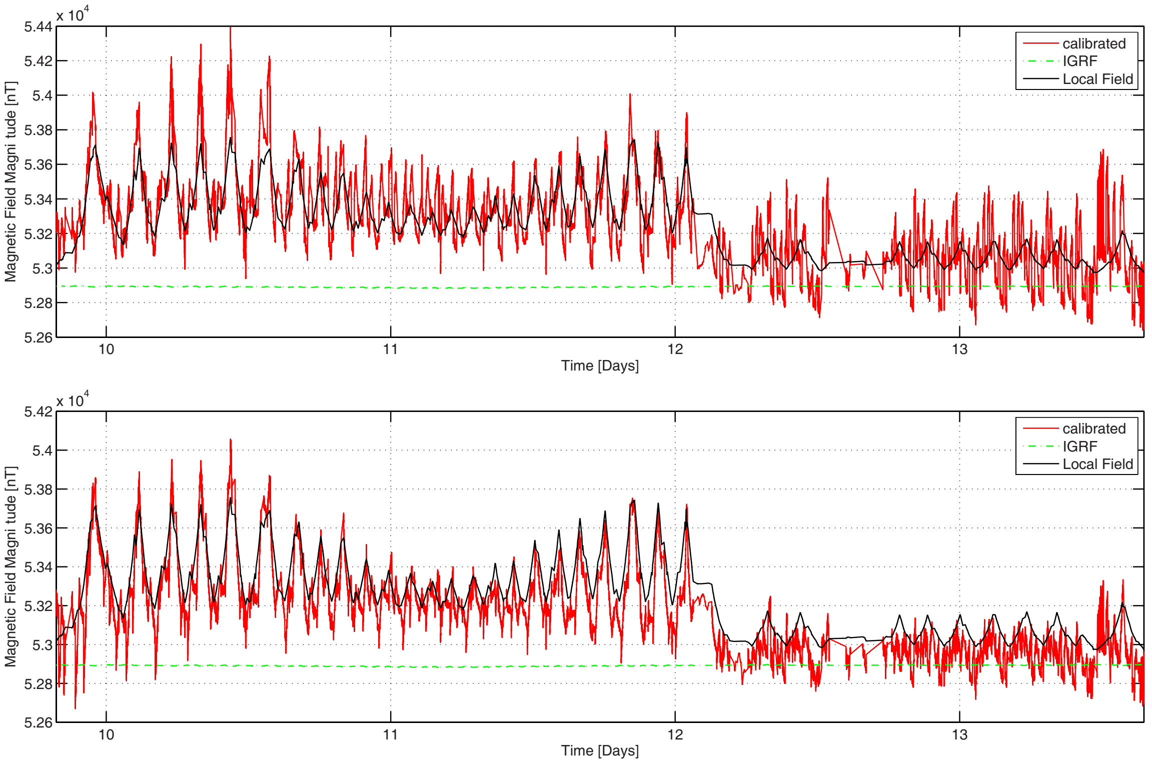

Figure 6.19: The glider magnetic data from the December 2013 Bonne Bay trials with the bias removed and calibrated with the first (top) and second (bottom) set of calibration coefficients. The IGRF and local field data is shown for reference.

consistently around the level of the local field. This difference is thought to be due to the temperature dependence of the sensor. The first calibration run was performed immediately after launch while the vehicle had been at a temperature of less than -10 degrees Celsius. The second calibration run was performed after the data collection before retrieval allowing the sensor adequate time to warm up. For this reason the measurements calibrated using the second set of parameterized coefficients were deemed more accurate. The measured magnetic anomaly data calibrated using the second set of parameterized calibration coefficients is in reasonable agreement with the magnetic anomaly data from the aeromagnetic surveys with RMS errors indicated in Table 6.5. This agreement indicates that the parameterized calibration method is

Table 6.5: The RMS errors between the magnetic anomaly map values and the calibrated measurements using the first and second set of diving and climbing calibration coefficients during the Bonne Bay parameterized calibration trials.

| Trial | |
|---|---|
| First | 123 nT |
| Second | 120 nT |

effective for calibration of magnetic measurements performed from a vehicle with moving masses. The drawbacks of this method are the increased number of calibration runs that need to be performed over the fixed parameter calibration method. However, the local optimization of the parameterized fits is constrained to a higher degree than the local optimizations performed on the diving and climbing calibrations from the fixed parameter trials. This increased constraint helps to mitigate some of the correlation with depth observed in the fixed parameter trials. Thus, while the parameterized calibration method takes longer to perform, it covers the calibration space more completely, resulting in a better calibration.

Magnetic measurements performed in this manner are suited to the online calibration of magnetic data. This online correction is the ultimate goal towards allowing the augmentation of terrain relative navigation methods with magnetic anomaly measurements. This chapter has further motivated this transition by presenting two calibration methods suited to use with measurements collected by an underwater glider and comparing these measurements to digital models. The calibration results compare favorably with the existing digital magnetic models supporting future research into magnetically aided navigation techniques.

# Chapter 7

# Summary

Persistent navigation of autonomous underwater gliders is subject to significant limitations in the mid-water zone and during long transects without surface access. Presently available solutions for persistent navigation of autonomous underwater vehicles either require too much energy or are subject to error accumulation which make them untenable over long durations.

In this work, the control of an underwater glider in the vertical plane, or depth control, is separated from the horizontal control. Long duration deployments of underwater vehicles which are not neutrally buoyant suffer additional energy loss due to lift induced drag. Hybrid underwater gliders using the propeller for extended horizontal flight modes can lose several percent of their potential range to this lift induced drag. This range loss is accentuated due to the vehicle's constant power control strategy where an increase in drag reduces the vehicle's forward velocity. As the velocity decreases the lift of the vehicle becomes lower compounding these effects and requiring more energy than a control scheme which attempts to maintain a constant velocity. For underwater gliders there is a threshold of around 0.3 m/s above which these effects are minimized.

A new depth controller for a hybrid underwater glider has been developed based on an integral state feedback control law. The gains for the controller are computed using an energy optimal method based on an augmentation of a linear quadratic regulator. The second order linear time invariant model coefficients for the computation of the gains are obtained through an iterative prediction-error minimization method. The system identification data was collected by commanding the vehicle to perform a series of thruster assisted profiles, one for identification and one for verification. The identified model showed sufficient agreement with both data sets for the steady state portion of the profiles, with higher errors during the inflections.

The computed gains were used to control the hybrid underwater glider to a constant depth. For these trials the vehicle showed its ability to adjust the ballast slowly to compensate for the excess buoyancy. Additionally, the step response of the vehicle had zero overshoot, a key consideration for avoiding the seafloor, and maintained its depth to within plus or minus 0.5 meters. The energy lost to the control commands and lift induced drag for this mission was around one percent over the 20 minute deployment. However, as the pitch of the vehicle had not settled to zero this value is expected to decrease for a longer deployment due to the reduced influence of the lift induced drag.

For the horizontal navigation of an underwater glider, a terrain aided navigation (TAN) algorithm has been presented based on a particle filter known as the jittered bootstrap filter. The glider TAN algorithm allows for location estimates to be computed through comparisons of the water depth estimate measured by the vehicle with a digital parameter model (DPM) of the bathymetry. The method makes use of the underwater glider's altimeter, pressure sensor, dead-reckoning solution and attitude. The algorithm has been shown to be suitable for post processing of underwater glider data collected in water depths which allow for altimeter measurements but in which

GPS updates are denied. Additionally, the method was validated through online trials in which a more powerful single board computer was integrated to run the filter.

The method was evaluated through two sets of offline field trials which took place in October 2010 and 2012 in Holyrood Arm of Conception Bay, Newfoundland. During these trials the underwater glider was allowed to obtain GPS updates during its periodic surfacings to provide a benchmark to compare to the glider TAN location estimates. The data collected during these trials was then used to compute location estimates using the glider TAN algorithm which uses the first pre-dive GPS location for initialization. The algorithm's performance was evaluated for a range of values of the jittering variance, the DPM grid cell size and the number of particles. It was found that the algorithm finds good convergence for a jittering variance of 15 $m^2$, 1000 particles and for DPM grid cell sizes ranging from the base grid cell size of 2 meters up to a cell size of 100 meters.

Using nominal values for the jittering variance, number of particles and the base grid cell size, 100 Monte Carlo simulations were run to confirm the convergence at those values. In both the 2010 and 2012 trials the algorithm maintained its convergence for all 100 runs. During the runs for the 2010 trials the peak error was 96 meters and the RMS error was 33 meters. The total distance traversed over the DPM was approximately 9 kilometers and the error before the vehicle left the bounds of the DPM was 44 meters compared to the dead-reckoned error of 900 meters. During the runs for the 2012 trials the peak error was 532 meters and the RMS error was 50 meters. The total distance travelled by the vehicle was approximately 91 kilometers and the error at the end of the mission was 16 meters, compared with the dead-reckoned error of 5.5 kilometers. The peak error of 532 meters during the 2012 trials was found to correspond to a period of shallow water profiles near shore and was attributed to an increase in the dead-reckoning error rate. These trials show the glider TAN algorithm's utility in post processing bounded location estimates of glider data in surface denied regions.

Online open loop trials were performed in September of 2014 in Holyrood Arm in which independent, hour long northward and southward tests were run. For these trials a Beagle Bone Black (BBB) single board computer was integrated into the payload bay of the underwater glider. The BBB runs the filter, programmed in C/C++, in around 10 ms while consuming just over 0.5 W on average. During the northward and southward legs of the online trials the RMS errors were 76 and 32 meters respectively. The larger error in the northward leg was attributed to the large dead-reckoned error growth rate of 25.6 percent of distance traveled. In both cases the glider TAN estimates provided bounded error location estimates which improved on the dead-reckoned estimates in spite of the short duration of the tests and larger than normal dead-reckoning error growth rate.

While TAN provides a powerful tool for navigation in regions without surface access it suffers from poor performance when the terrain is flat or beyond the range of the sensor. Magnetic measurements have been proposed previously to augment a terrain relative navigation scheme in such regions to help constrain the location estimates. To date, this capability has yet to be realized on a physical system due to challenges in magnetic sensor calibration and the lack of suitable magnetic maps. To further this goal, an underwater glider magnetic instrumentation suite has been developed. Additionally, two calibration methods have been developed and verified through field trials which are suited to correcting magnetic measurements gathered by an underwater glider.

The first method assumes the vehicle's actuators remain in a fixed location. A single set of calibration coefficients may be computed from calibration spirals performed during the field trials. In this case, the vehicle is commanded to perform a series of initial profiles to determine the steady state locations of the vehicle's actuators. A series of spiralling profiles was then performed using these steady state values and the calibration parameters extracted. This calibration method was verified through field trials in the Labrador Sea in June and July of 2014. In these trials the vehicle traversed approximately 250 kilometers over the course of 13 days. The corrected measurements were compared to the Magnetic Map of North America and found to match the low frequency content well with a mean RMS error of around 75 nanoteslas against a peak to peak magnetic anomaly signal of around 1200 nanoteslas.

The second method attempts to parameterize the calibration coefficients based on the locations of the vehicle's actuators. To accomplish this, spiralling profiles using a set of 5 different battery shifting locations are performed. Calibration coefficients may then be computed for each of the different battery and ballast locations. A fourth order polynomial was fit to these calibration coefficients such that a set of calibration coefficients may be determined for a measured battery location. These polynomial fits were optimized using a gradient descent local optimizer. This calibration method was then verified through field trials in the East Arm of Bonne Bay, Newfoundland in December of 2013. The corrected magnetic anomaly measurements were compared to a local magnetic anomaly model which were collected through an aeromagnetic survey. The low frequency content from the underwater glider magnetic measurements was found to agree well with the gridded aeromagnetic data with a mean RMS error of 120 nanoteslas against a peak to peak magnetic anomaly signal of around 1400 nanoteslas. The larger error present in the parameterized method data over the fixed parameter method data is attributed to the different locations of the tests. These magnetic measurement methods for an underwater glider show promise towards online magnetic augmentation of a terrain aided navigation method.

The primary contributions of this thesis are summarized as an energy optimal depth control method; a terrain aided navigation method and a magnetic instrumentation system and calibration method for an autonomous underwater glider. Future work in this area includes the online closed loop trials of the terrain aided navigation for an underwater glider. Additionally, an evaluation of the terrain aided navigation methods using the available global bathymetric digital parameter models for the Labrador Shelf and Sea is needed.

# Bibliography

[1] B. Claus and R. Bachmayer, "Towards navigation of underwater gliders in seasonal sea ice," in *Oceans 2014 - St. John's*, 2014.

[2] B. Claus, R. Bachmayer, and L. Cooney, "Analysis and development of a buoyancy-pitch based depth control algorithm for a hybrid underwater glider," in *Autonomous Underwater Vehicles (AUV), 2012 IEEE/OES*, pp. 1–6, IEEE, 2012.

[3] B. Claus and R. Bachmayer, "Development of a magnetometry system for an underwater glider," in *17th International Symposium on Unmanned Untethered Submersible Technology*, 2011.

[4] B. Claus and R. Bachmayer, "Terrain aided navigation for an underwater glider," *Journal of Field Robotics*, accepted.

[5] "Map of the 7 stations and 14 sections." `http://www.meds-sdmm.dfo-mpo.gc.ca/isdm-gdsi/azmp-pmza/map-carte-eng.html`. Accessed: 2014-10-15.

[6] W. B. F. Ryan, S. M. Carbotte, J. O. Coplan, S. O'Hara, A. Melkonian, R. Arko, R. A. Weissel, V. Ferrini, A. Goodwillie, F. Nitsche, J. Bonczkowski, and R. Zemsky, "Global multi-resolution topography synthesis," *Geochemistry, Geophysics, Geosystems*, vol. 10, no. 3, pp. n/a–n/a, 2009.

[7] Environment Canada, "Canadian Ice Service." online, Apr. 2014. http://www.ec.gc.ca/glaces-ice/.

[8] Sikumiut Environmental Management Ltd., "Labrador Shelf offshore area sea final report," Aug. 2008.

[9] F. Fetterer and C. Fowler, "National Ice Center Arctic sea ice charts and climatologies in gridded format," *National Snow and Ice Data Center, Boulder, CO, digital media.[Available online at http://nsidc. org/data/docs/noaa/g02172_nic_charts_ climo_grid/index. html.]*, 2006.

[10] V. Bankey, A. Cuevas, D. Daniels, C. A. Finn, I. Hernandez, P. Hill, R. Kucks, W. Miles, M. Pilkington, C. Roberts, W. Roest, V. Rystrom, S. Shearer, S. Snyder, R. Sweeney, J. Velez, J. D. Phillips, and D. Ravat, *Digital data grids for the magnetic anomaly map of North America.* US Geological Survey, 2002.

[11] O. Schofield, J. Kohut, D. Aragon, L. Creed, J. Graver, C. Haldeman, J. Kerfoot, H. Roarty, C. Jones, D. Webb, and S. Glenn, "Slocum gliders: Robust and ready," *Journal of Field Robotics*, vol. 24, no. 6, pp. 473–485, 2007.

[12] S. R. Rintoul, M. Sparrow, M. P. Meredith, V. Wadley, K. Speer, E. Hofmann, C. Summerhayes, E. Urban, R. Bellerby, S. Ackley, K. Alverson, I. Ansorge, S. Aoki, R. Azzolini, L. Beal, M. Belbeoch, A. Bergamasco, M. Biuw, L. Boehme, G. Budillon, L. Campos, D. Carlson, R. Cavanagh, E. Charpentier, H. C. Shin, M. Coffin, A. Constable, D. Costa, M. Cronin, H. D. Baar, C. D. Broyer, T. D. Bruin, L. D. Santis, E. Butler, P. Dexter, M. Drinkwater, M. England, E. Fahrbach, E. Fanta, M. Fedak, K. Finney, A. Fischer, R. Frew, S. Garzoli, H. Gernandt, S. Gladyshev, D. Gomis, A. Gordon, J. Gunn, J. Gutt, C. Haas, J. Hall, K. Heywood, K. Hill, M. Hindell, M. Hood, M. Hoppema,

G. Hosie, W. Howard, C. Joiris, L. Kaleschke, S.-H. Kang, M. Kennicutt, A. Klepikov, L. Lembke-Jene, N. Lovenduski, V. Lytle, P.-P. Mathieu, T. Moltmann, R. Morrow, M. Muelbert, E. Murphy, M. Naganobu, A. N. Garabato, S. Nicol, S. O'Farrell, N. Ott, A. Piola, S. Piotrowicz, R. Proctor, F. Qiao, F. Rack, R. Ravindra, K. Ridgway, E. Rignot, V. Ryabinin, E. Sarukhanian, S. Sathyendranath, P. Schlosser, J. Schwarz, G. Smith, S. Smith, C. Southwell, S. Speich, W. Stambach, D. Stammer, K. Stansfield, J. Thiede, E. Thouvenot, B. Tilbrook, P. Wadhams, I. Wainer, V. W. Puig, S. Wijffels, P. Woodworth, T. Worby, and S. Wright, *The Southern Ocean observing system: Initial science and implementation strategy.* SCAR and SCOR, 2012.

[13] K. R. Arrigo, D. K. Perovich, R. S. Pickart, Z. W. Brown, G. L. van Dijken, K. E. Lowry, M. M. Mills, M. A. Palmer, W. M. Balch, F. Bahr, *et al.*, "Massive phytoplankton blooms under Arctic sea ice," *Science*, vol. 336, no. 6087, pp. 1408–1408, 2012.

[14] K. R. Arrigo, D. K. Perovich, R. S. Pickart, Z. W. Brown, G. L. van Dijken, K. E. Lowry, M. M. Mills, M. A. Palmer, W. M. Balch, N. R. Bates, *et al.*, "Phytoplankton blooms beneath the sea ice in the Chukchi Sea," *Deep Sea Research Part II: Topical Studies in Oceanography*, 2014.

[15] D. L. Gautier, K. J. Bird, R. R. Charpentier, A. Grantz, D. W. Houseknecht, T. R. Klett, T. E. Moore, J. K. Pitman, C. J. Schenk, J. H. Schuenemeyer, *et al.*, "Assessment of undiscovered oil and gas in the Arctic," *Science*, vol. 324, no. 5931, pp. 1175–1179, 2009.

[16] L. C. Smith and S. R. Stephenson, "New Trans-Arctic shipping routes navigable by midcentury," *Proceedings of the National Academy of Sciences*, vol. 110,

no. 13, pp. E1191–E1195, 2013.

[17] S. R. Stephenson, L. C. Smith, L. W. Brigham, and J. A. Agnew, “Projected 21st-century changes to Arctic marine access,” *Climatic Change*, vol. 118, no. 3-4, pp. 885–899, 2013.

[18] J.-C. Therriault, *Proposal for a northwest Atlantic zonal monitoring program.* Fisheries & Oceans Canada, 1998.

[19] E. Colbourne, “The history of standard hydrographic sections in Newfoundland and Labrador,” *The Atlantic Zone Monitoring Program/Le Programme de Monitorage de la Zone Atlantique*, p. 29, 2004.

[20] J. Lazier and D. Wright, “Annual velocity variations in the Labrador Current,” *Journal of Physical Oceanography*, vol. 23, no. 4, pp. 659–678, 1993.

[21] J. C. Kinsey, R. M. Eustice, and L. L. Whitcomb, “A survey of underwater vehicle navigation: Recent advances and new challenges,” in *IFAC Conference of Manoeuvering and Control of Marine Craft*, (Lisbon, Portugal), September 2006. Invited paper.

[22] L. Stutters, H. Liu, C. Tiltman, and D. Brown, “Navigation technologies for autonomous underwater vehicles,” *Systems, Man, and Cybernetics, Part C: Applications and Reviews, IEEE Transactions on*, vol. 38, pp. 581 –589, July 2008.

[23] L. Paull, S. Saeedi, M. Seto, and H. Li, “AUV navigation and localization: A review,” *Oceanic Engineering, IEEE Journal of*, vol. 39, pp. 131–149, Jan 2014.

[24] C. M. Lee and J. I. Gobat, “Acoustic navigation and communication for high-latitude ocean research workshop,” *Eos, Transactions American Geophysical Union*, vol. 87, no. 27, pp. 268–268, 2006.

[25] L. Freitag, P. Koski, A. Morozov, S. Singh, and J. Partan, “Acoustic communications and navigation under arctic ice,” in *Oceans, 2012*, pp. 1–8, Oct 2012.

[26] C. Jones, A. Morozov, and J. Manley, “Under ice positioning and communications for unmanned vehicles,” in *OCEANS - Bergen, 2013 MTS/IEEE*, pp. 1–6, June 2013.

[27] S. Webster, C. Lee, and J. Gobat, “Preliminary results in under-ice acoustic navigation for seagliders in Davis Strait,” in *OCEANS 2014*, pp. 1 –5, Sept. 2014.

[28] I. Nygren, “Robust and efficient terrain navigation of underwater vehicles,” in *Position, Location and Navigation Symposium, 2008 IEEE/ION*, pp. 923 –932, May 2008.

[29] C. Morice, S. Veres, and S. McPhail, “Terrain referencing for autonomous navigation of underwater vehicles,” in *OCEANS 2009 - EUROPE*, pp. 1 –7, May 2009.

[30] D. Meduna, S. Rock, and R. McEwen, “Closed-loop terrain relative navigation for AUVs with non-inertial grade navigation sensors,” in *Autonomous Underwater Vehicles (AUV), 2010 IEEE/OES*, pp. 1 –8, Sept. 2010.

[31] L. Chen, S. Wang, K. McDonald-Maier, and H. Hu, “Towards autonomous localization and mapping of AUVs: a survey,” *International Journal of Intelligent Unmanned Systems*, vol. 1, no. 2, pp. 97–120, 2013.

[32] I. Nygren, *Terrain Navigation for Underwater Vehicles.* PhD thesis, KTH Electrical Engineering, Stockholm, Sweden, 2005.

[33] O. Bergem, *Bathymetric Navigation of Autonomous Underwater Vehicles Using a Multibeam Sonar and a Kalman Filter with Relative Measurement Covariance Matrices.* PhD thesis, University of Trondheim, 1993.

[34] D. Meduna, *Terrain relative navigation for sensor-limited systems with application to underwater vehicles.* Phd, Stanford University, 08/2011 2011.

[35] J. A. Richeson, *Gravity Gradiometer Aided Inertial Navigation within Non-GNSS Environments.* PhD thesis, University of Maryland, 2008.

[36] F. Teixeira, *Terrain-Aided Navigation and Geophysical Navigation of Autonomous Underwater Vehicles.* PhD thesis, Institute for Systems and Robotics, 2007.

[37] F. C. Teixeira and A. M. Pascoal, "Geophysical navigation of autonomous underwater vehicles using geomagnetic information," in *2nd IFAC Workshop, Navigation, Guidance and Control of Underwater Vehicles*, 2008.

[38] N. Kato and T. Shigetomi, "Underwater navigation for long-range autonomous underwater vehicles using geomagnetic and bathymetric information," *Advanced Robotics*, vol. 23, no. 7-8, pp. 787–803, 2009.

[39] C. Jones, "Email correspondence regarding the derating of slocum glider lithium primary packs." Personal Communication, June 2014.

[40] B. Greenan, "Presentation on the overturning in the subpolar north atlantic program." Personal Communication, July 2014.

[41] E. Gallimore, J. Partan, I. Vaughn, S. Singh, J. Shusta, and L. Freitag, “The WHOI micromodem-2: A scalable system for acoustic communications and networking,” in *OCEANS 2010*, pp. 1 –7, Sept. 2010.

[42] S. Smith and D. Kronen, “Experimental results of an inexpensive short baseline acoustic positioning system for AUV navigation,” in *OCEANS '97. MTS/IEEE Conference Proceedings*, vol. 1, pp. 714 –720 vol.1, Oct 1997.

[43] J. Becker and et al., “Global bathymetry and elevation data at 30 arc seconds resolution: SRTM30 PLUS,” *Geod.*, 2009.

[44] C. Amante and B. W. Eakins, *ETOPO1 1 arc-minute global relief model: procedures, data sources and analysis.* US Department of Commerce, National Oceanic and Atmospheric Administration, National Environmental Satellite, Data, and Information Service, National Geophysical Data Center, Marine Geology and Geophysics Division, 2009.

[45] S. Maus, T. Sazonova, K. Hemant, J. D. Fairhead, and D. Ravat, “National geophysical data center candidate for the world digital magnetic anomaly map,” *Geochemistry, Geophysics, Geosystems*, vol. 8, no. 6, pp. n/a–n/a, 2007.

[46] Y. Quesnel, M. Catalan, and T. Ishihara, “A new global marine magnetic anomaly data set,” *Journal of Geophysical Research: Solid Earth (1978–2012)*, vol. 114, no. B4, 2009.

[47] S. Maus, U. Barckhausen, H. Berkenbosch, N. Bournas, J. Brozena, V. Childers, F. Dostaler, J. Fairhead, C. Finn, R. Von Frese, *et al.*, “EMAG2: A 2–arc min resolution earth magnetic anomaly grid compiled from satellite, airborne, and marine magnetic measurements,” *Geochemistry, Geophysics, Geosystems*, vol. 10, no. 8, 2009.

[48] P. Honarvar, L. Nolan, L. Crisby-Whittle, and K. Morgan, “The geoscience atlas,” Report 13-1, Newfoundland and Labrador Department of Natural Resources, 2013. Geological Survey.

[49] M. Tominaga, W. W. Sager, M. A. Tivey, and S.-M. Lee, “Deep-tow magnetic anomaly study of the Pacific Jurassic Quiet Zone and implications for the geomagnetic polarity reversal timescale and geomagnetic field behavior,” *Journal of Geophysical Research: Solid Earth (1978–2012)*, vol. 113, no. B7, 2008.

[50] M. A. Tivey, H. Schouten, and M. C. Kleinrock, “A near-bottom magnetic survey of the Mid-Atlantic Ridge axis at 26ř N: Implications for the tectonic evolution of the TAG segment,” *Journal of Geophysical Research: Solid Earth (1978–2012)*, vol. 108, no. B5, 2003.

[51] M. A. Tivey and J. Dyment, “The magnetic signature of hydrothermal systems in slow spreading environments,” *Diversity of Hydrothermal Systems on Slow Spreading Ocean Ridges*, pp. 43–66, 2010.

[52] J. Manley and S. Willcox, “The wave glider: A persistent platform for ocean science,” in *OCEANS 2010 IEEE-Sydney*, pp. 1–5, IEEE, 2010.

[53] H. Stommel, “Direct measurements of sub-surface currents,” *Deep Sea Research (1953)*, vol. 2, no. 4, pp. 284 – 285, 1955.

[54] J. C. Swallow, “A neutral-buoyancy float for measuring deep currents,” *Deep Sea Research (1953)*, vol. 3, no. 1, pp. 74 – 81, 1955.

[55] R. E. Davis, P. D. Killworth, and J. R. Blundell, “Comparison of Autonomous Lagrangian Circulation Explorer and fine resolution Antarctic model results in

the South Atlantic," *Journal of Geophysical Research*, vol. 101, pp. 855–884, 1996.

[56] H. Stommel, "The slocum mission," *Oceanography*, pp. 22–25, 1989.

[57] T. B. Curtin, J. G. Bellingham, J. Catipovic, and D.Webb, "Autonomous oceanographic sampling networks," *Oceanography*, vol. 6, pp. 86–94, 1993.

[58] D. Webb, P. Simonetti, and C. Jones, "Slocum: an underwater glider propelled by environmental energy," *Oceanic Engineering, IEEE Journal of*, vol. 26, pp. 447–452, Oct 2001.

[59] P. Simonetti, "Slocum glider: Design and 1991 field trials," tech. rep., Webb Research Corp., 1992.

[60] D. Webb and P. Simonetti, "A simpified approach to the prediction and optimization of performance of underwater gliders," in *Proc. of the 10th Symposium on Unmanned Untethered Submersible Technology in Durham, New Hampshire, USA*, 1997.

[61] E. Creed, J. Kerfoot, C. Mudgal, and H. Barrier, "Transition of slocum electric gliders to a sustained operational system," in *Proc. of IEEE Oceans*, vol. 2, pp. 828–833 Vol.2, Nov. 2004.

[62] J. Sherman, R. Davis, W. Owens, and J. Valdes, "The autonomous underwater glider "spray"," *Oceanic Engineering, IEEE Journal of*, vol. 26, pp. 437–446, Oct 2001.

[63] C. Eriksen, T. Osse, R. Light, T. Wen, T. Lehman, P. Sabin, J. Ballard, and A. Chiodi, "Seaglider: A long-range autonomous underwater vehicle for

oceanographic research," *Oceanic Engineering, IEEE Journal of*, vol. 26, no. 4, pp. 424–436, 2001.

[64] R. Davis, C. Eriksen, and C. Jones, *The Technology and Applications of Autonomous Underwater Vehicles*, ch. Autonomous buoyancy driven underwater gliders, pp. 37–58. Taylor and Francis, 2002.

[65] C. Eriksen, "Autonomous underwater gliders," tech. rep., Autonomous and Lagrangian Platforms and Sensors (ALPS) Workshop, Sea Lodge, La Jolla CA, 2003.

[66] D. Rudnick, R. Davis, C. Eriksen, D. Fratantoni, and M. Perry, "Underwater gliders for ocean research," *Marine Technology Society Journal*, vol. 38, pp. 73–84, 2004.

[67] G. Griffiths, C. Jones, J. Ferguson, and N. Bose, "Undersea gliders," *Journal of Ocean Technology*, vol. 2, no. 2, pp. 65–75, 2007.

[68] S. Jenkins, D. Humphreys, J. Sherman, J. Osse, C. Jones, N. Leonard, J. Graver, R. Bachmayer, T. Clem, P. Carroll, P. Davis, J. Berry, P. Berry, P. Worley, and J. Wasyl, *Underwater Glider System Study Technical Report 53.* Scripps Institution of Oceanography, 2003.

[69] R. Hine, G. Hine, and J. Manley, "The wave glider, a persistent platform for ocean science," in *Proc. of Everyone's Gliding Observatories, Cyprus*, 2009.

[70] C. R. Fralick and J. Manley, "The dartő wave glider advanced technology demonstration results," in *Proc. of Everyone's Gliding Observatories, Cyprus*, 2009.

[71] Y. L. Page, "Innovative glider technologies," in *Everyones Gliding Observatories*, 2008.

[72] J. Imlach and R. Mahr, "Modification of a military grade glider for coastal scientific applications," in *Oceans, 2012*, pp. 1–6, Oct 2012.

[73] M.E.Furlong, S. McPhail, and P. Stevenson, "A concept design for an ultra-long-range survey class AUV," in *Proc. of IEEE Oceans - Europe*, pp. 1 –6, June 2007.

[74] S. McPhail, P. Stevenson, M. Pebody, and M. Furlong, "The NOCS long range AUV project," in *National Marine Facilities Department Seminar Series*, 2008.

[75] M. E. Furlong, D. Paxton, P. Stevenson, M. Pebody, S. D. McPhail, and J. Perrett, "Autosub long range: A long range deep diving AUV for ocean monitoring," in *Autonomous Underwater Vehicles (AUV), 2012 IEEE/OES*, pp. 1–7, IEEE, 2012.

[76] B. W. Hobson, J. G. Bellingham, B. Kieft, R. McEwen, M. Godin, and Y. Zhang, "Tethys-class long range AUVs-extending the endurance of propeller-driven cruising AUVs from days to weeks," in *Autonomous Underwater Vehicles (AUV), 2012 IEEE/OES*, pp. 1–8, IEEE, 2012.

[77] B. Butler and V. D. Hertog, "Theseus: A cable-laying AUV," in *Proc. of the 8th International Symposium on Unmanned Untether Submesible Technology*, 1993.

[78] J. Ferguson, "The Theseus autonomous underwater vehicle. two successful missions," in *Proc. of the International Symposium on Underwater Technology*, pp. 109 –114, 1998.

[79] J. Ferguson, “Adapting AUVs for use in under-ice scientific missions,” in *Proc. of IEEE Oceans*, pp. 1 –5, 2008.

[80] J. Ferguson, “Under-ice seabed mapping with AUVs,” in *Proc. of Oceans - Europe*, pp. 1 –6, 2009.

[81] D. Research and D. Canada, “Autonomous under-ice surveys for Canadian Arctic sovereignty: Project cornerstone.” Fact Sheet No. MAP0809, 2009.

[82] C. Kaminski, T. Crees, J. Ferguson, A. Forrest, J. Williams, D. Hopkin, and G. Heard, “12 days under ice-an historic AUV deployment in the Canadian High Arctic,” in *Autonomous Underwater Vehicles (AUV), 2010 IEEE/OES*, pp. 1–11, IEEE, 2010.

[83] P. Stevenson, N. W. Millard, S. D. McPhail, J. Riggs, D. White, M. Pebody, J. R. Perrett, and A. T. Webb, “Engineering an autonomous underwater vehicle for under ice operations,” *ASME Conference Proceedings*, vol. 2003, no. 36835, pp. 445–452, 2003.

[84] M. Pebody, “Autonomous underwater vehicle collision avoidance for under-ice exploration,” *Journal of Engineering for the Maritime Environment*, vol. 222, pp. 53–66, 2008.

[85] G. Griffiths, N. W. Millard, S. D. McPhail, P. Stevenson, and P. G. Challenor, “On the reliability of the autosub autonomous underwater vehicle,” *Underwater Technology*, 2001.

[86] H. J. Venables and M. P. Meredith, “Feedbacks between ice cover, ocean stratification, and heat content in Ryder Bay, western Antarctic Peninsula,” *Journal of Geophysical Research: Oceans*, vol. 119, no. 8, pp. 5323–5336, 2014.

[87] P. H. Milne, *Underwater acoustic positioning systems.* Gulf Publishing Company, Houston, TX, 1983.

[88] J. C. Kinsey, *Advances in Precision Navigation of Oceanographic Submersibles.* PhD thesis, The John Hopkins University, 2006.

[89] M. V. Jakuba, C. N. Roman, H. Singh, C. Murphy, C. Kunz, C. Willis, T. Sato, and R. A. Sohn, "Long-baseline acoustic navigation for under-ice autonomous underwater vehicle operations," *Journal of Field Robotics*, vol. 25, no. 11-12, pp. 861–879, 2008.

[90] L. Techy, K. A. Morgansen, and C. A. Woolsey, "Long-baseline ranging system for acoustic underwater localization of the seaglider underwater glider," tech. rep., Technical report, University of Washington, Aeronautics & Astronautics, Seattle, WA, 2010.

[91] P. Batista, C. Silvestre, and P. Oliveira, "Single range aided navigation and source localization: Observability and filter design," *Systems & Control Letters*, vol. 60, no. 8, pp. 665–673, 2011.

[92] J.-P. Peyronnet, R. Person, and F. Rybicki, "POSIDONIA 6000: a new long range highly accurate ultra short base line positioning system," in *OCEANS '98 Conference Proceedings*, vol. 3, pp. 1721 –1727 vol.3, sep-1 oct 1998.

[93] F. P. Parthiot and J.-F. Denis, "A better way to navigate on deep sea floors," in *OCEANS'93. Engineering in Harmony with Ocean. Proceedings*, pp. II494–II498, IEEE, 1993.

[94] T. Ura and K. Kim, “On-site ins update of an AUV "r2d4" by SSBL based position estimation,” in *OCEANS’04. MTTS/IEEE TECHNO-OCEAN’04*, vol. 3, pp. 1606–1611, IEEE, 2004.

[95] L. Christensen, M. Fritsche, J. Albiez, and F. Kirchner, “USBL pose estimation using multiple responders,” in *OCEANS 2010 IEEE-Sydney*, pp. 1–9, IEEE, 2010.

[96] M. Youngberg, “Method for extending GPS to underwater applications (US Patent 5119341),” 1992.

[97] H. Thomas, “GIB buoys: an interface between space and depths of the oceans,” in *Autonomous Underwater Vehicles, 1998. AUV’98. Proceedings Of The 1998 Workshop on*, pp. 181 –184, aug 1998.

[98] A. Alcocer, P. Oliveira, and A. Pascoal, “Underwater acoustic positioning system based on buoys with gp,” in *8th European Conf. on Underwater Acoustics*, 2006.

[99] C. E. G. LaPointe, “Virtual long baseline (VLBL) autonomous underwater vehicle navigation using a single transponder,” Master’s thesis, Massachusetts Institute of Technology, 2006.

[100] S. E. Webster, *Decentralized Single-Beacon Acoustic Navigation: Combined Communication and Navigation for Underwater Vehicles*. PhD thesis, The John Hopkins University, 2010.

[101] Ø. Hegrenæs, K. Gade, O. Hagen, and P. Hagen, “Underwater transponder positioning and navigation,” in *Proceedings of the MTS/IEEE Oceans Conference, Biloxi, MS*, 2009.

[102] M. B. Larsen, “Synthetic long baseline navigation of underwater vehicles,” in *OCEANS 2000 MTS/IEEE Conference and Exhibition*, vol. 3, pp. 2043–2050, IEEE, 2000.

[103] R. M. Eustice, H. Singh, and L. L. Whitcomb, “Synchronous-clock, one-way-travel-time acoustic navigation for underwater vehicles,” *journal of field robotics*, vol. 28, no. 1, pp. 121–136, 2011.

[104] S. Singh, S. Webster, L. Freitag, L. Whitcomb, K. Ball, J. Bailey, and C. Taylor, “Acoustic communication performance of the WHOI micro-modem in sea trials of the nereus vehicle to 11,000 m depth,” in *OCEANS 2009, MTS/IEEE Biloxi - Marine Technology for Our Future: Global and Local Challenges*, pp. 1 –6, Oct. 2009.

[105] R. M. Eustice, L. L. Whitcomb, H. Singh, and M. Grund, “Experimental results in synchronous-clock one-way-travel-time acoustic navigation for autonomous underwater vehicles,” in *Robotics and Automation, 2007 IEEE International Conference on*, pp. 4257–4264, IEEE, 2007.

[106] A. Bahr, J. J. Leonard, and M. F. Fallon, “Cooperative localization for autonomous underwater vehicles,” *The International Journal of Robotics Research*, vol. 28, no. 6, pp. 714–728, 2009.

[107] G. Rui and M. Chitre, “Cooperative positioning using range-only measurements between two AUVs,” in *OCEANS 2010 IEEE-Sydney*, pp. 1–6, IEEE, 2010.

[108] N. M. Barbour, “Inertial navigation sensors,” in *RTO-EN-SET-116(2011) Low-Cost Navigation Sensors and Integration Technology Lecture Series*, 2011.

[109] F. Daum, "Nonlinear filters: beyond the Kalman filter," *Aerospace and Electronic Systems Magazine, IEEE*, vol. 20, no. 8, pp. 57–69, 2005.

[110] L. Whitcomb, D. Yoerger, and H. Singh, "Advances in doppler-based navigation of underwater robotic vehicles," in *Robotics and Automation, IEEE International Conference on*, 1999.

[111] M. Stanway, "Water profile navigation with an acoustic doppler current profiler," in *OCEANS 2010 IEEE - Sydney*, pp. 1–5, May 2010.

[112] L. J. B. Medagoda, *Mid-water Localisation for Autonomous Underwater Vehicles.* PhD thesis, University of Sydney, 2012.

[113] D. A. Smallwood and L. L. Whitcomb, "Model-based dynamic positioning of underwater robotic vehicles: theory and experiment," *Oceanic Engineering, IEEE Journal of*, vol. 29, pp. 169 – 186, 2004.

[114] T. Fossen and S. Sagatun, "Adaptive control of nonlinear underwater robotic systems," in *Robotics and Automation, 1991. Proceedings., 1991 IEEE International Conference on*, pp. 1687 –1694 vol.2, apr 1991.

[115] D. Smallwood and L. Whitcomb, "The effect of model accuracy and thruster saturation on tracking performance of model based controllers for underwater robotic vehicles: experimental results," in *Robotics and Automation, 2002. Proceedings. ICRA '02. IEEE International Conference on*, vol. 2, pp. 1081 –1087, 2002.

[116] R. Cristi, F. A. Papoulias, and A. J. Healey, "Adaptive sliding mode control of autonomous underwater vehicles in the dive plane," *Oceanic Engineering, IEEE Journal of*, vol. 15, no. 3, pp. 152–160, 1990.

[117] A. J. Healey and D. Lienard, “Multivariable sliding mode control for autonomous diving and steering of unmanned underwater vehicles,” *Oceanic Engineering, IEEE Journal of*, vol. 18, no. 3, pp. 327–339, 1993.

[118] L. V. Steenson, A. Phillips, E. Rogers, M. Furlong, and S. Turnock, “Experimental verification of a depth controller using model predictive control with constraints onboard a thruster actuated AUV,” in *IFAC Workshop on Navigation, Guidance and Control of Underwater Vehicles (NGCUV?2012)*, April 2012.

[119] S. Martin and L. Whitcomb, “Preliminary results in experimental identification of 3-DOF coupled dynamical plant for underwater vehicles,” in *OCEANS 2008*, pp. 1 –9, Sept. 2008.

[120] O. Hegrenaes and O. Hallingstad, “Model-aided INS with sea current estimation for robust underwater navigation,” *Oceanic Engineering, IEEE Journal of*, vol. 36, pp. 316 –337, april 2011.

[121] S. B. Williams, P. Newman, J. Rosenblatt, G. Dissanayake, and H. Durrant-Whyte, “Autonomous underwater navigation and control,” *Robotica*, vol. 19, pp. 481–496, August 2001.

[122] H. Durrant-Whyte and T. Bailey, “Simultaneous localization and mapping: part i,” *Robotics & Automation Magazine, IEEE*, vol. 13, no. 2, pp. 99–110, 2006.

[123] T. Bailey and H. Durrant-Whyte, “Simultaneous localization and mapping (SLAM): Part ii,” *IEEE Robotics & Automation Magazine*, vol. 13, no. 3, pp. 108–117, 2006.

[124] J. Folkesson and J. Leonard, “Autonomy through SLAM for an underwater robot,” in *The 14th International Symposium on Robotics Research (ISRR)*, 2009.

[125] R. Eustice, H. Singh, W. Hole, and W. Hole, “Visually navigating the RMS titanic with SLAM information filters,” in *in Proceedings of Robotics: Science and Systems*, pp. 57–64, 2005.

[126] S. Barkby, S. Williams, O. Pizarro, and M. Jakuba, “Bathymetric particle filter slam using trajectory maps,” *The International Journal of Robotics Research*, 2012.

[127] A. Zorn, “A merging of system technologies: all-accelerometer inertial navigation and gravity gradiometry,” in *Position Location and Navigation Symposium, 2002 IEEE*, pp. 66 – 73, 2002.

[128] H. Rice and V. Benischek, “Submarine navigation applications of atom interferometry,” in *Position, Location and Navigation Symposium, 2008 IEEE/ION*, pp. 933 –939, May 2008.

[129] J. Moryl, H. Rice, and S. Shinners, “The universal gravity module for enhanced submarine navigation,” in *Position Location and Navigation Symposium, IEEE 1998*, pp. 324 –331, apr 1998.

[130] F. Goldenberg, “Geomagnetic navigation beyond the magnetic compass,” in *Position, Location, And Navigation Symposium, 2006 IEEE/ION*, pp. 684 – 694, 25-27, 2006.

[131] C. Tyren, “Magnetic terrain navigation,” in *Unmanned Untethered Submersible Technology, Proceedings of the 1987 5th International Symposium on*, vol. 5, pp. 245 – 256, jun 1987.

[132] J. Vasconcelos, G. Elkaim, C. Silvestre, P. Oliveira, and B. Cardeira, “Geometric approach to strapdown magnetometer calibration in sensor frame,” *Aerospace and Electronic Systems, IEEE Transactions on*, vol. 47, no. 2, pp. 1293–1306, 2011.

[133] J. Haverinen and A. Kemppainen, “Global indoor self-localization based on the ambient magnetic field,” *Robot. Auton. Syst.*, vol. 57, pp. 1028–1035, October 2009.

[134] W. F. Storms, “Magnetic field aided indoor navigation,” Master’s thesis, Air Force Institute of Technology, 2009.

[135] N. NOVKOVSKI, “Progress and limitations in magnetic field measurements,” in *Geomagnetics for Aeronautical Safety*, pp. 201–212, Springer, 2006.

[136] F. Primdahl, “The fluxgate magnetometer,” *Journal of Physics E: Scientific Instruments*, vol. 12, no. 4, p. 241, 1979.

[137] *Mag648 and Mag649 Low Power Three-Axis Magnetic Field Sensors, Bartington Instruments, DS2298/9, retreived July 2011.*

[138] W. E. Bell and A. L. Bloom, “Optical detection of magnetic resonance in alkali metal vapor,” *Physical Review*, vol. 107, no. 6, p. 1559, 1957.

[139] P. D. Schwindt, S. Knappe, V. Shah, L. Hollberg, J. Kitching, L.-A. Liew, and J. Moreland, “Chip-scale atomic magnetometer,” *Applied Physics Letters*, vol. 85, no. 26, pp. 6409–6411, 2004.

[140] V. Shah, S. Knappe, P. D. Schwindt, and J. Kitching, “Subpicotesla atomic magnetometry with a microfabricated vapour cell,” *Nature Photonics*, vol. 1, no. 11, pp. 649–652, 2007.

[141] M. Prouty and R. Johnson, “Small, low power, high performance magnetometers,” in *EGM 2010 International Workshop*, 2010.

[142] R. Johnson, “G-880AUV integration with teledyne gavia AUV.” `http://www.geometrics.com/blog/blog-entry/?article_id=177/`, 2012.

[143] N. Isezaki, “A new shipboard three-component magnetometer,” *Geophysics*, vol. 51, no. 10, pp. 1992–1998, 1986.

[144] J. Korenaga, “Comprehensive analysis of marine magnetic vector anomalies,” *Journal of Geophysical Research: Solid Earth (1978–2012)*, vol. 100, no. B1, pp. 365–378, 1995.

[145] J. M. Merayo, P. Brauer, F. Primdahl, J. R. Petersen, and O. V. Nielsen, “Scalar calibration of vector magnetometers,” *Measurement science and technology*, vol. 11, no. 2, p. 120, 2000.

[146] N. Olsen, L. Toffner-Clausen, T. J. Sabaka, P. Brauer, J. M. Merayo, J. Jorgensen, J. Léger, O. V. Nielsen, F. Primdahl, and T. Risbo, “Calibration of the Orsted vector magnetometer,” *Earth Planets and Space*, vol. 55, no. 1, pp. 11–18, 2003.

[147] R. Alonso and M. D. Shuster, “Attitude-independent magnetometer-bias determination: a survey,” *Journal of the Astronautical sciences*, vol. 50, no. 4, pp. 453–476, 2002.

[148] R. Alonso and M. D. Shuster, "TWOSTEP: a fast robust algorithm for attitude-independent magnetometer-bias determination," *Journal of the Astronautical Sciences*, vol. 50, no. 4, pp. 433–452, 2002.

[149] R. Alonso and M. D. Shuster, "Complete linear attitude-independent magnetometer calibration," *Journal of the Astronautical Sciences*, vol. 50, no. 4, pp. 477–490, 2002.

[150] J. Gee and S. Cande, "A surface-towed vector magnetometer," *Geophysical research letters*, vol. 29, no. 14, pp. 15–1, 2002.

[151] M. Engels, U. Barckhausen, and J. S. Gee, "A new towed marine vector magnetometer: methods and results from a Central Pacific cruise," *Geophysical Journal International*, vol. 172, no. 1, pp. 115–129, 2008.

[152] D. Turner, I. Anderson, J. Mason, and M. Cox, "An algorithm for fitting an ellipsoid to data," *National Physical Laboratory, UK*, 1999.

[153] A. Fitzgibbon, M. Pilu, and R. B. Fisher, "Direct least square fitting of ellipses," *Pattern Analysis and Machine Intelligence, IEEE Transactions on*, vol. 21, no. 5, pp. 476–480, 1999.

[154] Q. Li and J. G. Griffiths, "Least squares ellipsoid specific fitting," in *Geometric Modeling and Processing, 2004. Proceedings*, pp. 335–340, IEEE, 2004.

[155] I. Markovsky, A. Kukush, and S. Van Huffel, "Consistent least squares fitting of ellipsoids," *Numerische Mathematik*, vol. 98, no. 1, pp. 177–194, 2004.

[156] C. Foster and G. Elkaim, "Extension of a two-step calibration methodology to include nonorthogonal sensor axes," *Aerospace and Electronic Systems, IEEE Transactions on*, vol. 44, no. 3, pp. 1070–1078, 2008.

[157] V. Renaudin, M. H. Afzal, and G. Lachapelle, “Complete triaxis magnetometer calibration in the magnetic domain,” *Journal of sensors*, vol. 2010, 2010.

[158] V. Renaudin, M. H. Afzal, and G. Lachapelle, “New method for magnetometers based orientation estimation,” in *Position Location and Navigation Symposium (PLANS), 2010 IEEE/ION*, pp. 348–356, IEEE, 2010.

[159] J. L. Crassidis, K.-L. Lai, and R. R. Harman, “Real-time attitude-independent three-axis magnetometer calibration,” *Journal of Guidance, Control, and Dynamics*, vol. 28, no. 1, pp. 115–120, 2005.

[160] J. C. Springmann, *Satellite Attitude Determination with Low-Cost Sensors.* PhD thesis, University of Michigan, 2013.

[161] J. Frey, J. Hawkins, and D. Thorsen, “Magnetometer calibration in the presence of hard magnetic torquers,” in *Aerospace Conference, 2014 IEEE*, pp. 1–6, IEEE, 2014.

[162] A. Bronner, M. Munschy, D. Sauter, J. Carlut, R. Searle, and A. Maineult, “Deep-tow 3C magnetic measurement: Solutions for calibration and interpretation,” *Geophysics*, vol. 78, no. 3, pp. J15–J23, 2013.

[163] J. Graver, *Underwater gliders: Dynamics, control and design.* PhD thesis, Princeton University, 2005.

[164] L. Merckelbach, D. Smeed, and G. Griffiths, “Vertical water velocities from underwater gliders,” *J. Atmos. Oceanic Technol.*, vol. 27, pp. 547–563, Mar. 2010.

[165] D. Steinberg, A. Bender, and A. Friedman, “Toward selection of a propulsion method for a long range benthic imaging AUV,” in *Proc. 16th Int. Symp. on Unmanned Untethered Submersible Technology (UUST)*, 2009.

[166] B. Claus, “Development of an underwater glider equipped with an auxiliary propulsion module,” Master’s thesis, Memorial University of Newfoundland, 2010.

[167] B. Claus, R. Bachmayer, and C. D. Williams, “Experimental flight stability tests for the horizontal flight mode of a hybrid glider,” *AUV 2010*, 2010.

[168] H. Singh, D. Yoerger, and A. Bradley, “Issues in AUV design and deployment for oceanographic research,” in *Proc. of the IEEE International Conference on Robotics and Automation*, vol. 3, pp. 1857–1862, Apr 1997.

[169] J. E. Dennis Jr and R. B. Schnabel, *Numerical methods for unconstrained optimization and nonlinear equations*, vol. 16. Siam, 1996.

[170] L. Ljung, “System identification,” in *Signal Analysis and Prediction* (A. ProchÃązka, J. UhlÃŋÅŹ, P. Rayner, and N. Kingsbury, eds.), Applied and Numerical Harmonic Analysis, pp. 163–173, BirkhÃďuser Boston, 1998.

[171] K. Ogata, *Discrete-time control systems*, vol. 2. Prentice Hall Englewood Cliffs, NJ, 1995.

[172] D. S. Naidu, *Optimal control systems*, vol. 2. CRC press, 2002.

[173] D. Fox, J. Hightower, L. Liao, D. Schulz, and G. Borriello, “Bayesian filtering for location estimation,” *Pervasive Computing, IEEE*, vol. 2, no. 3, pp. 24–33, 2003.

[174] M. Sanjeev Arulampalam, S. Maskell, N. Gordon, and T. Clapp, “A tutorial on particle filters for online nonlinear/non-Gaussian Bayesian tracking,” *Signal Processing, IEEE Transactions on*, vol. 50, no. 2, pp. 174–188, 2002.

[175] A. Doucet, S. Godsill, and C. Andrieu, “On sequential Monte Carlo sampling methods for Bayesian filtering,” *STATISTICS AND COMPUTING*, vol. 10, no. 3, pp. 197–208, 2000.

[176] B. Ristic, S. Arulampalam, and N. Gordon, *Beyond the Kalman Filter: Particle Filters for Tracking Applications.* Artech House, 2004.

[177] D. Simon, *Optimal state estimation: Kalman, H infinity, and nonlinear approaches.* John Wiley & Sons, 2006.

[178] N. Gordon, D. Salmond, and A. F. M. Smith, “Novel approach to nonlinear/non-Gaussian Bayesian state estimation,” *Radar and Signal Processing, IEE Proceedings F*, vol. 140, no. 2, pp. 107–113, 1993.

[179] S. E. Houts, S. G. Dektor, and S. M. Rock, “A robust framework for failure detection and recovery for terrain-relative navigation,” in *Unmanned Untethered Submersible Technology 2013*, (Portsmouth, NH), Aug 2013.

[180] Y. Bar-Shalom, X. R. Li, and T. Kirubarajan, *Estimation with applications to tracking and navigation: theory algorithms and software.* John Wiley & Sons, 2004.

[181] G. Kitagawa, “Monte Carlo filter and smoother for non-Gaussian nonlinear state space models,” *Journal of Computational and Graphical Statistics*, vol. 5, no. 1, pp. pp. 1–25, 1996.

[182] J. Lagadec, D. Cecchi, M. Rixen, and R. Grasso, “Terrain navigation for underwater autonomous gliders,” in *MREA10, Lerici, Italy, October 18-22*, 2010.

[183] D. E. Wells and D. Monahan, “IHO S44 standards for hydrographic surveys and the variety of requirements for bathymetric data,” *Hydrographic Journal*, pp. 9–16, 2002.

[184] R. Hodges, *Underwater Acoustics: Analysis, Design and Performance of Sonar*, ch. 5, pp. 84–91. John Wiley and Sons, Ltd., 2010.

[185] DFO, “Archived tidal data for station 905,” 2013. Accessed on Dec. 12th, 2013.

[186] M. Matsumoto and T. Nishimura, “Mersenne twister: A 623-dimensionally equidistributed uniform pseudo-random number generator,” *ACM Trans. Model. Comput. Simul.*, vol. 8, pp. 3–30, Jan. 1998.

[187] B. Claus and R. Bachmayer, “A modified particle filter suitable for embedded systems,” in *NECEC 2013*, Nov 2013.